New Insights into the Rift-to-Drift Process of the Northern South China Sea Margin Constrained by a Three-dimensional OBS Seismic Velocity Model

Jiazheng Zhang[1], Minghui Zhao[2], Weiwei Ding[3], César R. Ranero[4], Valentí Sallarès[5], Jinwei Gao[6], Cuimei Zhang[7], and Xuelin Qiu[2]

[1]South China Sea Institute of Oceanology
[2]Key Laboratory of Ocean and Marginal Sea Geology, South China Sea Institute of Oceanology, Chinese Academy of Sciences
[3]the Second Insititue of Oceanography, State Oceanic Administration of China
[4]Institut de Ciències del Mar - ICREA at CSIC
[5]Institute of Marine Sciences - CSIC
[6]Institute of Deep Sea Science and Engineering, CAS
[7]CAS Key Laboratory of Ocean and Marginal Sea Geology, South China Sea Institute of Oceanology

December 22, 2022

Abstract

A three-dimensional (3D) P-wave seismic velocity (Vp) model of the crust at the northern South China Sea margin drilled by IODP Expeditions 367/368/368X has been obtained with first-arrival travel-time tomography using wide-angle seismic data from a network of 49 OBSs and 11 air-gun shot lines. The 3D Vp distribution constrains the extent, structure and nature of the continental, continent to ocean transition (COT), and oceanic domains. Continental crust laterally ranges in thickness from ˜8 to 20 km, a ˜20 km-width COT contains no evidence of exhumed mantle, and crust with clear oceanic seismic structure ranges in thickness from ˜4.5 to 9 km. A high-velocity (7.0-7.5 km/s) lower crust (HVLC) ranges in thickness from ˜1 to 9 km across the continental and COT domains, which is interpreted as a proxy of syn-rift and syn-breakup magma associated to underplating and/or intrusions. Continental crust thinning style is abrupter in the NE segment and gradual in the SW segment. Abrupter continental thinning exhibits thicker HVLC at stretching factor (β) <˜3, whereas gentler thinning associates to thinner HVLC at β>˜4. Opening of the NE segment thus occurred by comparatively increased magmatism, whereas tectonic extension was more important in the SW segment. The Vp distribution shows the changes in deformation and magmatism are abrupt along the strike of the margin, with the segments possibly bounded by a transfer fault system. No conventional model explains the structure and segmentation of tectonic and magmatic processes. Local inherited lithospheric heterogeneities during rifting may have modulated the contrasting opening styles.

Hosted file

951198_0_art_file_10497667_rm9c8b.docx available at https://authorea.com/users/569002/articles/614608-new-insights-into-the-rift-to-drift-process-of-the-northern-south-china-sea-margin-constrained-by-a-three-dimensional-obs-seismic-velocity-model

1   **New Insights into the Rift-to-Drift Process of the Northern South China Sea Margin**

2   **Constrained by a Three-dimensional OBS Seismic Velocity Model**

3   **Jiazheng Zhang[1*], Minghui Zhao[1,6*], Weiwei Ding[2], César R. Ranero[3,4], Valenti Sallares[3],**

4   **Jinwei Gao[5], Cuimei Zhang[1], Xuelin Qiu[1,6]**

5   [1]Key Laboratory of Ocean and Marginal Sea Geology, South China Sea Institute of Oceanology,

6   Chinese Academy of Sciences, Guangzhou 510301, China.

7   [2]Key Laboratory of Submarine Geosciences, State Oceanic Administration, Second Institute of

8   Oceanography, Ministry of Natural Resources, Hangzhou 310012, China.

9   [3]Barcelona Center for Subsurface Imaging, Instituto de Ciéncies del Mar (ICM-CSIC),

10   Barcelona, Spain.

11   [4]ICREA, Barcelona, Spain

12   [5]Laboratory of Marine Geophysics and Deep-Sea Georesource, Institute of Deep-sea Science and

13   Engineering, Chinese Academy of Sciences, Sanya 572000, China.

14   [6]University of Chinese Academy of Sciences, Beijing 100049, China.

15   Corresponding author: Jiazheng Zhang (jzzhang@scsio.ac.cn) ; Minghui Zhao

16   (mhzhao@scsio.ac.cn)

17   **Key Points:**

18   • Crustal structure at the northern South China Sea drilled by IODP Expeditions

19   367/368/368X is unraveled by 3D controlled-source tomography

20   • Abrupt along-strike change in deformation and magmatism from the NE tectono-

21   magmatic segment to the SW tectonic-dominated segment is found

22   • Local inherited lithospheric heterogeneities may have caused the along-strike

23   segmentation and the resultant contrasting opening styles

Abstract

A three-dimensional (3D) P-wave seismic velocity (Vp) model of the crust at the northern South China Sea margin drilled by IODP Expeditions 367/368/368X has been obtained with first-arrival travel-time tomography using wide-angle seismic data from a network of 49 OBSs and 11 air-gun shot lines. The 3D Vp distribution constrains the extent, structure and nature of the continental, continent to ocean transition (COT), and oceanic domains. Continental crust laterally ranges in thickness from ~8 to 20 km, a ~20 km-width COT contains no evidence of exhumed mantle, and crust with clear oceanic seismic structure ranges in thickness from ~4.5 to 9 km. A high-velocity (7.0-7.5 km/s) lower crust (HVLC) ranges in thickness from ~1 to 9 km across the continental and COT domains, which is interpreted as a proxy of syn-rift and syn-breakup magma associated to underplating and/or intrusions. Continental crust thinning style is abrupter in the NE segment and gradual in the SW segment. Abrupter continental thinning exhibits thicker HVLC at stretching factor (β) <~3, whereas gentler thinning associates to thinner HVLC at β>~4. Opening of the NE segment thus occurred by comparatively increased magmatism, whereas tectonic extension was more important in the SW segment. The Vp distribution shows the changes in deformation and magmatism are abrupt along the strike of the margin, with the segments possibly bounded by a transfer fault system. No conventional model explains the structure and segmentation of tectonic and magmatic processes. Local inherited lithospheric heterogeneities during rifting may have modulated the contrasting opening styles.

Plain Language Summary

Unravelling the deep structure at the northern South China Sea (SCS) margin drilled by IODP Expedition 367/368/368X can further help understand its rift-to-drift process. A 3D Vp model is therefore constructed with first-arrival travel-time tomography using wide-angle seismic data from a network of 49 OBSs and 11 air-gun shot lines. Based the 3D Vp model, we have identified different kinds of basement domains, including the continental, COT, and oceanic domains. Meanwhile, the HVLC ranging from ~1 to 9 km in thickness across the continental and COT domains is interpreted as a proxy of syn-rift and syn-breakup magmatic underplating and/or intrusions. We find that the continental crust thinning style and magma generation by decompression melting inferred from the HVLC vary along the strike of the margin, demonstrating as NE abrupter thinning with thicker HVLC at stretching factor (β) <~3, whereas

54 SW gentler thinning with thinner HVLC at β>~4. Hence, our data indicate that a transfer fault

55 system has possibly separated the NE tectono-magmatic segment from the SW tectonic-

56 dominated segment. The segmentation in tectonic and magmatic domains inferred from the 3D

57 Vp model supports that local inherited lithospheric heterogeneities may have led to the different

58 opening styles during rift-to-drift process.

59 **1 Introduction**

60 The continent to ocean transition (COT) is a relevant tectonic unit that develops on the passive

61 continental margin. It is located between the thinned continental crust and the unequivocal

62 oceanic crust, and contains key information about break-up mechanism of continental crust and

63 lithosphere and types of rifted margins (Gao et al., 2015; Peron-Pinvidic et al., 2013; Reston,

64 2009; Tucholke et al., 2007). Based on the syn-rift and syn-breakup magmatic degree at the

65 COT, the passive continental margins are usually classified into two end members, namely

66 magma-rich and magma-poor margins. The studies of structure and evolution of these margins

67 have attracted a large number of investigations, which have provided a new view on the genesis

68 of the Seaward Dipping Reflector sequences (SDRs) and the high-velocity lower crust (HVLC)

69 on the magma-rich margins (Paton et al., 2017; Holbrook and Kelemen, 1993; White et al.,

70 1987), and on the formation of hyperextended continental crust and/or exhumed serpentinized

71 mantle on the magma-poor margins (Brune et al., 2014; Huismans and Beaumont, 2011; Ranero

72 & Pérez-Gussinyé, 2010; Whitmarsh et al., 2001).

73 The South China Sea (SCS) is one of the largest marginal seas in the western Pacific (Figure

74 1). Scientific issues such as its margin nature, evolution process, breakup mechanism are current

75 research topics. Based on previous research results from studies of the COT with ocean bottom

76 seismometer (OBS) and multi-channel seismic (MCS) surveys, the northern SCS was defined

77 either as a magma-poor margin (Wan et al., 2020; Ding et al., 2012; Wang et al., 2006; Yan et

78 al., 2001) or an intermediate rifted margin (Cameselle et al., 2017; Gao et al., 2015; Clift et al.,

79 2001). The International Ocean Discovery Program (IODP) Expeditions 367/368/368X drilled

80 seven sites at the COT of the northern SCS. The rock samples support that the margin

81 experienced a rapid transition from continent to ocean without evidence for mantle exhumations

82 (Childress et al., 2020; Larsen et al., 2018a; Jian et al., 2018; Stock et al., 2018; Sun et al., 2018).

83 This differs from classic magma-poor margins where the continent is juxtaposed with exhumed

84   serpentinized mantle rocks (Whitmarsh et al., 2001). Therefore, the SCS has been suggested as

85   the "Plate-edge/Pacific" extensional basin, which is different from the Atlantic-type rifted

86   margins (Sun et al., 2019; Wang et al., 2019).

87   IODP Expeditions 367/368/368X results reveal the presence of a narrow COT (~20 km-width)

88   at the northern SCS (Larsen et al., 2018b), but the processes leading to continental breakup are

89   still debated. Some authors argue that continental breakup was mainly related to a seaward-

90   dipping low-angle extensional fault during latest stage of rifting (Nirrengarten et al., 2020).

91   Similar conclusion is obtained through lateral comparison of the transitional domain structures

92   which show that the continental rupture was mainly controlled by a combination of one or two

93   major listric normal fault(s) rooting near the Moho and a short-duration magmatic event (Ding et

94   al., 2020). However, others propose that the continental breakup is accomplished by core-

95   complex type structures related to a detachment system with flipped polarities (Zhang et al.,

96   2021). Considering the scant information of how structures of rifted continental margins vary

97   along-strike, there are speculations that they could even change within a few tens of kilometers

98   (Peron-Pinvidic et al., 2015; Franke et al., 2014; 2011). However, the new available drilling sites

99   reaching basement and the limited two-dimensional MCS profiles do not provide accurate

100   information on the lateral continuity of the structures and nature of the rocks, and thus there is

101   incomplete understanding on how the thinning of continental crust transitions into oceanic crust

102   formation.

103   Here, we present and interpret a three-dimensional (3D) P-wave seismic velocity (Vp) model

104   at the northern SCS margin. The model is firstly obtained using controlled-source data acquired

105   at a 3D OBS network that encompasses the seven drilling sites of IODP Expeditions

106   367/368/368X. Then, we combine the Vp model with the available MCS profiles, free-air gravity

107   anomalies, magnetic lineations and IODP drilling data to interpret the structure, nature and

108   spatial arrangement of the different geological domains. Finally, the structural characteristics and

109   attributes of each domain and their along-strike variations are jointly interpreted to propose a

110   possible geological model for the study area at the northern SCS.
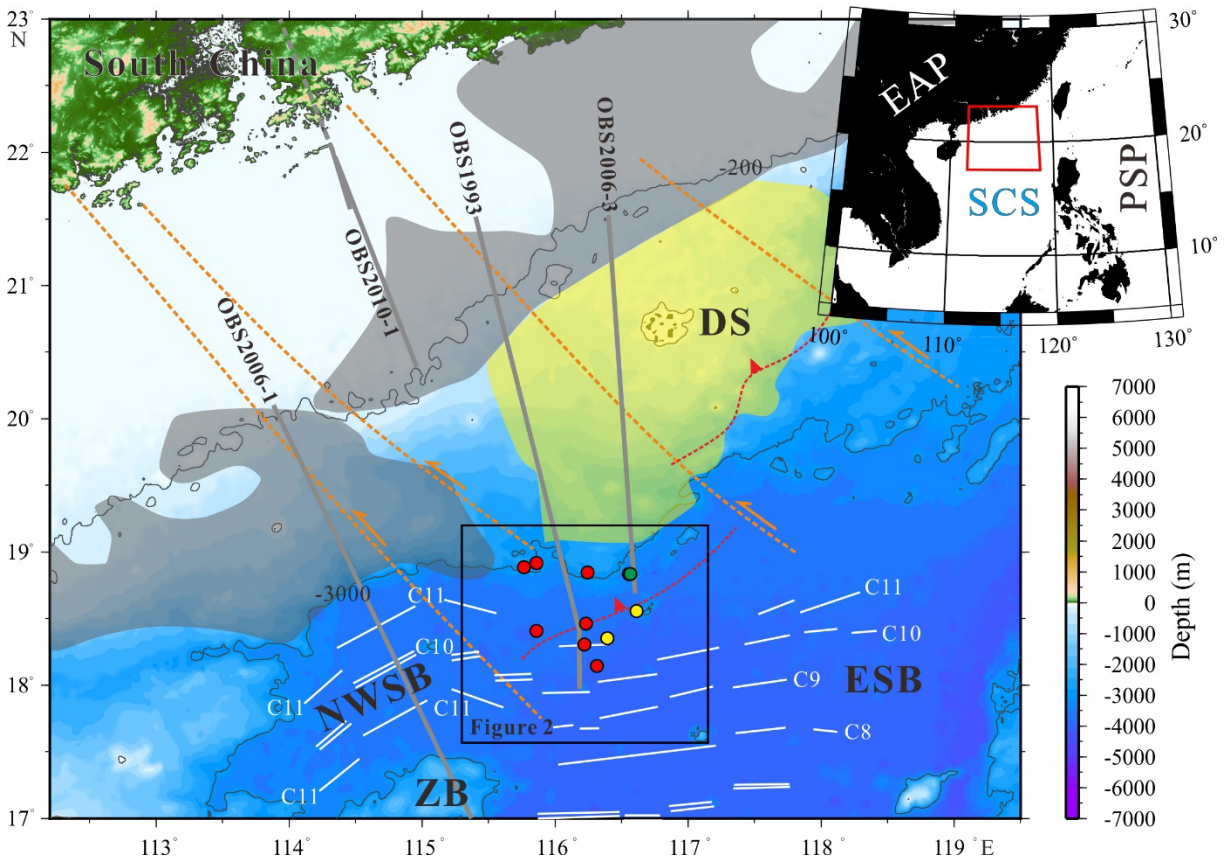
Figure 1. Combined topographic and bathymetric maps of the northern South China Sea (see location map in inset at the right-top corner) showing the distribution of major faults (orange dashed lines) and paleo-Pacific subduction zone (red dashed lines with red triangles) inferred from gravity data (Zhou et al., 2006). The location of the Mesozoic volcanic arc and the Mesozoic forearc basin identified in previous work (Zhao et al., 2019; Li et al., 2018) are shown in gray and yellow shadows, respectively. Seismic lines of OBS1993 (Yan et al., 2001), OBS2006-1 (Ding et al., 2012), OBS2006-3 (Wei et al., 2011) and OBS2010-1 (Cao et al., 2014) are shown in gray. White lines correspond to the magnetic lineations identified by Briais et al. (1993). Drill sites of ODP Leg 184, IODP Expeditions 349, 367/368/368X are indicated by green, yellow and red circles, respectively. Black box shows the location of the study area in Figure 2. SCS: South China Sea; ESB: Eastern Sub-Basin; NWSB: Northwestern Sub-Basin; ZB: Zhongsha Block; DS: Dongsha Island.

2 Geological Setting

The rhomb-shaped boundary of the nowadays SCS was formed under the interaction of the Indo-Australian, Eurasian and Philippine Sea plates. It is widely accepted that, during the Mesozoic, this region where the SCS subsequently developed was a convergent margin with Andean-type volcanic arc and forearc basin, which was affected by different magmatic episodes and was deformed by compressional structures associated with northwestward subduction of the paleo-Pacific plate (Ye et al., 2018; Pubellier & Meresse, 2013; Zhou et al., 2006; Taylor & Hayes, 1983; Holloway, 1981; Figure 1). From the Late Cretaceous to the Early Oligocene, the rollback of the subducted paleo-Pacific plate transformed the paleo-stress field from compression to extension, resulting in multi-stage rifting events, accompanied with local erosion and tectonic uplift (Savva et al., 2014; Li & Li, 2007; Taylor & Hayes, 1983).

In the northern SCS margin, some characteristics of magma-rich and magma-poor margins have been found in previous seismic surveys. For example, HVLC has been observed confined in the northeastern SCS margin (Wang et al., 2006; Yan et al., 2001; Nissen et al., 1995a), although its formation mechanism and age are debated due to the different periods of magmatism on the continental slope (Cheng et al., 2021; Fan et al., 2017; Yan et al., 2006). The hyper-extended continental crust controlled by detachment faults have also been documented in the Pearl River Mouth Basin (Deng et al., 2020; Zhang et al., 2020; Lei et al., 2019; Yang et al., 2018). However, the other important characteristics such as SDRs marked as magma-rich margin and exhumed serpentinized mantle related to magma-poor margin have yet been reported, which make it controversial about the nature of the SCS margin and subsequently confused about its formation mechanism.

Our study area locates at the northern SCS distal margin, where northwestern and northeastern corners seem to connect with the inferred Mesozoic volcanic arc and Mesozoic forearc basin, respectively (Zhao et al., 2019; Li et al., 2018; Figure 1). According to the multibeam bathymetry (Figure 2), the landward part of our study area is separated by a NW-SE extending Pearl River Mouth Canyon which seems to be the surface expression of a Mesozoic major fault (Figure 1) previously inferred by the gravity data (Zhou et al., 2006) and recently confirmed by the MCS profiles (Zhao et al., 2019). A series of basement highs (Figure 2), e.g., outer margin high (OMH) and ridges A/B/C, have been drilled here by the IODP Expeditions 367/368/368X,

154   but only rocks of continental or oceanic affinities have been found (Childress et al., 2020; Larsen

155   et al., 2018a; Jian et al., 2018; Stock et al., 2018; Sun et al., 2018). Hence, Larsen et al. (2018b)

156   suggest that a rapid transition from continental breakup to igneous oceanic crust occurs in a

157   narrow area of ~20 km-width, which has also been confirmed by subsequent researches (Zhang

158   et al., 2021; Ding et al., 2020).

159   **3 Seismic Experiment and Data Processing**

160   During the Chinese Natural Science Foundation Open Research Cruise of No. NORC2018-08

161   from May to July 2018, a 3D wide-angle seismic survey was carried out by the R/V Shiyan2 of

162   South China Sea Institute of Oceanology, Chinese Academy of Sciences (CAS) in the northern

163   SCS margin (Figure 2). The seismic source array with a total volume of 6000 in^3 (98.32 L) was

164   composed by four Bolt air-guns towed at a depth of ~10 m. The shooting interval was 90 s at a

165   speed of ~4.5 knots, providing a seismic trace spacing of ~200 m. A total of 8,751 shots were

166   fired along 11 shot lines with a total length of ~1750 km. Fifty-two 4-component short-period

167   (4.5-100 Hz) OBSs made by the Institute of Geology and Geophysics, CAS were deployed with

168   instrument spacing varying from 7 to 10 km, covering a surface of ~30000 km^2. The sampling

169   rates were 4 ms and 10 ms for different instruments. Forty-nine OBSs were finally recovered

170   with effective recording data.

171   The OBS internal clock drifts were corrected using the time-errors recorded in the logfiles

172   assuming a linear drift during the data collection period. The shot positions were corrected for

173   the offset between the Differential Global Positioning System (DGPS) antenna onboard and the

174   air-guns array. OBSs were relocated by inverting direct water-wave travel-times using a

175   combination of Monte Carlo method and least square method (Yang et al., 2020). The raw data

176   continuously recorded by the OBSs were converted and cut into seismic traces in Society of

177   Exploration Geophysicist (SEGY) format according to the shooting time. The corresponding

178   seismic sections were displayed as reduced time versus offset sections using 3-15 Hz bandpass

179   filtering in order to increase the signal-to-noise ratio (SNR, Figure 3).

180   This study focuses exclusively on P-wave first arrivals, which are best observed on record

181   sections of the geophone vertical component (Figure 3). The travel time picking steps show as

182   follows: 1) the in-line seismic profile showing the clearest arrivals is picked firstly; 2) the off-

183   line crossing the previous profile is then picked; 3) the rest of seismic sections for each OBS are

184 finally picked in order. Arrival travel-times were manually picked without differentiating

185 between crustal (e.g., Pg) and mantle phases (e.g., Pn) using the Upicker software (Wilcock,

186 2011). In total, we finally picked 152,801 first arrival travel-times. The uncertainties for the

187 picked travel-times were calculated based on their SNR within a 200 ms-long window centered

188 by the picked travel-time (e.g., Zelt & Forsyth, 1994).
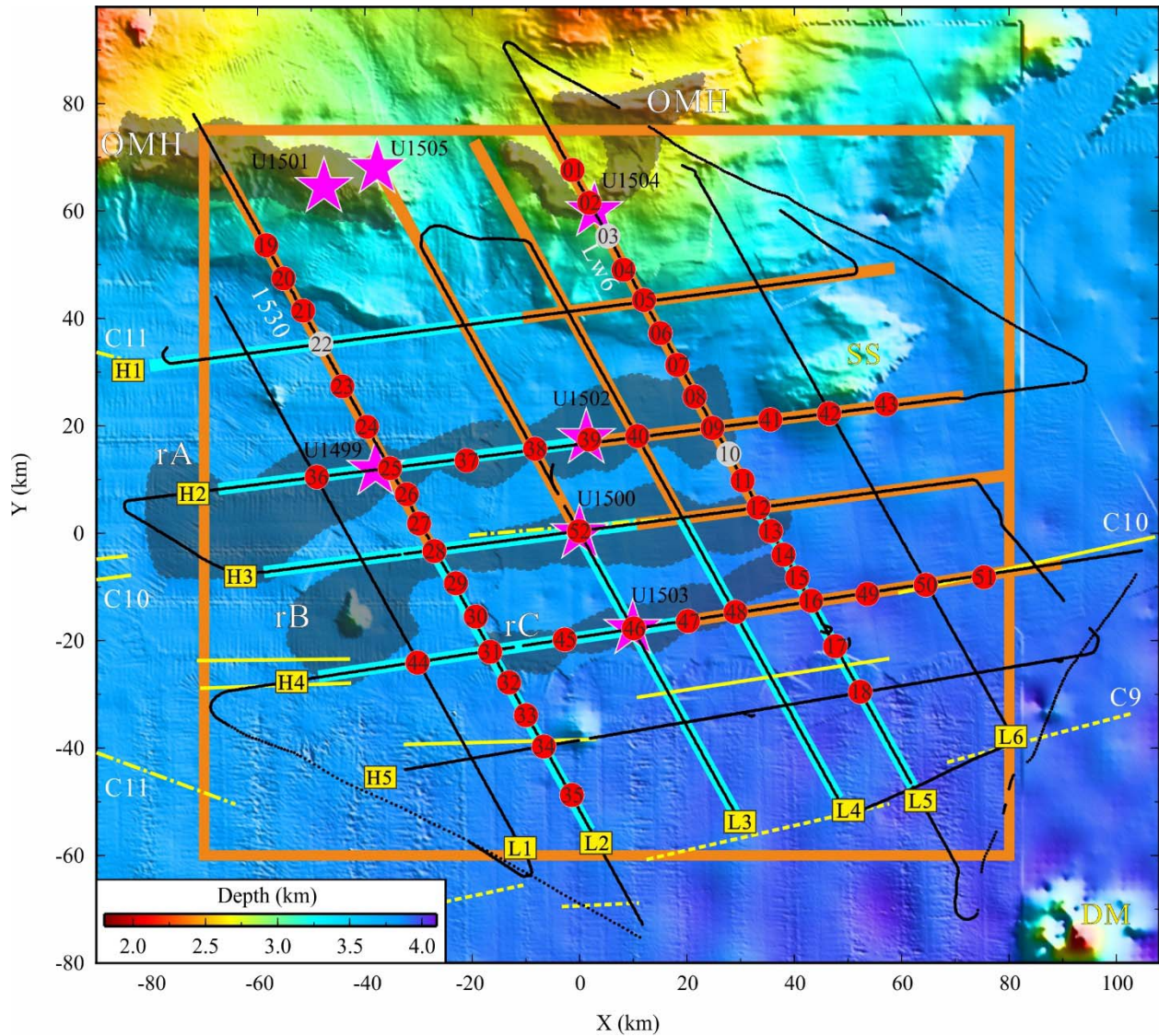
189

190 **Figure 2**. The 3D OBS seismic survey and the multibeam bathymetry map whose original

191 Geographical Coordinate has been transformed into Cartesian Coordinate using shifted Universal

192 Transverse Mercator projection (origin of the local coordinate system corresponds to 116.21992°

193 E, 18.30451° S at OBS52 and site U1500). Red numbered circles display OBSs positions, and

194 black lines with yellow lettered boxes correspond to air-gun shooting tracks. Grey numbered

195 circles indicate lost OBSs. Yellow dashed-dotted, solid and dashed lines represent magnetic

196 lineations from Briais et al. (1993). Pink stars show drilling sites of IODP Expeditions

197 367/368/368X. The orange and cyan solid lines show positive and negative parts of the vertical

198 slices of the 3D Vp model shown in Figure 5. The orange box shows the area covered by the

199 horizontal slices shown in Figure 6. The black shaded areas show the basement highs modified

200 from (Larsen et al., 2018b). OMH: outer margin high; rA/rB/rC: basement ridges A/B/C; SS:

201 Shishen Seamount; DM: Daimao Seamount.
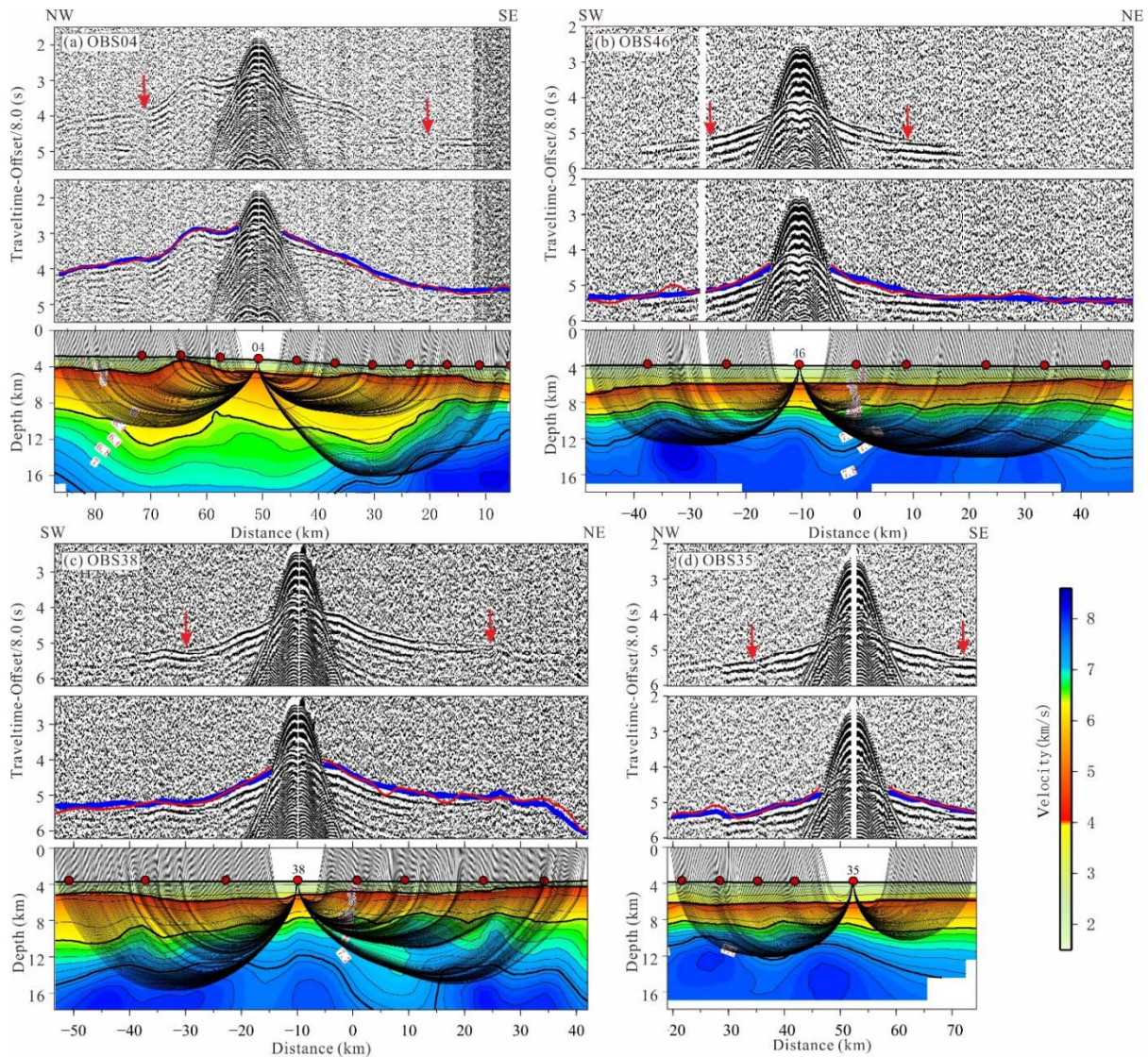
202

203 **Figure 3**. Uninterpreted seismic record sections (upper panel), interpreted seismic sections with

204 blue vertical bars of length equal to the assigned travel-time uncertainty corresponding to

205 observed picks and red lines to the modelled picks (middle panel) and vertical slices of 3D Vp

206   model with ray-paths (lower panel) along (a) profile L5 for instrument OBS04; (b) profile H2 for

207   OBS46; (c) profile H4 for OBS38; and (d) profile L2 for OBS35. The red circles indicate the

208   locations of OBS. The red arrows show the locations of triple junction of Pg, PmP and Pn.

209   **4 Modeling Method and Results**

210   4.1 Tomography Method

211   The first arrival seismic tomography code FAST (Zelt & Barton, 1998) is used to build a

212   smooth, isotropic 3D Vp model. FAST solves iteratively a regularized inverse problem to

213   construct a model with the minimum required structure that appropriately fits the observed

214   travel-times. At each iteration, it includes one step of forward modeling (ray tracing) and a

215   second step of travel-time inversion. Forward modeling computes synthetic first arrival travel-

216   times by solving the Eikonal equation based on a finite difference algorithm (Hole & Zelt, 1995;

217   Vidale, 1990). The velocity perturbation is then obtained by minimizing an objective function

218   including norms for the travel-time misfits and model roughness (Shaw & Orcutt, 1985). The

219   velocity perturbation is then added to the initial model and the resulting model is used as a new

220   starting model in the subsequent iterations. This scheme is repeated until the observed travel-

221   times are fit to the level of pick uncertainties (χ^2 close to 1 ideally).

222   The choice of the starting Vp model is an important step in the setup of any linearized

223   inversion procedure such as the one employed in FAST. In our case, the starting model is

224   composed of three layers such as water, sediment and basement. The layer boundaries

225   corresponding to the seafloor and top of the basement (TOB) are inferred from multibeam

226   bathymetry and from MCS data (Larsen et al., 2018b), respectively. Vp in the water layer is

227   fixed at 1.5 km/s. Vp at the top and bottom of the sedimentary layer are set to 1.5 km/s and 4.0

228   km/s, varying linearly within this layer. As the study area includes segments of both thinned

229   continental crust and oceanic lithosphere, a one-dimensional (1D) Vp-depth profile roughly

230   falling between the 1D Vp envelop of the thinned continental crust in the northern SCS (Liu et

231   al., 2018) and the 1D Vp of the typical oceanic crust in the Atlantic aged 0-127 Ma (White et al.,

232   1992) is chosen and draped from the TOB to construct the starting 3D Vp model. During

233   iteration, only the velocity structure below the bathymetry is recalculated according to the travel-

234   time misfits.

235   The regularization parameters of FAST include forward and inverse grid spacing as well as

236   lambda (λ), alpha (α) and iteration times. The λ is a trade-off parameter that controls the relative

237   weighting of fitting the travel time data versus solution constraints. The α controls the relative

238   importance of smoothness/flatness versus smallest perturbation within the regularization part.

239   Based on the 3D modelling experience of the Southwest Indian Ridge (Zhao et al., 2013) and

240   ESB of the SCS (Wang et al., 2016), we conduct a series of tests on the above parameters for a

241   model with dimensions of 198 km×178 km×30 km in X, Y, and Z directions. The spacing of the

242   forward grid is 0.5 km×0.5 km×0.5 km for a total of 8,645,469 nodes, whereas for the inversion

243   grid it is 2 km×2 km×2 km for a total of 132,165 nodes. We have tested different combinations

244   of λ between 0 and 10 and α between 0 and 4. The best fit after five iterations corresponds to a

245   combination of λ=3, and α=0.8. These regularization parameters will also be used in the

246   following tests of uncertainty and resolution of the tomographic Vp models constrained by the

247   same travel-time dataset.

248   4.2 Uncertainty and Resolution of the Tomographic Model

249   The solution of any inverse problem depends on the starting model chosen to some extent, and

250   a complete solution must include the measurement of its uncertainty. In order to further assess

251   the influence of the starting model on our final Vp model, a Monte Carlo approach was used to

252   obtain an estimate of the uncertainty (Zhao et al., 2013; Korenaga et al., 2000). One-hundred

253   random 3D starting models were firstly constructed in the same process as described by Section

254   4.1, in which the 1D Vp-depth profiles were randomly generated in or near the 1D Vp envelops

255   of the thinned continental crust and the typical oceanic crust as mentioned above. Then one-

256   hundred different inversions were executed using the same regularization parameters indicated in

257   Section 4.1.

258   The average of the RMS misfits from one-hundred inversions is ~107 ms and the

259   corresponding normalized misfit $\chi^2 = $ ~1.185 (Figure 4). Assuming that the starting models are

260   independent of each other and all solutions are valid (Korenaga et al., 2000), the mean and the

261   standard deviation of the one-hundred solutions will be our final tomographic model (Figures

262   5&6) and its uncertainty (Figures S1&S2), respectively. The standard deviation has quantified

263   the range of variation (namely uncertainty) in our final Vp models attributed to the different

264   starting models. These values show that the model presents standard deviations <±0.1 km/s in

265   most of the model, indicating a satisfactory control of seismic velocities. As expected, higher

266   values (>±0.2 km/s) are observed in regions with limited ray coverage (Figures S3&S4), like at

267   the edge or the deeper part of the Vp model (Figures 5&6).

268   We have also evaluated the resolution of the tomographic model by performing a set of

269   checkerboard tests (Zelt & Barton, 1998). In this way, a total of 55 checkerboard-type models

270   with eleven different squared cell sizes (4, 6, 8, 10, 12, 14, 16, 18, 20, 25 and 50 km), and with a

271   maximum velocity perturbation of 5% have been tested (Figures S5-S8). For each cell size, five

272   different patterns were created with positive and negative polarity without and with spatial shift

273   of 1/4, 2/4, 3/4 and 4/4 of the cell size contemporary at X, Y and Z directions. Each

274   checkerboard pattern was added to the final tomographic model to create each target model and

275   compute the synthetic travel-times. Before inverting each synthetic travel-times dataset, we

276   added a random Gaussian noise, with a standard deviation corresponding to the average picking

277   uncertainty of ~15 ms, to each synthetic travel-time.

278   After inverting each dataset using the final tomographic model as starting model, we compute

279   the semblance (Figures S9&S10) between the retrieved pattern (Figures S7&S8) and the

280   corresponding target pattern (Figures S5&S6). As in Zelt and Barton (1998), we consider the

281   pattern to be well retrieved for a semblance >0.7. We then compute the average semblance for

282   each cell size and combine them all in a resolution map that depicts the maximum lateral and

283   vertical resolutions of each cell size (Figures S11&S12). All these maps (Figures S11&S12)

284   show that the best resolution areas are located in the central and shallow part of the tomographic

285   model where the minimum cell size that can be retrieved is 4 km. However, the resolution is

286   poor (minimum cell size > 20 km) on the edges and deep part of our model. In these regions the

287   absence of instruments causes a lack of angular coverage because rays cross velocity cells with a

288   common direction, whereas in the deepest part of our model where rays have only horizontal

289   orientation thus decreasing the model resolution.
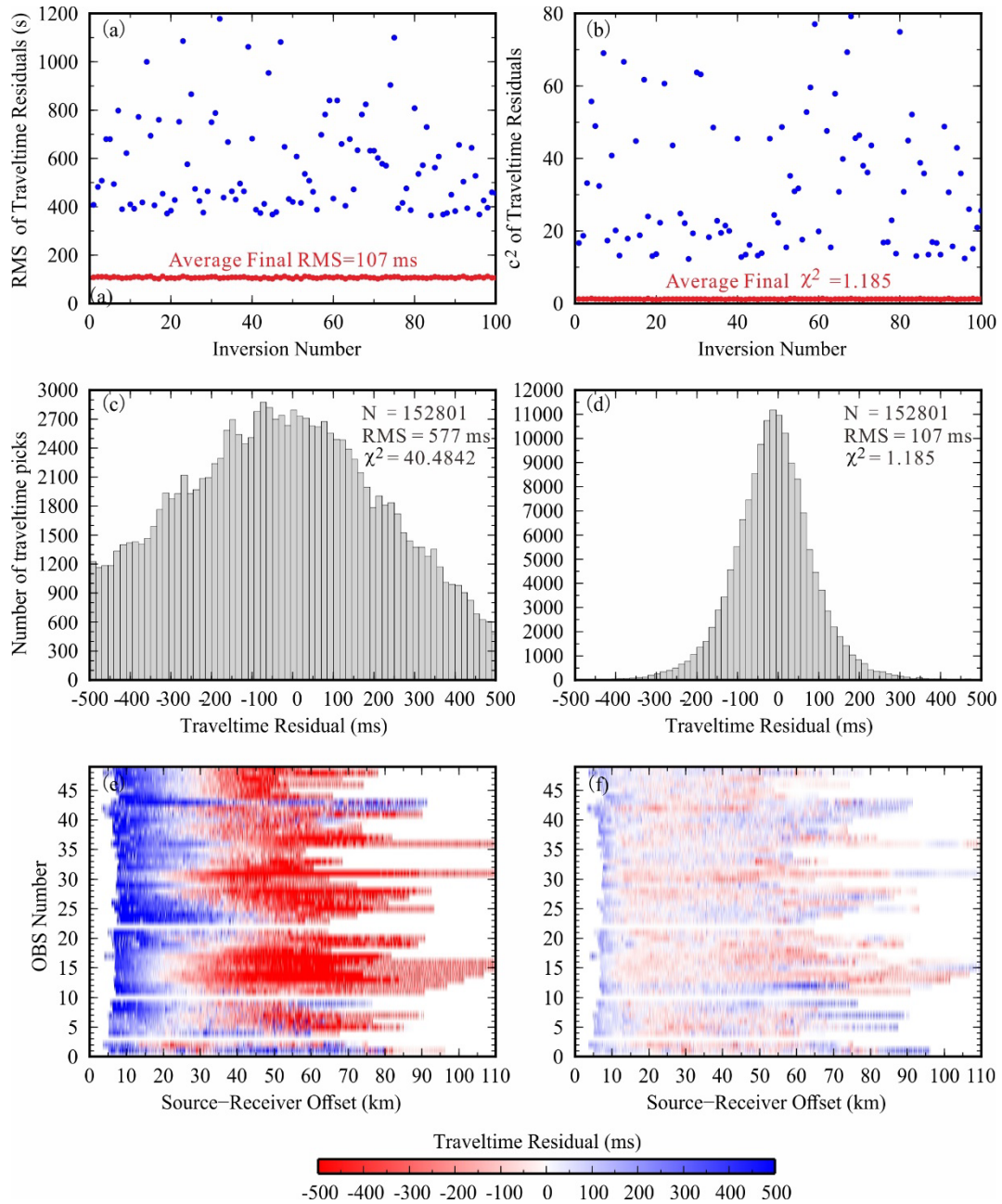
Figure 4. Travel-time residuals distribution for 100 Monte Carlo final solutions. (a) and (b) RMS and χ^2 of travel-time residuals for first (grey dots) and final (red dots) iteration of each Monte Carlo realization, respectively. (c) and (d) Histograms of travel-time residuals for the initial model and the final model, respectively. (e) and (f) Colour-coded travel-time residuals as a function of source-receiver offset (horizontal axis) and OBS number (vertical axis) for the initial model and the final model, respectively.
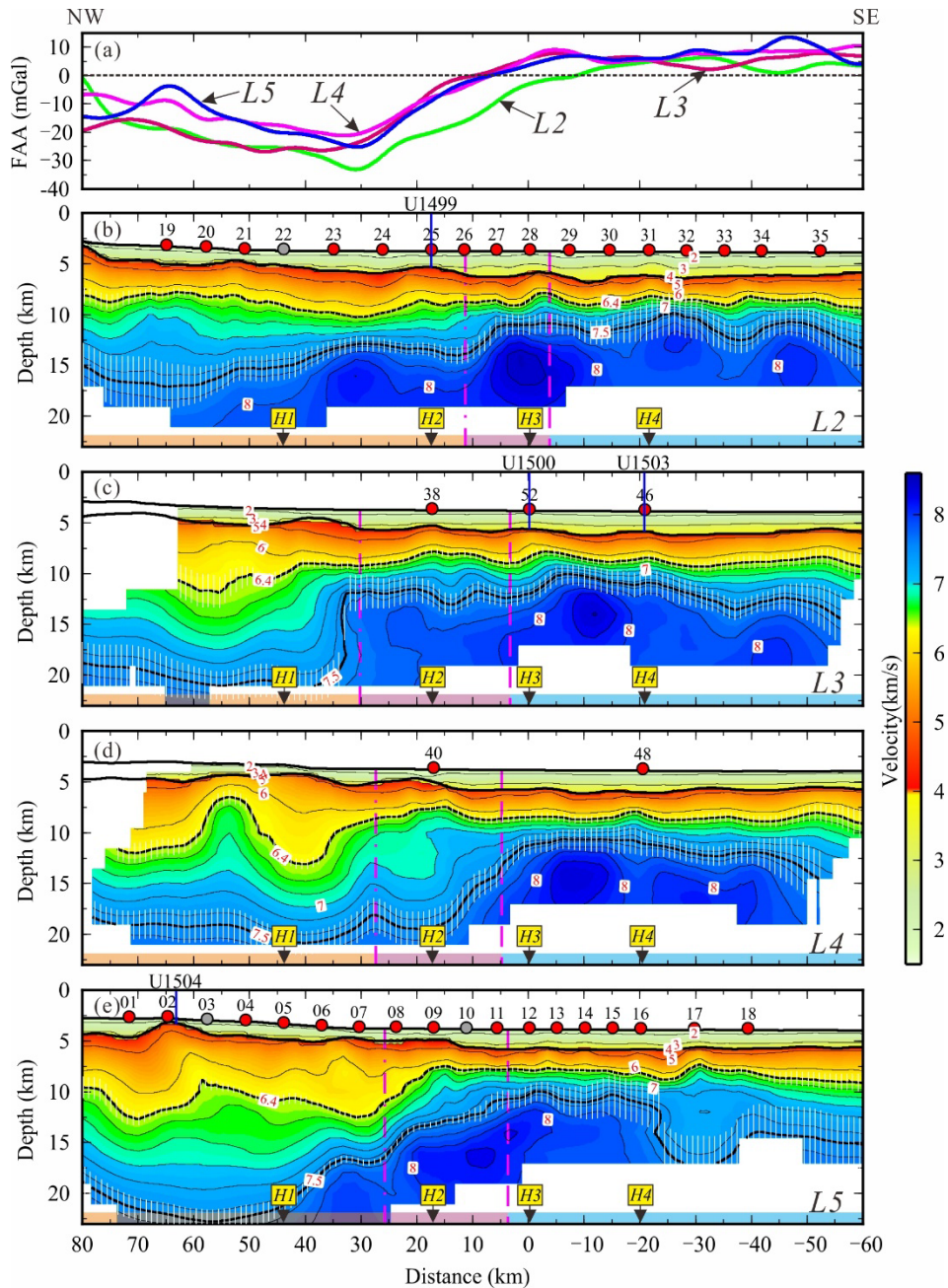
Figure 5. Vertical slices crosscutting the final 3D Vp model and free-air gravity anomaly. (a) Free-air gravity anomalies along shot lines L2, L3, L4 and L5. (b)~(e) Four vertical slices along the extension direction (L2, L3, L4 and L5). (f) Free-air gravity along shot lines H1, H2, H3 and H4. (g)~(j) Four vertical slices along-strike of the margin (H1, H2, H3 and L4). The locations of vertical slices are shown in Figure 2. Masked (white) regions correspond to lack of ray coverage. Velocity contour intervals are 1 km/s in the upper crust and 0.2 km/s in the lower crust, respectively. The 6.4 and 7.5 km/s velocity contours with white vertical bars indicating their

305   uncertainties are shown as bold contours. Red circles and grey circles are the positions of OBSs

306   used in inversion and lost OBS, respectively. The intersection of two vertical slices are shown by

307   black arrows with letter. The drill sites are shown in blue lines. Pink dashed and dashed-dotted

308   lines mark the seaward and landward boundaries of COT domain, respectively. The yellow, pink

309   and blue horizontal bars represent continental, COT and oceanic domains, respectively.
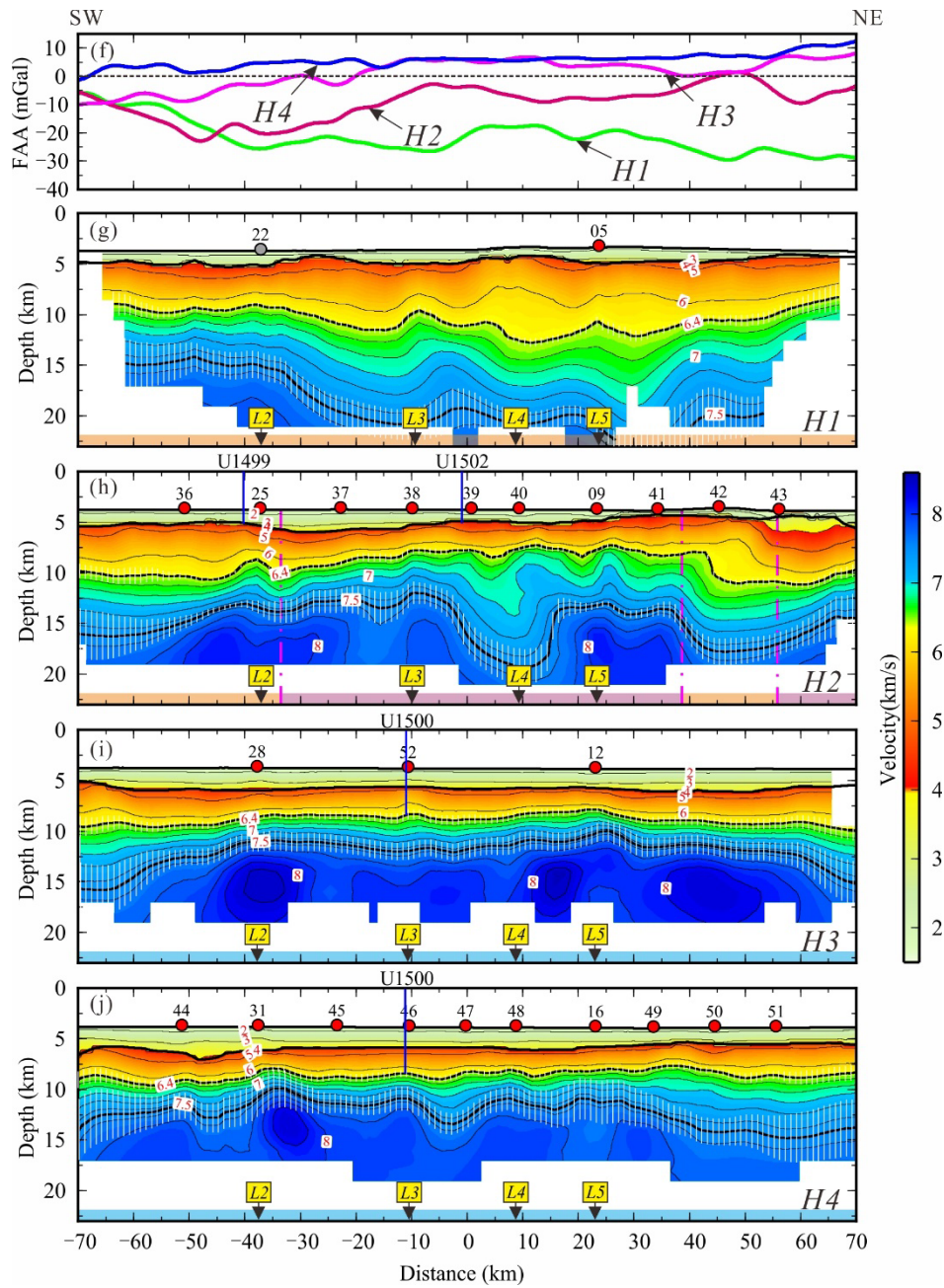
310

311   **Figure 5 (Continuous)**.

312
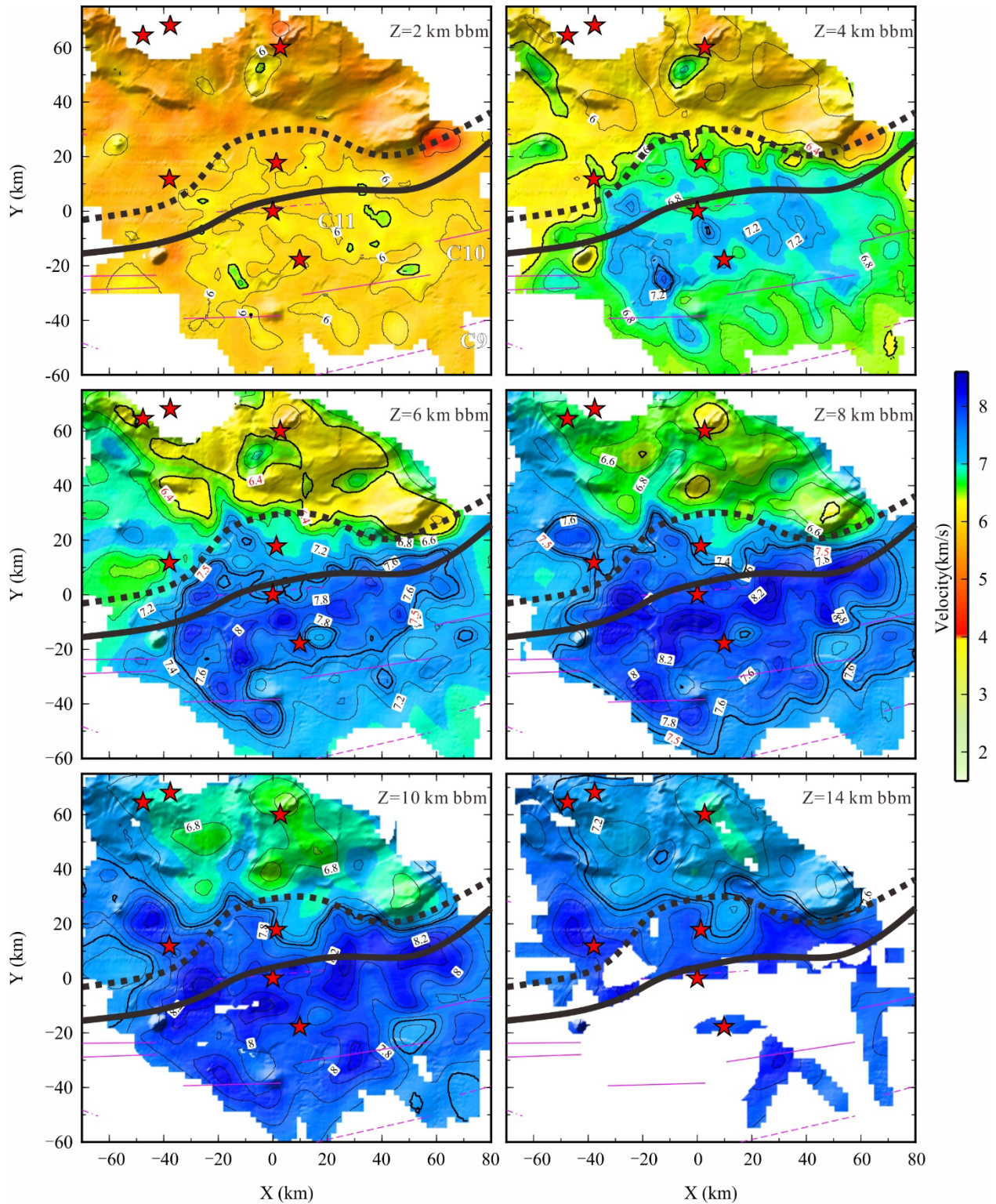
Figure 6. Horizontal slices of the final 3D Vp model at different depths below TOB (bbm).
Masked (white) regions correspond to lack of ray coverage. The scope is shown in Figure 2. The
6.4 and 7.5 km/s velocity contours are shown as bold contours. Black solid and dotted lines mark

316   the seaward and landward boundaries of COT domain, respectively. The other symbols are same

317   as the Figure 2.

318   **5 Results**

319   5.1 3D Vp Tomographic Model

320   The final 3D Vp model is our primary result obtained from tomographic inversion (Figures

321   5&6). Vertical slices in this 3D model (Figure 5) correspond to selected dip lines (L2, L3, L4 and

322   L5) and strike lines (H1, H2, H3 and H4) shown in Figure 2. Depth slices are also shown at 2-14

323   km depth below the TOB (bbm), focusing on the central, best resolved part of the model (Figure

324   6). In addition to the Vp model (Figures 5&6), we also show the velocity gradient (Figures

325   S13&S14) and the velocity perturbation models (Figures S15&S16) obtained on each of the

326   slices. The velocity gradient here referred as to vertical velocity variation versus depth is useful

327   to distinguish seismic layers (Zhao et al., 2013; Tong et al., 2003). The velocity perturbation is

328   obtained by subtracting the starting average 1D ensemble from the final model for each node of

329   the 3D Vp model.

330   The velocity, velocity gradient and velocity perturbation models are used to infer the internal

331   layering of the model, although there is no direct inversion of the interfaces in FAST. The 6.4

332   km/s velocity contour, which displays the sharpest variation in the Vp gradient, is inferred to

333   correspond to the boundary between the upper and lower crusts (Figure S13). Two-dimensional

334   (2D) Vp models with reflective interface (Moho) along L2 (Figure S17a&S17b, from Yuan et

335   al., 2022, in submission to Tectonophysics) are obtained using the Rayinvr (Zelt et al., 1992) and

336   TOMO2D (Korenaga et al., 2000), by comparing with which the 7.5 km/s velocity contour in our

337   3D Vp model is taken as the Moho (Figure S17c). As the velocity at the bottom of continental

338   crust is usually less than 7.0 km/s (Christensen & Mooney, 1995), the part of the model above

339   the inferred Moho showing Vp between 7.0 km/s and 7.5 km/s velocity contours is identified as

340   HVLC. The layer between 6.0 and 6.4 km/s velocity contours is tentatively identified as the

341   middle crust which is a potentially key marker for distinguishing the continental and oceanic

342   crusts (Tatsumi, 2008).

343   The vertical slices along L2, L3, L4 and L5 display the 3D Vp model parallel to the extension

344   direction. In general, they have consistent variations in the velocity structures presenting the

345 seaward uplift of the 7.5 km/s velocity contour (inferred to be a good proxy of the Moho by
346 comparison with the 2D profile) and the resultant tapering of the crustal thickness (Figure 5b-
347 5e). The Moho shallows up from average depths of ~15 km (beneath L2) and ~20 km (beneath
348 L3, L4 and L5) on the landward side to ~11 km on the seaward side, accompanying with
349 reduction of average crustal thickness from ~11-16 km to ~6 km. The seaward variations in
350 crustal structures are also reflected in the free-air gravity anomalies showing gradual transition
351 from negative value to positive value (Figure 5a). Lateral Vp variations indicate similar crustal
352 structure on the seaward side of the 3D model, but great lateral differences on its landward side.
353 In addition to changes in Moho depth, the geometry of 6.4 km/s velocity contour changes from
354 sub-horizontal along L2 to undulating along L3, L4 and L5.

355   The vertical slices along H1, H2, H3 and H4 run parallel to the margin strike and illustrate that
356 the character of Moho depth and crustal thickness along H1 and H2 changes generally more than
357 those along H3 and H4. Further, there is a greater lateral variation in velocity structure along H1
358 and H2 than along H3 and H4 (Figure 5g-5j), which is also expressed in change of the free-air
359 gravity anomaly (Figure 5f). Moho depth along H1 diminishes gradually southwestward, from
360 ~20 km (beneath L5) to ~15 km (beneath L2), causing crustal thinning (Figure 5g). Along H2,
361 there is a prominent low velocity anomaly located between L3 and L5, and the nearby site
362 U1502 drilled altered Mid-Ocean Ridge Basalt (MORB) (Figures 5h&S16). The crustal structure
363 along H3 and H4 is similar, with upper and lower crusts ~3 km thick, respectively, although the
364 lower crust is comparatively slightly thicker on the eastern part of H4.

365   Depth slices further show the Vp lateral variations (Figure 6). The 6.4 km/s velocity occurs as
366 shallow as 2 km bbm in the ocean part, where the Vp and Vp gradient are highest (Figure S14).
367 At 4 km and 6 km bbm, the 6.4 km/s velocity occurs on the entire landward regions, but at 8 km
368 bbm slice it occurs only on the northeastern region. The 7.5 km/s velocity occurs first at 6 km
369 bbm only on the oceanic region, but extends across the entire landward region at 14 km bbm
370 (Figure 6). The variations with depth in distribution of the 6.4 km/s and 7.5 km/s velocities
371 reflect the changes of the upper and lower crust boundary and the Moho resulting from the
372 thinning process (Figure 7a&7b). At 14 km bbm the 7.5 km/s velocity contour near site U1502
373 seems to form a separated circular structure from the surrounding region displaying a lower
374 velocity anomaly (Figures 6&S16).

375   The distribution of middle crust (6.0-6.4 km/s) is uneven, occurring mainly on the northeastern

376   region with thickness of ~4-6 km, but it is largely absent on the seaward side (thickness < 1 km)

377   (Figure 7c). The HVLC occurs widely, ranging from ~1 to 9 km in thickness (Figure 7d).

378   Although measuring the thickness of HVLC is limited by the difference between the Moho (7.5

379   km/s) in our 3D model and the Moho constrained by PmP (Figure S17), the relative thickness

380   variation is well expressed in the 3D volume. The HVLC on the landward region is generally

381   thicker than that on the seaward region, except near site U1502. Further, the HVLC on the

382   northeastern region is thicker than the southwestern region when comparing along-strike

383   variations (Figure 7d).

384   5.2 Identification of Different Basement Domains

385   The lateral variation in the transition from continental to oceanic crust in 3D defines different

386   basement domains (Figure 8). Previous works with MCS, free-air gravity anomaly (Figure 8),

387   magnetic lineations and recent IODP drilling, proposed basement domains in the study area,

388   including thin continental basement, the COT, and oceanic crust (Zhang et al., 2021; Ding et al.,

389   2020). Based on the variations in whole-crust and middle-crust thickness, as well as 1D Vp-

390   depth profiles from our 3D Vp model, we further investigate the extent, structure and nature of

391   the region. We define the lateral geometry of the COT based on seismic velocity distribution

392   with the seaward boundary to be roughly coincident with the zero value of free-air gravity

393   anomaly corresponding to a ~5-6 km crustal thickness (Figures 7&8), while its landward

394   boundary roughly corresponds to the location where continental crust abruptly thins and the

395   largest crustal thickness variation gradient happens (Figures 5, 7, S17). The landward boundary

396   is also roughly consistent with the maximum negative free-air gravity anomaly, except the parts

397   to the west of L2 and to the east of L5 (Figures 5a, 6&10). Moreover, the landward boundary

398   near drill site U1502 is interpreted landward of a circular-shape crustal thickness anomaly

399   (Figure 7a), because the crustal structure has been modified by magmatism during breakup

400   sampled as altered MORB at site U1502 (Larsen et al., 2018b).

401   The oceanic domain extends across the deep-water region at water depth >~3 km. This domain

402   contains distinct magnetic anomalies, interpreted as seafloor spreading lineations (Li et al., 2014;

403   Briais et al., 1993), positive free-air gravity anomaly (Sandwell et al., 2014), and high-amplitude

404   reflections from TOB displaying a flat to slightly hummocky geometry cut by small-offset faults

405   and continuous oceanic Moho reflections in seismic images (Zhang et al., 2021; Ding et al.,

406   2020; Ding et al., 2018). Drilling of fresh MORB at sites U1500 and U1503 supports the oceanic

407   nature of this domain (Childress et al., 2020; Larsen et al., 2018a). Our 3D Vp model shows that

408   the average crustal thickness of this region is ~6 km, although it locally ranges from 4.5 to 9 km

409   (Figure 7a). The seismic velocity structure of the basement displays two characteristic layers

410   with a higher velocity gradient in the upper crust and a gentler velocity gradient in the lower

411   crust (Figure 9a) resembling classical oceanic structure (White et al., 1992).

412   In contrast to the oceanic domain, mainly negative free-air anomalies and no distinct magnetic

413   lineations occur across the continental domain (Li et al., 2014). Syn-rift sediment associated to

414   large-offset faults support a continental rifting style of the basement deformation (Zhang et al.,

415   2021; Ding et al., 2020), confirmed by basement drilling at sites U1501, U1504 and U1505

416   (Larsen et al., 2018b). Our 3D Vp model displays comparatively thicker basement (~8-20 km) in

417   the continental domain (Figure 7a), whose seismic velocity vertical gradient and perturbation are

418   distinct from those of the oceanic domain (Figures S13-S16). A middle crust layer characterised

419   by 6.0-6.4 km/s velocity and >1 km thick seems to only occur here (Figure 7c). The whole-crust

420   thickness, including upper and middle crust and the HVLC, is thicker in the east sector than in

421   the western sector in this domain. The boundary between these two sectors seems to be

422   consistent with the Pearl River Mouth Canyon shown in the bathymetry (Figure 2). Hence, the

423   continental domain is divided into two segments (Figure 8), which will be discussed in detail in

424   next section. The boundary between the two segments appears to project seaward to a NW-SE

425   elongated area of comparatively thinner basement delineated by the 6 km thickness contour

426   (Figure 7a) across the COT and the oceanic domain, which may be coincident with the Zhongnan

427   fracture zone bounding seafloor spreading segments (Cameselle et al., 2017).

428   A ~20 km-width COT occurs between the continental and oceanic domains (Figure 8), as the

429   free-air gravity anomaly increases oceanward from negative to positive (Figure 8), which is

430   coincident with the crustal thinning from ~8-14 km on the landside to ~4.5-9 km on the seaside

431   (Figure 7a). The COT basement has been sampled at site U1502 (e.g., altered MORB),

432   supporting the hybrid type of crust based on the sample at comparative site U1499 (e.g., gravels)

433   and the MCS images, where tapering continental crust may have been overprinted by extrusive

434   and underplated/intrusive magmatic material (Zhang et al., 2021; Ding et al., 2020). Gravity

435   modelling using MCS images for structural constraints has interpreted thin continental basement

436   passing to igneous crust (Nirrengarten et al., 2020). The 1D Vp-depth profiles from the COT
437   domain fall in between typical thin continental and oceanic domains (Figures 9b), which
438   supports hybrid type of crust for the COT basement.
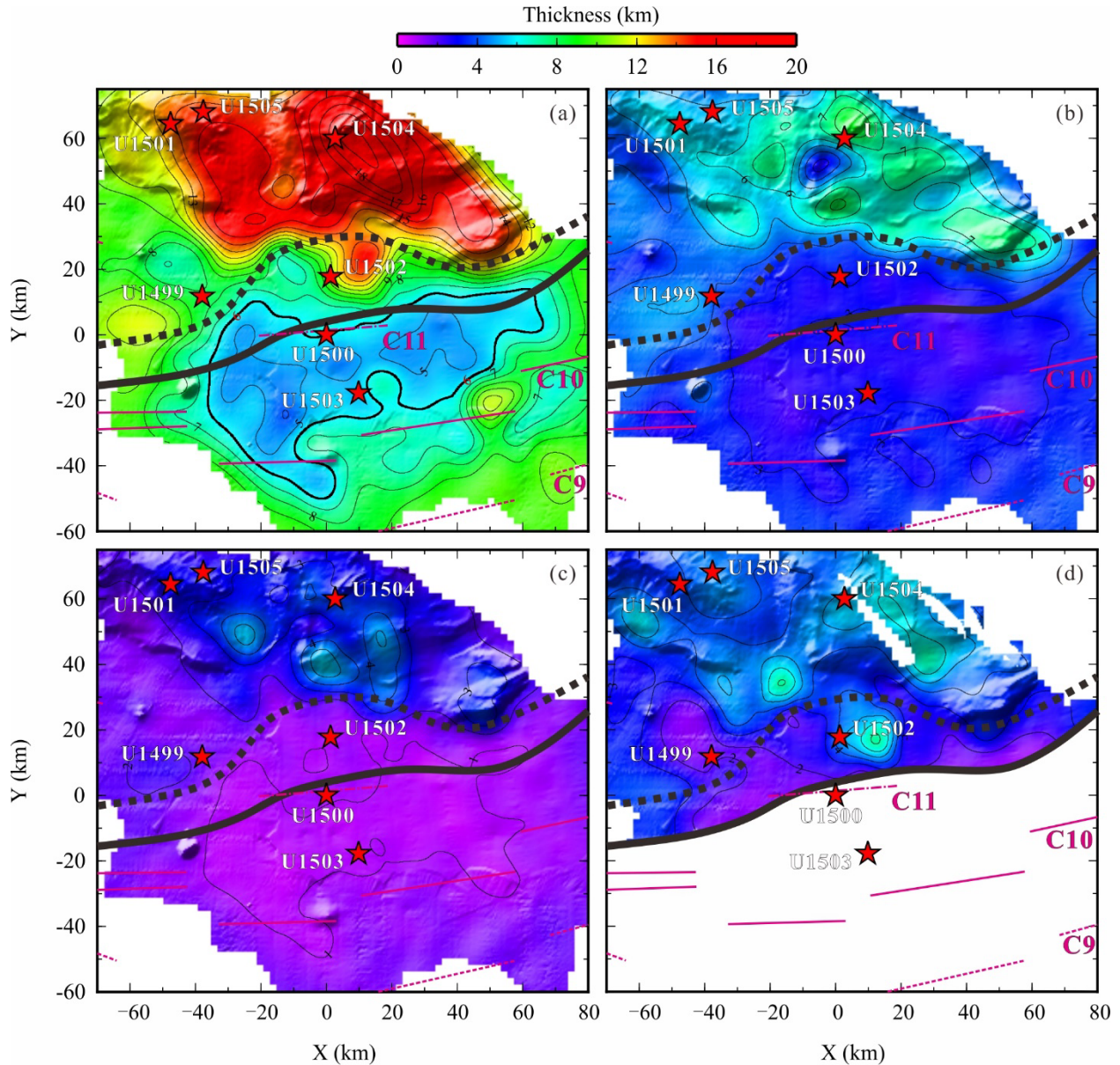
439

440   **Figure 7**. Thickness maps for different layers. (a) Whole crust (between TOB and 7.5 km/s
441   velocity contour). (b) Upper crust (between TOB and 6.4 km/s velocity contour). (c) Middle
442   crust (between 6.0 km/s and 6.4 km/s velocity contours). (d) HVLC (between 7.0 km/s and 7.5
443   km/s velocity contours). It's worth noting that the layer between 7.0 km/s and 7.5 km/s contours
444   in the oceanic domain is masked as it is usually not referred as to HVLC. The thick black solid

445 and dotted lines mark the seaward and landward boundaries of COT domain, respectively. The

446 other symbols are same as Figure 2.

447
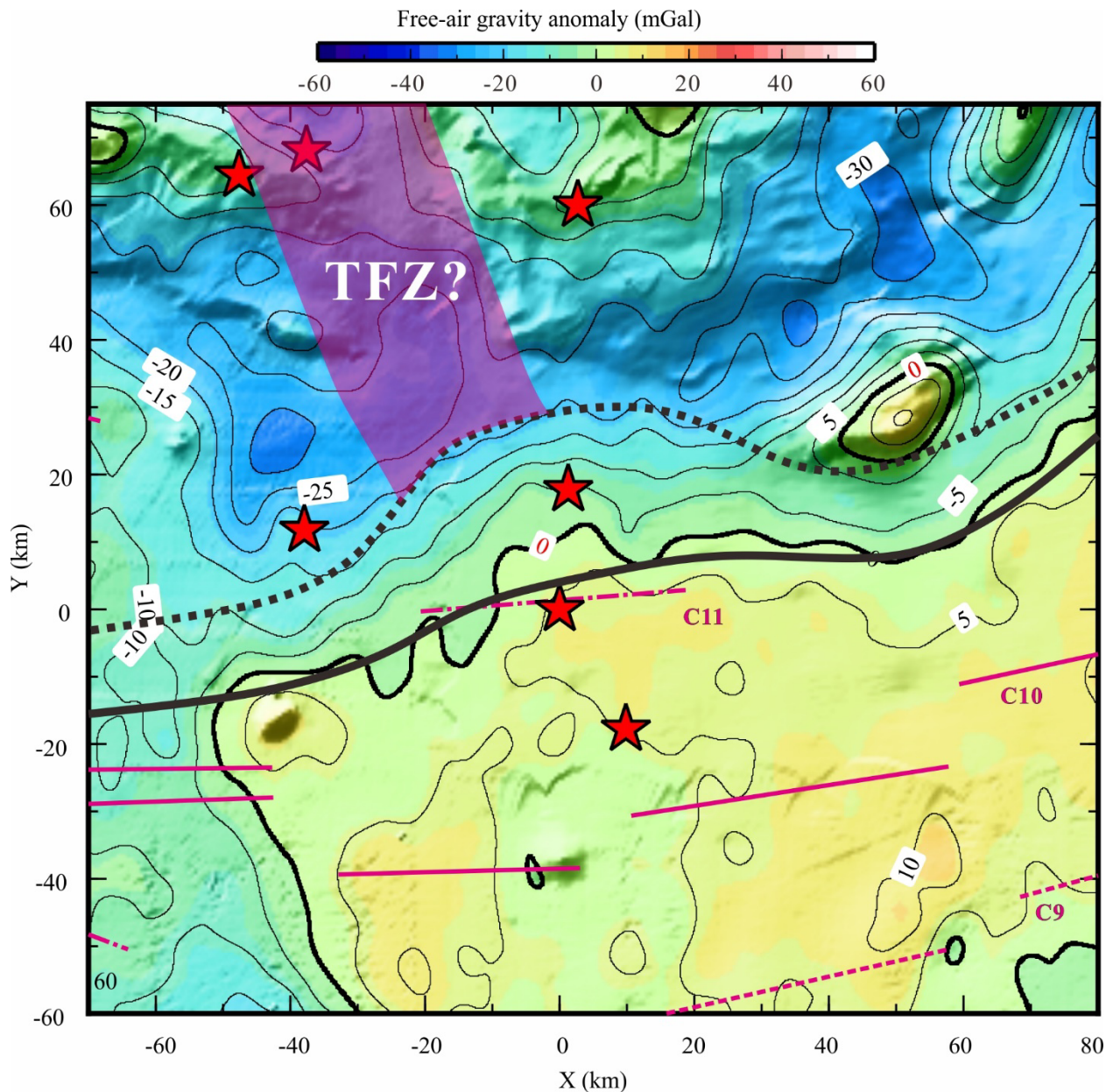
Figure 8. Free-air gravity anomaly map of the study area and identification of different basement

449 domains. The free-air gravity data is from Sandwell et al. (2014). The thick black solid and

450 dotted lines mark the seaward and landward boundaries of COT domain, respectively. The

451 continental and oceanic domains are therefore located on the landward side and on the seaward

452 side, respectively. It is worth noting that a possible transfer fault zone (TFZ) located in the

453   continental domain has further separated the NE tectono-magmatic segment from SW tectonic-

454   dominated segment. The other symbols are same as Figure 2.

455
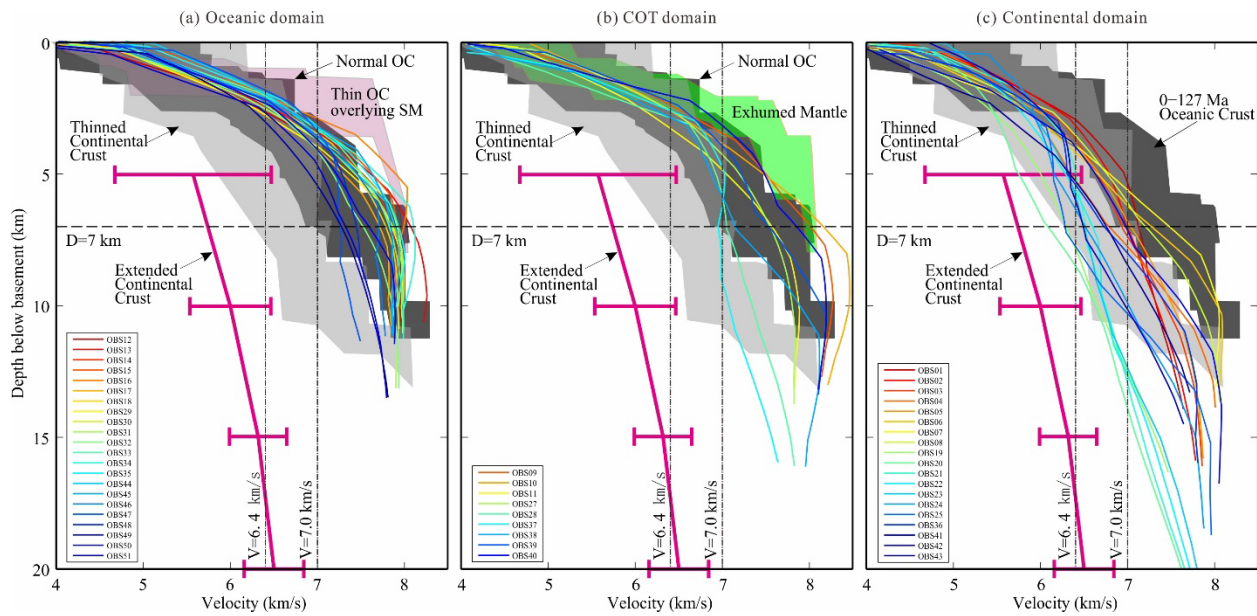
Figure 9. The 1D Vp-depth profiles extracted from the 3D Vp model beneath the OBS stations in (a) the oceanic domain, (b) the COT domain, (c) the continental domain. The dark envelope shows the range of typical velocities for the Atlantic oceanic crust (0-127 Ma) (White et al., 1992). The pink lines with uncertainties indicate extended continental crust (Christensen and Mooney, 1995). The grey envelope indicates the thinned continental crust in the SCS (Liu et al., 2018). The pink envelope and green envelope represent the velocity range of thin oceanic crust overlying serpentinized mantle (Davy et al., 2016; Whitmarsh et al., 1996) and exhumed mantle in the west Iberia margin (Dean et al., 2000).

6 Discussion

    6.1 Along-strike crustal changes during end rifting

    A major outcome of the 3D Vp model is the along-strike variations in the crustal structure of the continental domain (Figures 5&6). Lateral variations include significant changes in the crust and HVLC thickness (Figure 7). The model shows that there are two styes of thinning along-opening direction from the northeastern (NE) segment to the southwestern (SW) segment, separated by a transfer (fault?) zone marked by an abrupt change in crustal thickness and Vp distribution (Figures 6&7). In the SW segment, continental crust thickness thins towards the

472   COT from ~13 km to ~8 km in ~70 km range displaying a comparatively gradual thinning,

473   whereas seaward crustal thinning in the NE segment occurs abrupter from ~20 km to ~8 km in

474   ~30 km range (Figure 7a). Both segments transition to oceanic crust across a narrow COT

475   (Figure 8). The two styles of crustal structure are separated by a ~25 km-width NW-SE trending

476   zone (Figure 8). This narrow segment boundary separating two different kinds of tectonic and

477   magmatic styles possibly represents a transfer fault, perhaps relating to the Baiyun-Liwan Fault

478   Zone defined further landward (Zhao et al., 2019).

479   Contrasting styles of thinning and extension have been described to occur in conjugate

480   margins giving rise to the now classical observation of an asymmetric crustal and tectonic

481   structure (Ranero & Perez-Gussinye, 2010; Hopper et al., 2004). The observed crustal and

482   tectonic asymmetry of conjugate margins led to the term upper-plate margin, in the hanging wall

483   to the inferred lithospheric detachment, and a conjugate lower-plate margin, in the footwall to the

484   detachment (Wernicke, 1995; Lister et al., 1991). Conceptually, upper-plate margin segments

485   might laterally abut a lower-plate margin segment across a transfer fault, causing significant

486   along-strike variation in the crustal structure (Lister, 1986). Along-strike variability from an

487   upper-plate structure to a lower-plate structure have been reported in the SCS (Zhang et al.,

488   2021; Franke et al., 2014; 2011) and for the South Atlantic Angola–Gabon rifted margin (Peron-

489   Pindivic et al., 2015). However, in our study area, there is no MCS images show confident

490   along-strike flip of the detachment polarities (Gao et al., 2015), although it is worth noting that

491   the small-offset faults on the TOB in the NE segment (e.g., Figure 4 in Zhang et al., 2021) are

492   very different from the larger-offset faults (e.g., Figure 13 in Yang et al., 2018) on the TOB in

493   the SW segment, indicating distinct difference in the tectonic deformation between the two

494   segments.

495   Drilling the northern SCS basement found evidence of syn-rift and syn-breakup magmatism

496   (Sun et al., 2019; Larsen et al., 2018b), and the anomalously high Vp 7.0-7.5 km/s of the HVLC

497   can be interpreted as a proxy of syn-rift and syn-breakup mafic magmatic underplating and lower

498   crustal intrusions. HVLC are often attributed to decompression melting of upwelling hot or

499   chemically anomalous asthenosphere (Sallares et al., 2003; Korenaga et al., 2002). Assuming

500   that most of the HVLC is formed by underplating, it implies crustal stretching factor (β) of ~2-9

501   when removing the HVLC thickness (Figure S18a&18b) assuming 32 km as initial thickness (Li

502   et al., 2006). It is however somewhat counterintuitive that the HVLC in the NE segment with

503 smaller β (<~3) is overall thicker than the HVLC in the SW segment with larger β (>~4) (Figures

504 7d&S18b). Significant differences of the initial lithospheric thickness or mantle potential

505 temperature (Bown & White, 1995; White & McKenzie, 1989) in the relatively small study area

506 appear unlikely (Figure S18c & S18d) and thus the origin of the differences during rifting must

507 come from local chemical or structural heterogeneities.

508   Potential local lithospheric heterogeneities include inherited lateral changes in mantle

509 composition, which could have modulated the processes that led to the contrasting styles of

510 thinning and magmatism during rifting. Significant changes in magmatism have been reported

511 related to a comparatively strong tectonic segmentation by transform faults in the Gulf of

512 California (Lizarralde et al., 2007). The inheritance of a heterogenous mantle could lead to

513 abrupt along-strike changes in the interplay between deformation and magmatism during end

514 rifting processes. Locally constrained changes in melt production would also influence the

515 lithospheric thermal structure and the crustal and upper mantle rheology so that the opening in

516 the NE segment was controlled by a balance between tectonic and magmatic additions, whereas

517 opening in the SW segment is comparatively dominated by extensional tectonism. This

518 previously unreported relative small-scale segmentation requires a lithospheric scale transfer

519 fault system that separates two different opening styles and two melt generation systems

520 indicated by the distinct HVLC distribution (Figure 10).

521   6.2 Origin of syn-rift and syn-breakup magmatism

522   The HVLC in the 3D Vp model may represent sills heavily intruding the lower crust, which

523 may relate to the internal reflection packages in the lower crust above the Moho in MCS images

524 (Ding et al., 2020). The age of the altered MORB drilled at site U1502 (Larsen et al., 2018b)

525 supports the existence of significant syn-rift and syn-breakup magmatism. However, the

526 magmatic budget is inferred moderate compared to magma-rich margins because no SDRs are

527 imaged. The main parameters controlling the onset of magmatic activity and magmatic budget

528 include mantle temperature, opening rate, initial lithospheric thickness (Bown and White, 1995;

529 White and McKenzie, 1989), mantle composition (Sun et al., 2019; Korenaga, 2004) and rifting

530 styles (Lu et al., 2021). Mantle temperature is usually suggested as the main factor to control the

531 formation of the two end-member classes of magma-poor and magma-rich rifted margins (Lu et

532 al., 2021; Minshull et al., 2001; White et al., 1987). Previous investigations speculate on the

533   presence of a significant positive mantle thermal anomaly during breakup of the northern SCS

534   (Clift et al., 2015; Nissen et al.,1995b), but clearly any existing thermal anomaly was too small

535   to produce structures typical of magma-rich margins.

536   The Mesozoic paleo-Pacific subduction may have carried abundant fluids into lithosphere

537   prior to the SCS formation (Sun et al., 2019), making its mantle probably different from the

538   north Atlantic rifted margins. An extended phase of rifting occurred in the SCS margins

539   (Cameselle et al., 2020; Franke et al., 2014), and although the main rift event stared in Eocene

540   time and the magmatic event constrained with site U1502 results lasted less than 10 Ma have

541   during which upwelling of asthenosphere generated enhanced magmatism (Ding et al., 2020;

542   Larsen et al., 2018a). However, tectonic extension triggered different magma generation by

543   decompression melting, inferred from the differences in HVLC distribution in the two margin

544   segments (Figure 7d). A possible scenario is that opening rates were significantly different in the

545   two segments and that faster opening of the eastern segment produced larger volume of melt.

546   Alternatively, divergence rates may have been similar along the entire margin sector, but mantle

547   composition differed, and a comparatively more fertile mantle in the eastern segment produced

548   enhanced melt. Although we cannot exclude the first scenario, the second scenario appears more

549   realistic as the NE segment and SW segment may have been located at different tecontic setting

550   in Mesozoic subduction system (Figure 1).

551   6.3 No mantle exhumation at the COT

552   Prior to IODP Expeditions 367/368/368X, magma-poor rifting models of the type of the west

553   Iberia margin were often used to interpret the formation of SCS. As a result, the presence of

554   exhumed and serpentinized mantle was interpreted to occur across the COT of the northern SCS,

555   based on interpretations of MCS profiles (Franke et al., 2014). Alternative interpretations of the

556   northern SCS present seismic images displaying continuous Moho reflections from clear

557   continental domains to oceanic domains, and propose a narrow COT containing an abrupt

558   contact between extended continental crust and oceanic igneous crust (Cameselle et al., 2017). A

559   narrow COT between the continental and oceanic domain is supported by drilling results of

560   IODP Expeditions 367/368/368X (Larsen et al., 2018b), that seem to preclude the existence of

561   exhumed mantle in the northern SCS.

562   The drilling results are interpreted to indicate a COT basement made of extended continental

563   crust heavily modified by igneous additions (Zhang et al., 2021; Ding et al., 2020; Nirrengarten

564   et al., 2020). However, the limited number of IODP drilling sites sampling basement at structural

565   highs do not preclude the presence of mantle exhumed by faulting in the drilling area of IODP

566   Expeditions 367/368/368X. For example, because no basement was reached at site U1499, Yang

567   et al (2018) interpret MCS images supporting mantle exhumation. Wan et al (2021) speculate

568   that although fresh MORBs have been drilled at sites U1500 and U1503, a thin igneous carapace

569   may overlie serpentinized exhumed mantle just as interpreted in the west Iberia rifted margin

570   (Davy et al., 2016), or igneous additions occur after exhumation and serpentinization of the

571   mantle as drilled in the Vavilov and Marsili sub-basins of the Tyrrhenian Sea basin (Prada et al.,

572   2020; 2016; 2015).

573   To evaluate the presence of exhumed and serpentinized mantle we compare 1D Vp-depth

574   profiles beneath OBS station across the COT and oceanic domains with those from other basins

575   where exhumed and serpentinized mantle has been confirmed by drilling (Figure 9). The 1D Vp-

576   depth profiles from the oceanic domain fall into the range of velocities for the Atlantic oceanic

577   crust usually referred as normal oceanic crust (White et al., 1992), and do not overlap with the

578   range of velocities of thin magmatic crust overlying serpentinized mantle (Davy et al., 2016;

579   Whitmarsh et al., 1996) (Figure 9a). Furthermore, the 1D Vp-depth profiles from the COT

580   domain fall outside of the range of velocities for the exhumed mantle (Dean et al., 2000), and

581   they fall between the ranges of velocities for thinned continental crust (Liu et al., 2018) and

582   normal oceanic crust (White et al., 1992) (Figure 9b).

583   In addition, distinct and continuous seismic reflection Moho are well displayed in the MCS

584   profiles in or near the study area (Zhang et al., 2021; Ding et al., 2020; Nirrengarten et al., 2020;

585   Cameselle et al., 2017). Furthermore, wide-angle PmP Moho reflections are observed in seismic

586   records at the triple junction of Pg, PmP and Pn (Figure 3). The origin of PmP reflections has

587   been further verified with 2D forward and inverse modeling including the Moho interface

588   (Figure S17). Hence, all available seismic data including the 3D Vp model indicate that mantle

589   exhumation and serpentinization did not occur during the COT formation of the study area.

590   6.4 Rift-to-drift model

591   Different studies (e.g., Cameselle et al., 2020; Deng et al., 2020) propose that the formation

592 and large-scale evolution of the SCS is similar to the "wide rift mode" of extension (Hopper &

593 Buck, 1996; Buck, 1991). A ~1000 km-wide region of continental crust formed by "basin and

594 ranges" with a crustal architecture characterized by a succession of thin-basement (<~10 km)

595 sub-basins (e.g., the Xisha failed rift and Baiyun-Liwan Sags) separated by basement highs

596 (Cameselle et al., 2020; Clerc et al., 2018; Franke et al., 2014; Savva et al., 2014). These sub-

597 basins possibly evolved as discrete subsystems during early rifting, with final breakup and the

598 transition to seafloor spreading only occurred in one of them (Cameselle et al., 2020). The 3D

599 Vp model provides unprecedented resolution of the lateral crustal variability to study the end

600 phase of rifting and how the deformation localized in 3D (Figure 10).

601   Early stretching deformation is decoupled between the ductile lower crust and the brittle upper

602 crust, with a series of discrete small-scale normal faults cutting TOB (Franke et al., 2014). These

603 comparatively small faults are observed onshore (Nanni et al., 2017) and extend offshore. When

604 the crust is thinned to <~15 km, differences in rheology and the result of the interplay between

605 magmatism and faulting become more evident. In area with a ductile lower crust and limited

606 magmatism, basin-bounding faults develop as detachment surfaces giving rise to fault-controlled

607 thinning like in the Liwan sag with long detachment fault (>100 km) that extends towards the

608 COT characterized by numerous tilted blocks (e.g., along L2, Yang et al., 2018). Thinning

609 towards the COT in the SW segment is gradual as the motion between upper and lower

610 crust/upper mantle is accommodated along the detachment surfaces (Figure 10).

611   In contrast, tectonic deformation is comparatively less intense in the NE segment,

612 accompanied by thicker middle crust and the magmatic production associated to the HVLC

613 (Figure 7c&7d). Local lithospheric heterogeneities may have caused more magma in the NE

614 segment than that in the SW segment and the accommodation space created during the basin

615 opening is filled by a comparatively larger proportion of magmatic intrusions and relatively

616 smaller-offset normal faulting restricted to the upper crust (Figure 10).

617   Deeply penetrating faults are usually inferred to promote the exhumation and eventual

618 exposure at the seafloor of originally deep-seated material, either lower crust or mantle (Reston,

619 2009; Manatschal et al., 2001). However, neither mantle or lower crust exhumation are a

620   requisite in the SCS rifting. The northern SCS magmatism may not only have contributed to

621   form the HVLC, but also potentially used fault systems of the COT to percolate through highly-

622   thinned continental crust, forming the hybrid COT domain of thin continental crust and igneous

623   additions (Figure 10). Final breakup likely occurred rapidly associated to the weakening

624   produced by magmatic diking as lithospheric thinning progressed.

625   The north Atlantic rifted margins have been the most widely studied. Scientists have carried

626   out extensive geological and geophysical surveys to reveal the crustal structure (Minshull et al.,

627   2009), as well as numerous numerical and physical modelling to study what parameters have

628   influenced the rifting styles. A large number of geodynamic and conceptual models have been

629   proposed (Brune et al., 2014; Huisman & Beaumont, 2011; Ranero & Perez-Guissinye, 2010;

630   Whitmarsh et al., 2001), and have been widely applied to other rifted margins. However, the new

631   3D Vp data provides information on the rift-to-drift transition process for the northern SCS that

632   is different from the classic magma-poor and magma-rich rifted margins. In the future, the 3D

633   physical and numerical modelling are proposed to verify and reveal what kinds of parameters

634   mainly control the rifting style which may be very different from that in the Atlantic rifted

635   margins.
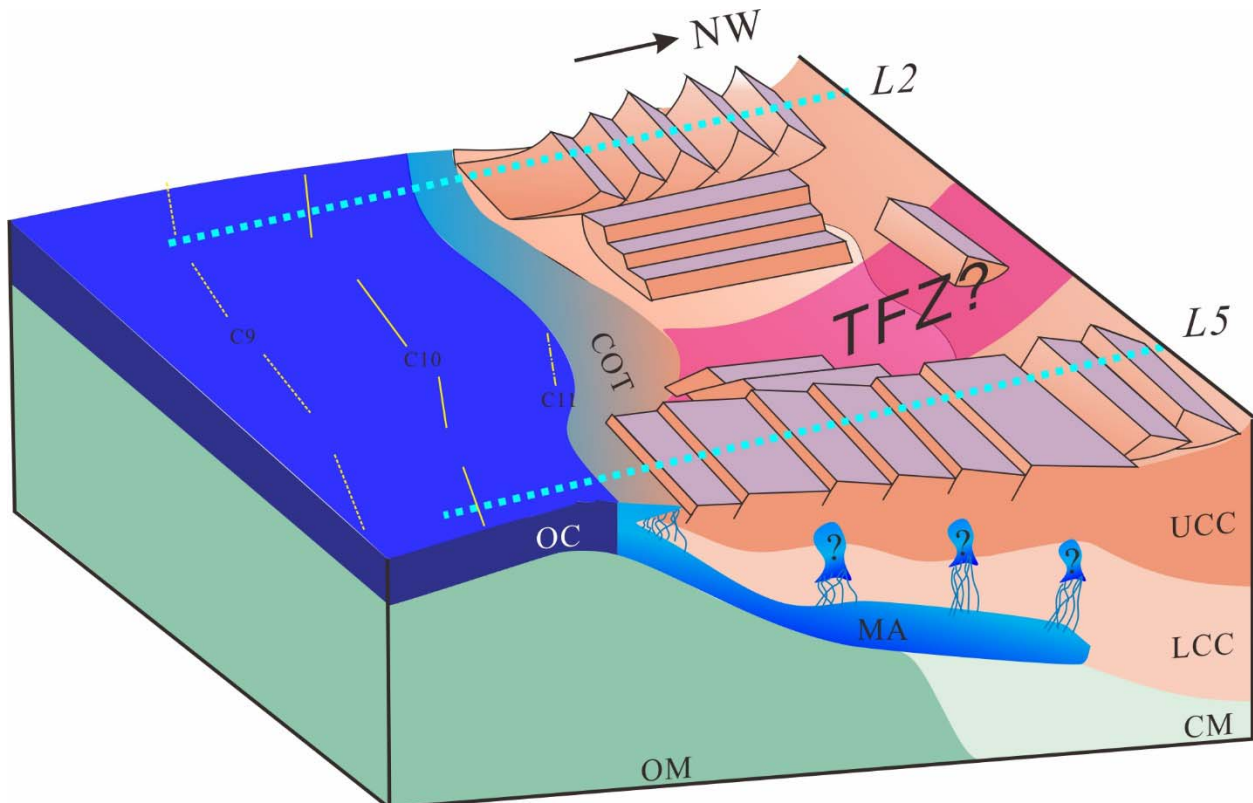
636

637 **Figure 10**. Schematic diagram showing possible geological model with possible tectonics and
638 magmatism during rift-to-drift process in the study area. An abrupt along-strike change in
639 deformation and magmatism occurred from the NE segment to SW segment. Magmatism in the
640 NE segment was abundant and took a significant proportion of the opening leading to a
641 comparatively smaller scale faulting of the upper crust. Whereas the SW segment was dominated
642 by tectonic extension and magmatism played a comparatively minor role during opening. The
643 two contrasting segments were bounded possibly by a transfer fault system that provided the
644 differential slip during opening of the two different crustal thinning styles and the magmatism
645 leading to the different HVLC distribution. The crustal structure along L2 and L5 in cyan lines
646 are shown in Figure 5. UCC: Upper continental crust; LCC: Lower continental crust; OC:
647 Oceanic crust; MA: Magmatic addition; CM: Continental mantle; OM: Oceanic mantle; TFZ:
648 Transfer fault zone.

649 7 Conclusions

650 In order to further reveal the rift-to-drift process in the northern SCS distal margin, a 3D OBS
651 Vp model is obtained using the first-arrival travel-time tomography method. In combination with
652 the geological and geophysical data, we have some new insights as following.

653 1) The 3D Vp distribution determines the extent of the continental, COT and oceanic
654 domains. The continental domain displays significant lateral variations in thickness from the
655 maximum of ~20 km at the NE segment to the minimum of ~8 km at the SW segment. The
656 oceanic domain shows crustal thickness of ~4.5-9 km with an average of ~6 km, with clear
657 oceanic type seismic structure. A narrow COT domain with width of ~20 km occurs between the
658 continental and oceanic domains.

659 2) The NE abrupt thinning and SW gradual thinning of crustal thickness are observed along-
660 strike margin. Meanwhile, the HVLC interpreted as a proxy of syn-rift and syn-breakup magma
661 shows thicker at the NE region of continental domain with smaller β ($<\sim3$) than that at the SW
662 region with larger β ($>\sim4$). We suggest that this indicates the juxtaposition of NE tectono-
663 magmatic segment and SW tectonic-dominated segment, which is bounded possibly by a transfer
664 fault system.

665   3)   The rapid extension during late Eocene may be responsible for the rapid upwelling of the

666 asthenosphere and moderate magma produced by decompression melting. However, the local

667 lithospheric heterogeneities due to Mesozoic paleo-Pacific subduction have caused different

668 magmatic production along the strike of the margin. This magmatic event not only forms the

669 HVLC, but also alters the highly-thin continental crust to form a narrow COT domain with

670 hybrid crust.

671   4)   The segmentation in rifting style observed at the northern SCS is unprecedented and can

672 not easily be explained by current models of rifting. The contrast in extension styles and inferred

673 magmatism, separated by distinct transfer zone may imply that inherited mantle heterogeneities

674 played a major role during rifting. High resolution seismic Vp models are needed to test the

675 significant of segmentation in other rift systems.

Acknowledgments

Open Research

685   The raw data used for P-wave travel-time tomographic inversion in this study is available at

686 Science Data Bank via https://www.scidb.cn/anonymous/ckVyTVpm with CC0 (Zhang J., Zhao,

687 M., & Qiu X., 2022).

References

689 Bown, J. W., & White, R. S. (1995). Effect of finite extension rate on melt generation at rifted

690   continental margins. *Journal of Geophysical Research: Solid Earth, 100(B9)*, 18011-

691   18029, https://doi.org/10.1029/94JB01478

692 Briais, A., Patriat, P., & Tapponnier, P. (1993). Updated interpretation of magnetic anomalies

693   and seafloor spreading stages in the south China Sea: Implications for the Tertiary tectonics

of Southeast Asia. *Journal of Geophysical Research: Solid Earth, 98(B4)*, 6299-6328. https://doi.org/10.1029/92JB02280

Brune, S., Heine, C., Pérez-Gussinyé, M, & Sobolev, S. V. (2014). Rift migration explains continental margin asymmetry and crustal hyper-extension. *Nature Communications, 5*. https://doi.org/10.1038/ncomms5014

Buck, W. R. (1991). Modes of continental lithospheric extension. *Journal of Geophysical Research: Solid Earth, 96(B12)*, 20161-20178. https://doi.org/10.1029/91JB01485

Cameselle, A. L., Ranero, C. R., & Barckhausen, U. (2020). Understanding the 3D formation of a wide rift: the central South China Sea rift system. *Tectonics, 39(12)*, e2019TC006040. https://doi.org/10.1029/2019TC006040

Cameselle, A. L., Ranero, C. R., Franke, D., & Barckhausen, U. (2017). The continent-ocean transition on the northwestern South China Sea. *Basin Research, 29*, 73-95. https://doi.org/10.1111/bre.12137

Cao, J., Sun, J., Xu, H., & Xia, S. (2014). Seismological features of the littoral fault zone in the Pearl River Estuary. *Chinese Journal of Geophysics (in Chinese), 2014, 57(2)*, 498-508. https://doi.org/10.6038/cjg20140215

Cheng, J., Zhang, J., Zhao, M., Du, F., Fan, C., & Wang, X., et al. (2021). Spatial distribution and origin of the high-velocity lower crust in the northeastern South China Sea. *Tectonophysics, 819*, 229086. https://doi.org/10.1016/j.tecto.2021.229086

Childress, L.B., Alvarez Zarikian, C.A., Briais, A., Dadd, K.A., Deng, J.-M., & Höfig, T.W., et al. (2020). Expedition 368X Preliminary Report: South China Sea Rifted Margin. *International Ocean Discovery Program*. https://doi.org/10.14379/iodp.proc.368X.101.2020

Christensen, N. I., & Mooney, W. D. (1995). Seismic velocity structure and composition of the continental crust: A global view. *Journal of Geophysical Research Atmospheres, 100(B6)*, 9761-9788. https://doi.org/10.1029/95JB00259

Clerc, C., Ringenbach, J. C., Jolivet, L., & Ballard, J. F. (2018). Rifted margins: ductile deformation, boudinage, continentward-dipping normal faults and the role of the weak lower crust. Gondwana Research, 53, 20-40. https://doi.org/10.1016/j.gr.2017.04.030

723   Clift, P. D., & Lin, J. (2001). Patterns of extension and magmatism along the continent-ocean
724   boundary, south china margin. *Geological Society London Special Publications, 187(1)*,
725   489-510. https://doi.org/10.1144/GSL.SP.2001.187.01.24

726   Clift, P. D., Brune, S., & Quinteros, J. (2015). Climate changes control offshore crustal structure
727   at South China Sea continental margin. *Earth and Planetary Science Letters, 420*, 66-72.
728   https://doi.org/10.1016/j.epsl.2015.03.032

729   Davy, R. G., Minshull, T. A., Bayrakci, G., Bull, J. M., Klaeschen, D., & Papenberg, C., et
730   al. (2016), Continental hyperextension, mantle exhumation, and thin oceanic crust at the
731   continent-ocean transition, West Iberia: New insights from wide-angle seismic. *Journal of*
732   *Geophysical Research: Solid Earth, 121(5)*, 3177-3199.
733   https://doi.org/10.1002/2016JB012825

734   Dean, S. M., Minshull, T. A., Whitmarsh, R. B., & Louden, K. E. (2000). Deep structure of the
735   ocean-continent transition in the southern Iberia Abyssal Plain from seismic refraction
736   profiles: the IAM-9 transect at 40°20′N. *Journal of Geophysical Research: Solid Earth,*
737   *105(B3)*, 5859-5886. https://doi.org/10.1029/1999JB900301

738   Deng, H., Ren, J., Pang, X., Rey, P. F., & Luo, P., et al. (2020). South China Sea documents the
739   transition from wide continental rift to continental break up. *Nature Communications, 11(1)*,
740   4583. https://doi.org/10.1038/s41467-020-18448-y

741   Ding W., Sun Z., Mohn G., Nirrengarten M., Tugend J., & Manatschal G., et al. (2020). Lateral
742   evolution of the rift-to-drift transition in the South China Sea: Evidence from multi-channel
743   seismic data and IODP Expeditions 367&368 drilling results. *Earth and Planetary Science*
744   *Letters, 531*, 115932. https://doi.org/10.1016/j.epsl.2019.115932

745   Ding, W., Schnabel, M., Franke, D., Ruan A., & Wu, Z. (2012). Crustal structure across the
746   northwestern margin of South China Sea: evidence for magma-poor rifting from a wide-
747   angle seismic profile. *Acta Geologica Sinica-English Edition*, *86(4)*, 854-866.
748   https://doi.org/10.1111/j.1755-6724.2012.00711.x

749   Ding, W., Zhen, S., Dadd, K., Fang, Y., & Li, J. (2018). Structures within the oceanic crust of
750   the central south china sea basin and their implications for oceanic accretionary processes.
751   *Earth and Planetary Science Letters, 488*, 115-125.
752   https://doi.org/10.1016/j.epsl.2018.02.011

753 Fan, C., Xia, S., Zhao, F., Sun, J., Cao, J., & Xu, H., et al. (2017). New insights into the
754   magmatism in the northern margin of the South China Sea: spatial features and volume of
755   intraplate seamounts. *Geochemistry Geophysics Geosystems, 18(6)*, 2216-2239.
756   https://doi.org/10.1002/2016GC006792

757 Franke, D., Barckhausen, U., Baristeas, N., Engels, M., Ladage, S., & Lutz, R., et al. (2011). The
758   continent-ocean transition at the southeastern margin of the South China Sea. *Marine and*
759   *Petroleum Geology, 28(6)*, 1187-1204. https://doi.org/10.1016/j.marpetgeo.2011.01.004

760 Franke, D., Savva, D., Pubellier, M., Steuer, S., Mouly, B., & Auxietre, J. L., et al. (2014). The
761   final rifting evolution in the South China Sea. *Marine and Petroleum Geology, 58*, 704-720.
762   https://doi.org/10.1016/j.marpetgeo.2013.11.020

763 Gao, J., Wu, S., McIntosh, K., Mi, L., Yao, B., & Chen, Z., et al. (2015). The continent–ocean
764   transition at the mid-northern margin of the south china sea. *Tectonophysics, 654*, 1-19
765   https://doi.org/10.1016/j.tecto.2015.03.003

766 Holbrook, W. S., & Kelemen, P. B. (1993). Large igneous province on the us atlantic margin and
767   implications for magmatism during continental breakup. *Nature, 364(6436)*, 433-436.
768   https://doi.org/10.1038/364433a0

769 Hole, J. A., & Zelt, B. C. (1995). Three-dimensional finite-difference reflection travel-times.
770   *Geophysical Journal International, 121(2)*, 427-434. https://doi.org/10.1111/j.1365-
771   246X.1995.tb05723.x

772 Holloway, N. H. (1981). The north Palawan block, Philippines: its relation to the Asian mainland
773   and its role in the evolution of the South China Sea. *Geological Society of Malaysia*
774   *Bulletin, 14*, 19-58. https://doi.org/10.7186/bgsm14198102

775 Hopper, J. R., Funck, T., Tucholke, B. E., Larsen, H. C., Holbrook, W. S., & Louden, K. E., et
776   al. (2004). Continental breakup and the onset of ultraslow seafloor spreading off Flemish
777   cap on the Newfoundland rifted margin. *Geology, 32(1)*, 93-96.
778   https://doi.org/10.1130/G19694.1

779 Hopper, J. R., & Buck, W. R. (1996). The effect of lower crustal flow on continental extension
780   and passive margin formation. *Journal of Geophysical Research: Solid Earth, 101(B9)*,
781   20175-20194. https://doi.org/10.1029/96JB01644

782   Huismans, R., & Beaumont, C. (2011). Depth-dependent extension, two-stage breakup and
783   cratonic   underplating   at   rifted   margins.   *Nature,   473(7345)*,   74-78.
784   https://doi.org/10.1038/nature09988

785   Huismans, R., & Beaumont, C. (2011). Depth-dependent extension, two-stage breakup and
786   cratonic   underplating   at   rifted   margins.   *Nature,   473(7345)*,   74-78.
787   https://doi.org/10.1038/nature09988

788   Jian, Z., Larsen, H.C., Alvarez Zarikian, C.A., Sun, Z., Stock, J.M., Klaus, A., et al. (2018). Site
789   U1505. *In: Proceedings of the International Ocean Discovery Program, 367/368*.
790   https://doi.org/10.14379/iodp.proc.367368.109.2018

791   Korenaga, J., Holbrook, W. S., Kent, G. M., Kelemen, P. B., Detrick, R. S., & Larsen, H. C., et
792   al. (2000). Crustal structure of the southeast Greenland margin from joint refraction and
793   reflection seismic tomography. *Journal of Geophysical Research: Solid Earth, 105(B9)*,
794   21591-21614. https://doi.org/10.1029/2000JB900188

795   Korenaga, J., Kelemen P.B., & Holbrook W. S. (2002) Methods for resolving the origin of large
796   igneous provinces from crustal seismology. *Journal of Geophysical Research: Solid Earth,
797   107(B9)*, 1-27. https://doi.org/10.1029/2001JB001030

798   Korenaga J. (2004). Mantle mixing and continental breakup magmatism. *Earth and Planetary
799   Science Letters, 218(3-4)*, 463-473. https://doi.org/10.1016/S0012-821X(03)00674-5

800   Larsen, H.C., Sun, Z., Stock, J.M., Jian, Z., Alvarez Zarikian, C.A., & Klaus, A., et al. (2018a).
801   Expedition 367/368 summary. *In: Proceedings of the International Ocean Discovery
802   Program, 367/368*. https://doi.org/10.14379/iodp.proc.367368.101.2018

803   Larsen, H. C., Mohn, G., Nirrengarten, M., Sun Z., Stock J., & Jian Z., et al. (2018b). Rapid
804   transition from continental breakup to igneous oceanic crust in the South China Sea. *Nature
805   Geoscience, 11*, 782-789. https://doi.org/10.1038/s41561-018-0198-1

806   Lavier, L. L., & Manatschal, G. (2006). A mechanism to thin the continental lithosphere at
807   magma-poor margins. Nature, 440(7082), 324-328. https://doi.org/10.1038/nature04608

808   Lei, C., Alves, T. M., Ren, J., Pang, X., Yang, L. & Liu, J. (2019). Depositional architecture and
809   structural evolution of a region immediately inboard of the locus of continental breakup
810   (Liwan sub-basin, South Shina Sea). *Geological Society of America Bulletin, 131(7-8)*,
811   1059-1074. https://doi.org/10.1130/B35001.1

812 Li, C. F., Xu, X., Lin, J., Sun, Z., & Zhu J., et al. (2014). Ages and magnetic structures of the
813   South China Sea constrained by deep tow magnetic surveys and IODP Expedition 349.
814   *Geochemistry,   Geophysics,   Geosystems,   15*,   4958-4983.
815   https://doi.org/10.1002/2014GC005567

816 Li, F., Sun, Z., & Yang, H. (2018). Possible spatial distribution of the Mesozoic volcanic arc in
817   the present-day South China Sea continental margin and its tectonic implications. *Journal of*
818   *Geophysical Research: Solid Earth*, 123, 6215-6235. https://doi.org/10.1029/2017JB014861

819 Li, S., Mooney, W. D., & Fan, J. (2006). Crustal structure of mainland China from deep seismic
820   sounding   data.   *Tectonophysics,   420(1-2)*,   239-252.
821   https://doi.org/10.1016/j.tecto.2006.01.026

822 Li, Z. X., & Li, X. H. (2007). Formation of the 1300-km-wide intracontinental orogen and
823   postorogenic magmatic province in Mesozoic South China: a flat-slab subduction model.
824   *Geology, 35(2)*, 179-182. https://doi.org/10.1130/G23193A.1

825 Lister, G. S., Etheridge, M. A., & Symonds, P. A. (1986). Detachment faulting and the evolution
826   of passive continental margins. *Geology, 14(3)*, 246-250. https://doi.org/10.1130/0091-
827   7613(1986)14<246:DFATEO>2.0.CO;2

828 Lister, G. S., Etheridge, M. A., & Symonds, P. A. (1991). Detachment models for the formation
829   of   passive   continental   margins.   *Tectonics,   10(5)*,   1038-1064.
830   https://doi.org/10.1029/90TC01007

831 Liu, S., Zhao, M., Sibuet, J. C., Qiu, X., Wu, J., & Zhang, J., et al. (2018). Geophysical
832   constraints on the lithospheric structure in the northeastern South China Sea and its
833   implications for the South China Sea geodynamics. *Tectonophysics, 742*,101-119.
834   https://doi.org/10.1016/j.tecto.2018.06.002

835 Lizarralde, D., Axen, G., Brown, H., Fletcher, J. & Gonzalez-Fernandez, A., et al. (2007).
836   Variation in styles of rifting in the Gulf of California. *Nature, 448*, 466-469.
837   https://doi.org/10.1038/nature06035

838 Lu, G., & Huismans, R. S. (2021). Melt volume at Atlantic volcanic rifted margins controlled by
839   depth-dependent extension and mantle temperature. *Nature Communications, 12*, 3894.
840   https://doi.org/10.1038/s41467-021-23981-5

841 Manatschal, G., Froitzheim, N., Rubenach, M., & Turrin, B. D. (2001). The role of detachment
842   faulting in the formation of an ocean-continent transition: insights from the Iberia Abyssal

843   Plain. *Geological   Society   London   Special   Publications,   187(1)*,   405-428.
844   https://doi.org/10.1144/GSL.SP.2001.187.01.20

845 Mckenzie, D. (1978). Some remarks on the development of sedimentary basins. *Earth and*
846   *Planetary Science Letters, 40(1)*, 25-32. https://doi.org/10.1016/0012-821X(78)90071-7

847 Minshull, T. A. (2009). Geophysical characterisation of the ocean-continent transition at magma-
848   poor   rifted   margins.   *Comptes   Rendus   Geoscience,   341(5)*,   382-393.
849   https://doi.org/10.1016/j.crte.2008.09.003

850 Minshull, T. A., Dean, S. M., White, R. S., & Whitmarsh, R. B. (2001). Anomalous melt
851   production after continental break-up in the southern Iberia Abyssal Plain. *Geological*
852   *Society   London   Special   Publications,   187(1)*,   537-550.
853   https://doi.org/10.1144/GSL.SP.2001.187.01.26

854 Nanni, U., Pubellier, M., Chan, L. S., & Sewell, R. J. (2017). Rifting and reactivation of a
855   Cretaceous structural belt at the northern margin of the South China Sea. *Journal of Asian*
856   *Earth Sciences, 136*, 110-123. https://doi.org/10.1016/j.jseaes.2017.01.008

857 Nirrengarten M., Mohn G., Kusznir N. J., Sapin F., Despinois F., & Pubellier M., et al. (2020).
858   Extension modes and breakup processes of the southeast China-Northwest Palawan
859   conjugate   rifted   margins.   *Marine   and   Petroleum   Geology,   113*,   104123.
860   https://doi.org/10.1016/j.marpetgeo.2019.104123

861 Nissen, S. S., Hayes, D. E., Buhl, P., Diebold, J., Bochu, Y., & Zeng, W., et al. (1995a). Deep
862   penetration seismic soundings across the northern margin of the South China Sea. *Journal*
863   *of   Geophysical   Research: Solid   Earth,   100(B11)*,   22407-
864   22433. https://doi.org/10.1029/95JB01866

865 Nissen, S. S., Hayes, D. E., Bochu, Y., Zeng, W., Chen, Y., & Nu, X. (1995b), Gravity, heat
866   flow, and seismic constraints on the processes of crustal extension: Northern margin of the
867   South China Sea, *Journal of Geophysical Research: Solid Earth, 100(B11)*, 22447-22483
868   https://doi.org/10.1029/95JB01868

869 Paton, D. A., Pindell, J., Mcdermott, K., Bellingham, P., & Horn, B. (2017). Evolution of
870   seaward-dipping reflectors at the onset of oceanic crust formation at volcanic passive
871   margins: insights   from   the   south   atlantic.   *Geology,   45(5)*,   439-442.
872   https://doi.org/10.1130/G38706.1

Perez-Gussiny, M., & Reston, T. J. (2001). Rheological evolution during extension at nonvolcanic rifted margins onset of serpentinization and development of detachments leading to continental breakup. *Journal of Geophysical Research: Solid Earth, 106(B3)*, 3961-3975, https://doi.org/10.1029/2000JB900325

Peron-Pinvidic, G., & Manatschal, G. (2010). From microcontinents to extensional allochthons: witnesses of how continents rift and break apart?. *Petroleum Geoscience, 16(3)*, 189-197. https://doi.org/10.1016/j.physio.2015.03.3679

Peron-Pinvidic, G., Manatschal, G., & Osmundsen, P. T. (2013). Structural comparison of archetypal Atlantic rifted margins: A review of observations and concepts. *Marine and Petroleum Geology*, *43*, 21-47. https://doi.org/10.1016/j.marpetgeo.2013.02.002

Peron-Pinvidic, G., Manatschal, G., Masini, E., Sutra, E., & Unternehr, P. (2015). Unravelling the along-strike variability of the Angola-Gabon rifted margin: a mapping approach. Geological Society London Special Publications, 438(1). http://doi.org/10.1144/SP438.1

Prada, M., Ranero, C. R., Sallares, V., Zitellini, N., & Grevemeyer, I. (2016). Mantle exhumation and sequence of magmatic events in the Magnaghi–Vavilov basin (central Tyrrhenian, Italy): New constraints from geological and geophysical observations. *Tectonophysics, 689*, 133-142. https://doi.org/10.1016/j.tecto.2016.01.041

Prada, M., Sallares, V., Ranero, C. R., Vendrell, M. G., Grevemeyer, I., & Zitellini, N., et al. (2015). The complex 3-D transition from continental crust to backarc magmatism and exhumed mantle in the Central Tyrrhenian basin. *Geophysical Journal International*, 203(1), 63-78. https://doi.org/10.1093/gji/ggv271

Prada, M., Ranero, C.R., Sallares, V., Grevemeyer, I., de Franco, R., Gervasi, A., Zitellini, N., The structure of Mediterranean arcs: New insights from the Calabrian Arc subduction system, Earth and Planetary Science Letters, vol.548, 116480, https://doi.org/10.1016/j.epsl.2020.116480. 2020

Pubellier, M., & Meresse, F. (2013). Phanerozoic growth of Asia: geodynamic processes and evolution. *Journal of Asian earth sciences, 72*, 118-128. https://doi.org/10.1016/j.jseaes.2012.06.013

Qiu, X., Ye, S., Wu, S., Shi, X., Zhou, D., & Xia, K., et al. (2001). Crustal structure across the Xisha Trough, northwestern South China Sea. *Tectonophysics, 341(1-4)*, 179-193. https://doi.org/10.1016/S0040-1951(01)00222-0

904 Ranero, C. R., & Pérez-Gussinyé, M. (2010). Sequential faulting explains the asymmetry and
905   extension discrepancy of conjugate margins. *Nature, 468(7321)*, 294-299.
906   https://doi.org/10.1038/nature09520

907 Reston, T. J. (2009). The structure, evolution and symmetry of the magma-poor rifted margins of
908   the North and Central Atlantic: A synthesis. *Tectonophysics, 468*, 6-27.
909   https://doi.org/10.1016/j.tecto.2008.09.002

910 Sallares, V., Charvis P., Flueh E. R., & Bialas J. (2003). Seismic structure of Cocos and Malpelo
911   Volcanic Ridges and implications for hot spot-ridge interaction, *Journal of Geophysical
912   Research: Solid Earth, 108(B12),* 2564. https://doi.org/10.1029/2003JB002431

913 Sandwell, D. T., Mueller, R. D., Smith, W. H. F., Garcia, E., & Francis, R. (2014). New global
914   marine gravity model from Cryosat-2 and Jason-1 reveals buried tectonic structure. *Science,
915   346(6205)*, 65-7. https://doi.org/10.1126/science.1258213

916 Savva, D., Pubellier, M., Franke, D., Chamot-Rooke, N., Meresse, F., & Steuer, S., et al. (2014).
917   Different expressions of rifting on the South China Sea margins. *Marine and Petroleum
918   Geology, 58*, 579-598. https://doi.org/10.1016/j.marpetgeo.2014.05.023

919 Shaw, P. R., & Orcutt, J. A. (1985). Waveform inversion of seismic refraction data and
920   applications to young pacific crust. *Geophysical Journal of the Royal Astronomical Society,
921   82(3)*, 375-414. https://doi.org/10.1111/j.1365-246X.1985.tb05143.x

922 Stock, J.M., Sun, Z., Klaus, A., Larsen, H.C., Jian, Z., & Alvarez Zarikian, C.A., et al.
923   (2018). Site U1500. *In: Proceedings of the International Ocean Discovery Program,
924   367/368*. https://doi.org/10.14379/iodp.proc.367368.104.2018

925 Sun, Z., Lin, J., Qiu, N., Jian, Z., Wang, P. X., & Pang, X., et al. (2019). The role of magmatism
926   in the thinning and breakup of the south china sea continental margin. *National Science
927   Review, 6(5)*, 871-876. https://doi.org/10.1093/nsr/nwz116

928 Sun, Z., Stock, J., Jian, Z., McIntosh, K., Alvarez Zarikian, C.A., & Klaus, A., 2016. Expedition
929   367/368 Scientific Prospectus: South China Sea Rifted Margin. *International Ocean
930   Discovery Program*. https://doi.org/10.14379/iodp.sp.367368.2016

931 Sun, Z., Stock, J.M., Klaus, A., Larsen, H.C., Jian, Z., & Alvarez Zarikian, C.A., et al.
932   (2018). Site U1499. *In: Proceedings of the International Ocean Discovery Program,
933   367/368*. https://doi.org/10.14379/iodp.proc.367368.103.2018

934   Sutra, E., & Manatschal, G. (2012). How does the continental crust thin in a hyperextended rifted
935   margin? Insights from the Iberia margin. *Geology, 40(2)*, 139-142.
936   https://doi.org/10.1130/G32786.1

937   Tatsumi, Y. (2008). Making continental crust: The sanukitoid connection. *Chinese Science
938   Bulletin, 53*, 1620-1633. https://doi.org/10.1007/s11434-008-0185-9

939   Taylor, B., & Hayes, D. E. (1983). Origin and history of the south China sea basin. *The Tectonic
940   and Geologic Evolution of Southeast Asian Seas and Islands: Part 2*, 23-56.

941   Tong, C. H., Barton, P. J., White, R. S., Sinha, M. C., Singh, S. C., & Pye, J. W., et al. (2003).
942   Influence of enhanced melt supply on upper crustal structure at a mid-ocean ridge
943   discontinuity: A three-dimensional seismic tomographic study of 9° N East Pacific Rise.
944   *Journal of Geophysical Research: Solid Earth, 108(B10)*, 2464.
945   https://doi.org/10.1029/2002JB002163

946   Tucholke, B. E., Sawyer, D. S., & Sibuet, J. C. (2007). Breakup of the Newfoundland-Iberia rift.
947   *Geological Society London Special Publications, 282(1)*, 9-46.
948   https://doi.org/10.1144/SP282.2

949   Vidale, J. (1988). Finite-difference calculation of travel-times. *Bulletin of the Seismological
950   Society of America, 78 (6)*, 2062–2076. https://doi.org/10.1785/BSSA0780062062

951   Wan, X., Li, C. F., Zhao, M., He, E., Liu, S., Qiu, X., et al (2019). Seismic velocity structure of
952   the magnetic quiet zone and continent-ocean boundary in the northeastern South China Sea.
953   *Journal of Geophysical Research: Solid Earth, 124*, 11866-11899.
954   https://doi.org/10.1029/2019JB017785

955   Wang, J., Zhao, M., Qiu, X., Sibuet, J. C., He, E., & Zhang, J., et al. (2016). 3D seismic structure
956   of the Zhenbei-Huangyan seamounts chain in the East Sub-basin of the South China Sea
957   and its mechanism of formation. *Geological Journal, 51(S1)*, 448-
958   463. https://doi.org/10.1002/gj.2781

959   Wang, P., Huang, C. Y., Lin, J., Jian, Z., Sun, Z., & Zhao, M. (2019). The south china sea is not
960   a mini-atlantic: plate-edge rifting vs intra-plate rifting. *National Science Review, 6*, 902-
961   913. https://doi.org/10.1093/nsr/nwz135

962   Wang, Q., Zhao, M., Zhang, H., Zhang, J., He, E., Yuan, Y., & Qiu, X. (2020). Crustal velocity
963   structure of the Northwest Sub-basin of the South China Sea based on seismic data

964   reprocessing. *Science China Earth Sciences, 63(11),* 1791-
965   806.https://doi.org/10.1007/s11430-020-9654-4

966 Wang, T. K., Chen, M. K., Lee, C. S., & Xia, K. (2006). Seismic imaging of the transitional crust
967   across the northeastern margin of the South China Sea. *Tectonophysics, 412(3-4)*, 237-254.
968   https://doi.org/10.1016/j.tecto.2005.10.039

969 Wei, X., Ruan, A., Zhao, M., Qiu, X., Li, J., & Zhu, J., et al. (2011). A wide-angle OBS profile
970   across Dongsha Uplift and Chaoshan Depression in the mid-northern South China Sea.
971   *Chinese Journal of Geophysics (in Chinese), 2011, 54(12)*, 3325-3335.
972   https://doi.org/10.3969/j.issn.0001-5733.2011.12.030

973 Wernicke, B. (1995). Low-angle normal faults and seismicity: A review. *Journal of Geophysical
974   Research: Solid Earth, 100(B10),* 20159-20174. https://doi.org/10.1029/95JB01911

975 Wessel, P., Smith, W. H. F., Scharroo, R., Luis, J., & Wobbe, F. (2013). Generic Mapping Tools:
976   Improved Version Released. *Eos, Transactions American Geophysical Union, 94(45)*, 409–
977   410. https://doi.org/10.1002/2013EO450001

978 White, R. S., Mckenzie, D., & O"Nions, R. K. (1992). Oceanic crustal thickness from seismic
979   measurements and rare earth element inversions. *Journal of Geophysical Research: Solid
980   Earth, 97(B13)*, 19683-19715. https://doi.org/10.1029/92JB01749

981 White, R. S., Spence, G. D., Fowler, S. R., Mckenzie, D. P., Westbrook, G. K., & Bowen, A. N.
982   (1987). Magmatism at rifted continental margins. *Nature, 330(6147)*, 439-444.
983   https://doi.org/10.1038/330439a0

984 White, R., & McKenzie, D. (1989). Magmatism at rift zones: the generation of volcanic
985   continental margins and flood basalts. *Journal of Geophysical Research: Solid Earth,
986   94(B6),* 7685-7729. https://doi.org/10.1029/JB094iB06p07685

987 Whitmarsh, R. B., Manatschal, G., & Minshull, T. B. (2001). Evolution of magma-poor
988   continental margins from rifting to seafloor spreading. *Nature, 413(6852)*, 150-4.
989   https://doi.org/10.1016/B978-0-444-56357-6.00008-1

990 Whitmarsh, R. B., Manatschal, G., & Minshull, T. B. (2001). Evolution of magma-poor
991   continental margins from rifting to seafloor spreading. *Nature, 413(6852)*, 150-4.
992   https://doi.org/10.1016/B978-0-444-56357-6.00008-1

993 Whitmarsh, R. B., White, R. S., Horsefield, S. J., Sibuet, J.-C., Recq, M., & Louvel,
994   V. (1996). The ocean-continent boundary off the western continental margin of Iberia:

Crustal structure west of Galicia Bank. *Journal of Geophysical Research: Solid Earth, 101(B12)*, 28291- 28314. https://doi.org/10.1029/96JB02579

Wilcock W (2011). Tlpicker users' manual. http://faculty.washington.edu/wilcock/?page_id=39.

Yan, P., Hui, D., Liu, H., Zhang, Z., & Jiang, Y. (2006). The temporal and spatial distribution of volcanism in the South China Sea region. *Journal of Asian Earth Sciences, 27(5)*, 647-659. https://doi.org/10.1016/j.jseaes.2005.06.005

Yan, P., Zhou, D., & Liu, Z. (2001). A crustal structure profile across the northern continental margin of the south china sea. *Tectonophysics, 338(1)*, 1-21. https://doi.org/10.1016/S0040-1951(01)00062-2

Yang, F., Zhang, J., Du, F., Wang, Q., Pang, X., Zhao, M., & Qiu, X. (2020). A new method for shots and OBSs' relocation applying in three-dimensional seismic survey. *Chinese Journal of Geophysics (in Chinese), 63(2)*, 766-777. https://doi.org/10.6038/cjg2020N0150

Yang, L., Ren, J., McIntosh, K., Pang, X., Lei, C., & Zhao, Y. (2018). The structure and evolution of deepwater basins in the distal margin of the northern South China Sea and their implications for the formation of the continental margin. *Marine and Petroleum Geology, 92*, 234-254. https://doi.org/10.1016/j.marpetgeo.2018.02.032

Ye, Q., Mei, L., Shi, H., Camanni, G., Shu, Y., & Wu, J., et al. (2018). The late cretaceous tectonic evolution of the South China Sea area: an overview, and new perspectives from 3D seismic reflection data. *Earth-Science Reviews, 187*, 186-204. https://doi.org/10.1016/j.earscirev.2018.09.013

Zelt, C. A., & Barton, P. J. (1998). Three-dimensional seismic refraction tomography: a comparison of two methods applied to data from the faeroe basin. *Journal of Geophysical Research: Solid Earth, 103(B4)*, 7187-7210. https://doi.org/10.1029/97JB03536

Zelt, C. A., & Smith, R. B. (1992). Seismic travel-time inversion for 2-D crustal velocity structure. *Geophysical Journal International, 108(1)*, 16-34. https://doi.org/10.1111/j.1365-246X.1992.tb00836.x

Zelt, C., A., & Forsyth, D. A. (1994). Modeling wide-angle seismic data for crustal structure: southeastern Grenville province. *Journal of Geophysical Research: Solid Earth, 99(B6)*, 11687-11704. https://doi.org/10.1029/93JB02764

Zhang, C., Manatschal, G., Pang, X., Sun, Z., & Zheng, J., et al. (2020). Discovery of mega-sheath folds flooring the Liwan subbasin (South China Sea): implications for the rheology

1026   of hyperextended crust. *Geochemistry, Geophysics, Geosystems, 21(7)*, e2020GC009023.
1027   https://doi.org/10.1029/2020GC009023

1028 Zhang, C., Sun, Z., Manatschal, G., Pang, X., & Zhao, M. (2021). Ocean-continent transition
1029   architecture and breakup mechanism at the mid-northern South China Sea. *Earth-Science*
1030   *Reviews, 217*, 103620. https://doi.org/10.1016/j.earscirev.2021.103620

1031 Zhang, J., Zhao M., & Qiu, X. (2022). Ocean Bottom Seismometer data of a three-dimensional
1032   seismic survey in the northern South China Sea distal margin [Dataset]. Science Data Bank.
1033   https://www.scidb.cn/anonymous/ckVyTVpm

1034 Zhao, F., Alves, T. M., Xia, S., Li, W., & Fan, C. (2019). Along-strike segmentation of the South
1035   China Sea margin imposed by inherited pre-rift basement structures. *Earth and Planetary*
1036   *Science Letters, 530*, 115862. https://doi.org/10.1016/j.epsl.2019.115862

1037 Zhao, M., Qiu, X., Li, J., Sauter, D., Ruan, A., & Chen, J., et al. (2013). Three-dimensional
1038   seismic structure of the Dragon Flag oceanic core complex at the ultraslow spreading
1039   Southwest Indian Ridge (49°39′ E). *Geochemistry Geophysics Geosystems, 14(10)*, 4544-
1040   4563. https://doi.org/10.1002/ggge.20264

1041 Zhou, D., Wang, W., Wang, J., Pang, X., Cai D. & Sun Z. (2006). Mesozoic subduction-
1042   accretion zone in northeastern South China Sea inferred from geophysical interpretations.
1043   *Science in China Series D Earth Sciences, 49(5)*, 471-482. https://doi.org/10.1007/s11430-
1044   006-0471-9

New Insights into the Rift-to-Drift Process of the Northern South China Sea Constrained by a Three-dimensional OBS Seismic Structure

Jiazheng Zhang[1*], Minghui Zhao[1,6*], Weiwei Ding[2], César R. Ranero[3,4], Valenti Sallares[3], Jinwei Gao[5], Cuimei Zhang[1], Xuelin Qiu[1,6]

[1]Key Laboratory of Ocean and Marginal Sea Geology, South China Sea Institute of Oceanology, Chinese Academy of Sciences, Guangzhou 510301, China.
[2]Key Laboratory of Submarine Geosciences, State Oceanic Administration, Second Institute of Oceanography, Ministry of Natural Resources, Hangzhou 310012, China.
[3]Barcelona Center for Subsurface Imaging, Instituto de Ciéncies del Mar (ICM-CSIC), Barcelona, Spain.
[4]ICREA, Barcelona, Spain
[5]Laboratory of Marine Geophysics and Deep-Sea Georesource, Institute of Deep-sea Science and Engineering, Chinese Academy of Sciences, Sanya 572000, China.
[6]University of Chinese Academy of Sciences, Beijing 100049, China.

 Corresponding author: Jiazheng Zhang (jzzhang@scsio.ac.cn) ; Minghui Zhao (mhzhao@scsio.ac.cn)

Contents of this file

 Figures S1 to S18.

Introduction

  The supplementary figures (Figures S1-S4) display the 3D models of velocity uncertainty and raytracing count, which are used to show the confidence of final 3D Vp model. The supplementary figures (Figures S5-S12) display a set of checkerboard tests mainly showing three different squared cell sizes (4, 10, 20 km), which are used to evaluate the resolution of the tomographic Vp model. The supplementary figures (Figures S13-S16) display the 3D models of velocity gradient and velocity perturbation, which are used to help analyze the final 3D Vp model. The supplementary Figure S17 displays the comparison between 2D and 3D Vp models along L2, which is used to indicate that it is reasonable to take 7.5 km/s velocity contour in our 3D Vp model as the Moho. Figure S18 displays the relationship among HVLC thickness, melt thickness, crustal stretching factor, rifting duration, potential temperature of asthenosphere as well as initial continental lithospheric thickness.
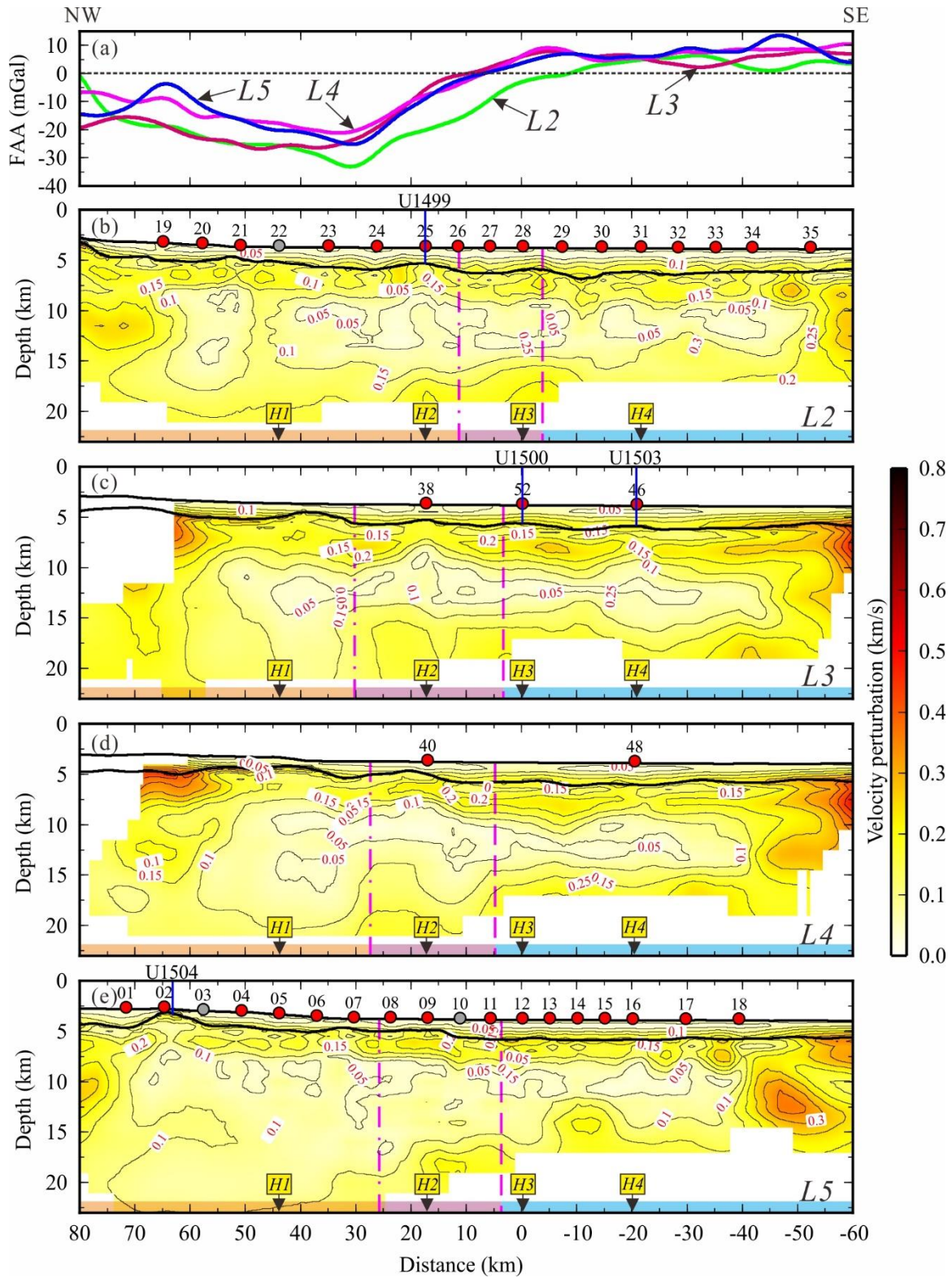
Figure S1. Vertical slices crosscutting the 3D Vp uncertainty model and free-air gravity anomaly. The other symbols are same as Figure 5.
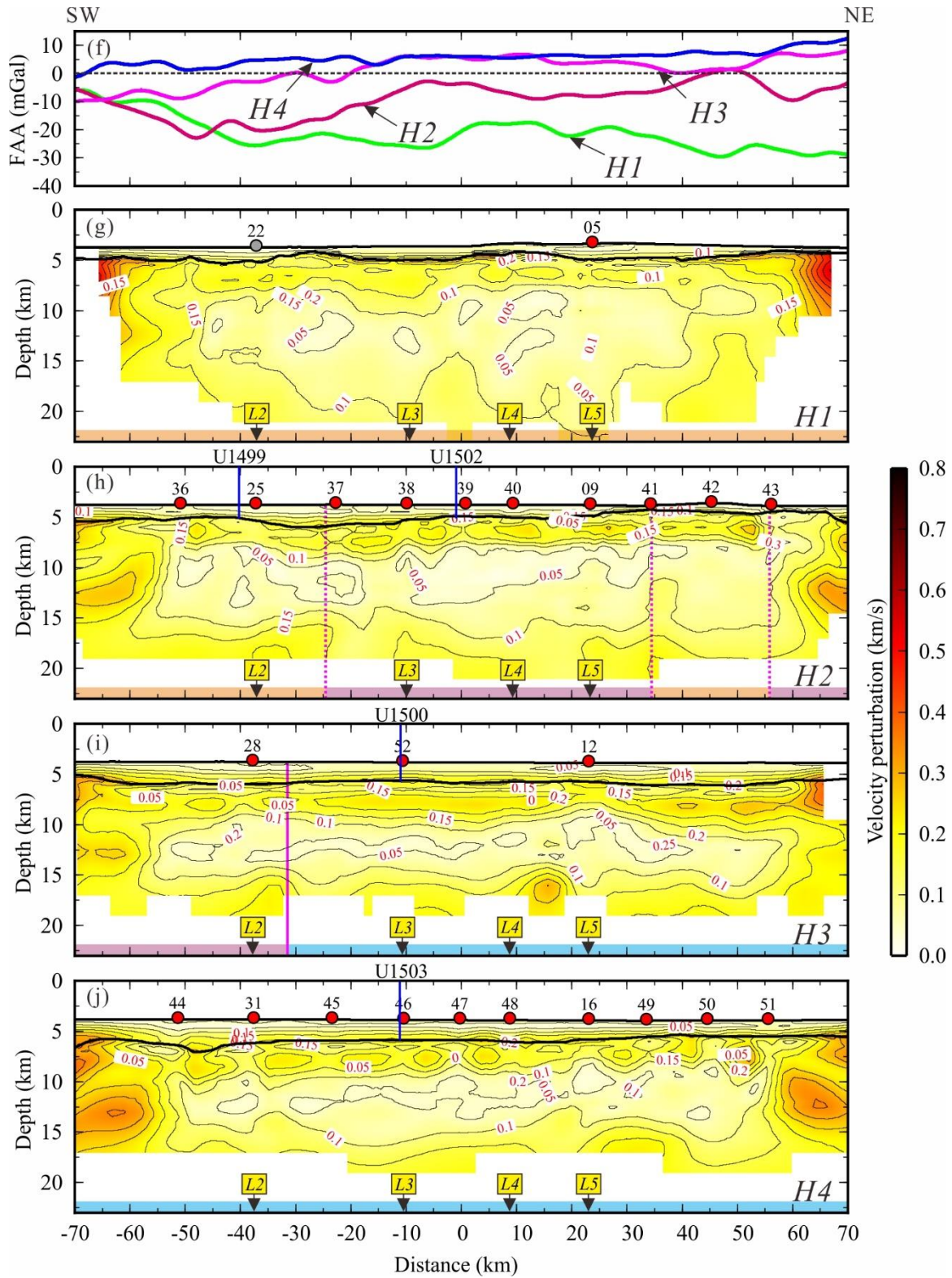
Figure S1 (Continuous).
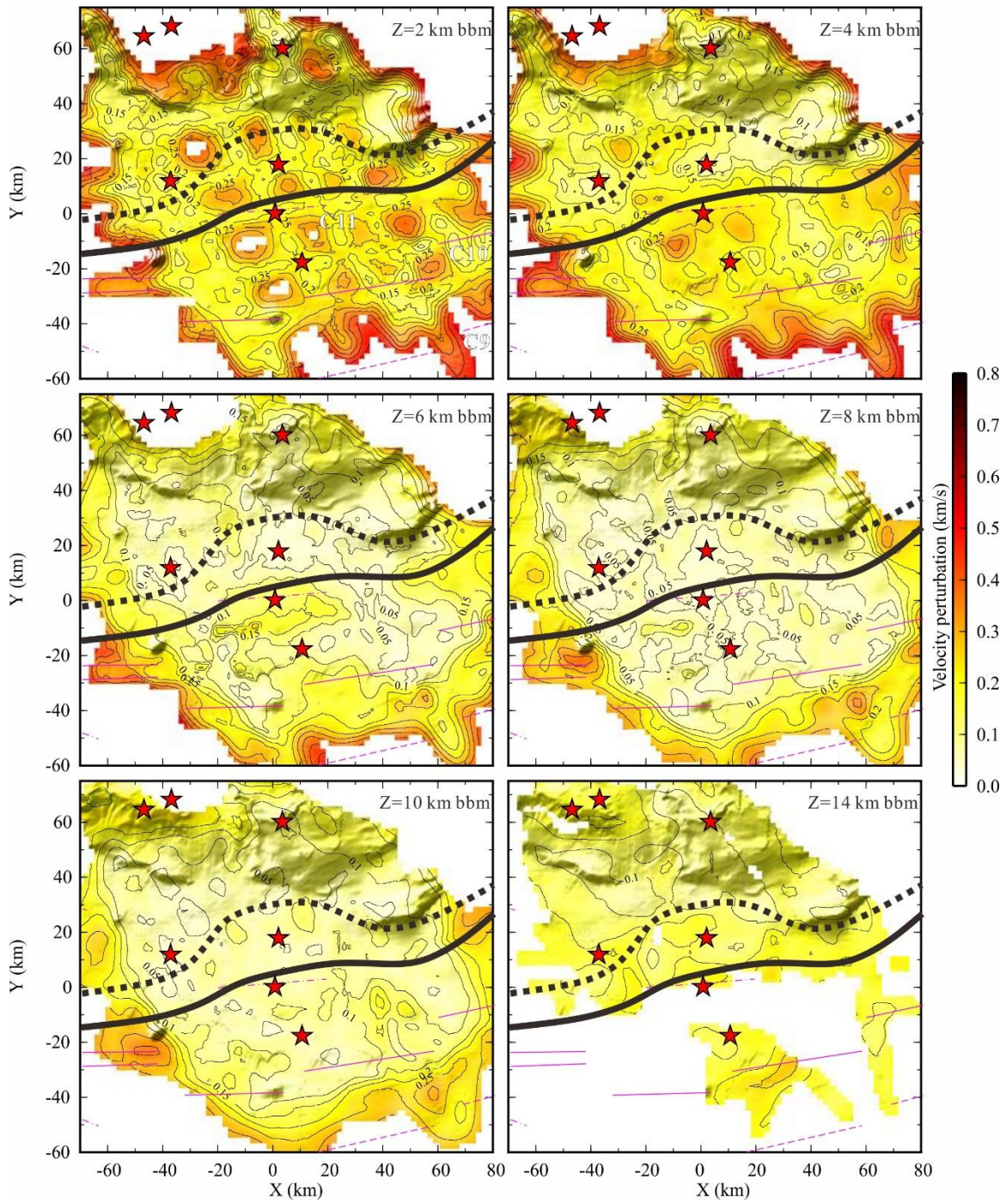
Figure S2. Horizontal slices of the 3D Vp uncertainty model at different depths below TOB (bbm). The other symbols are same as Figure 6.
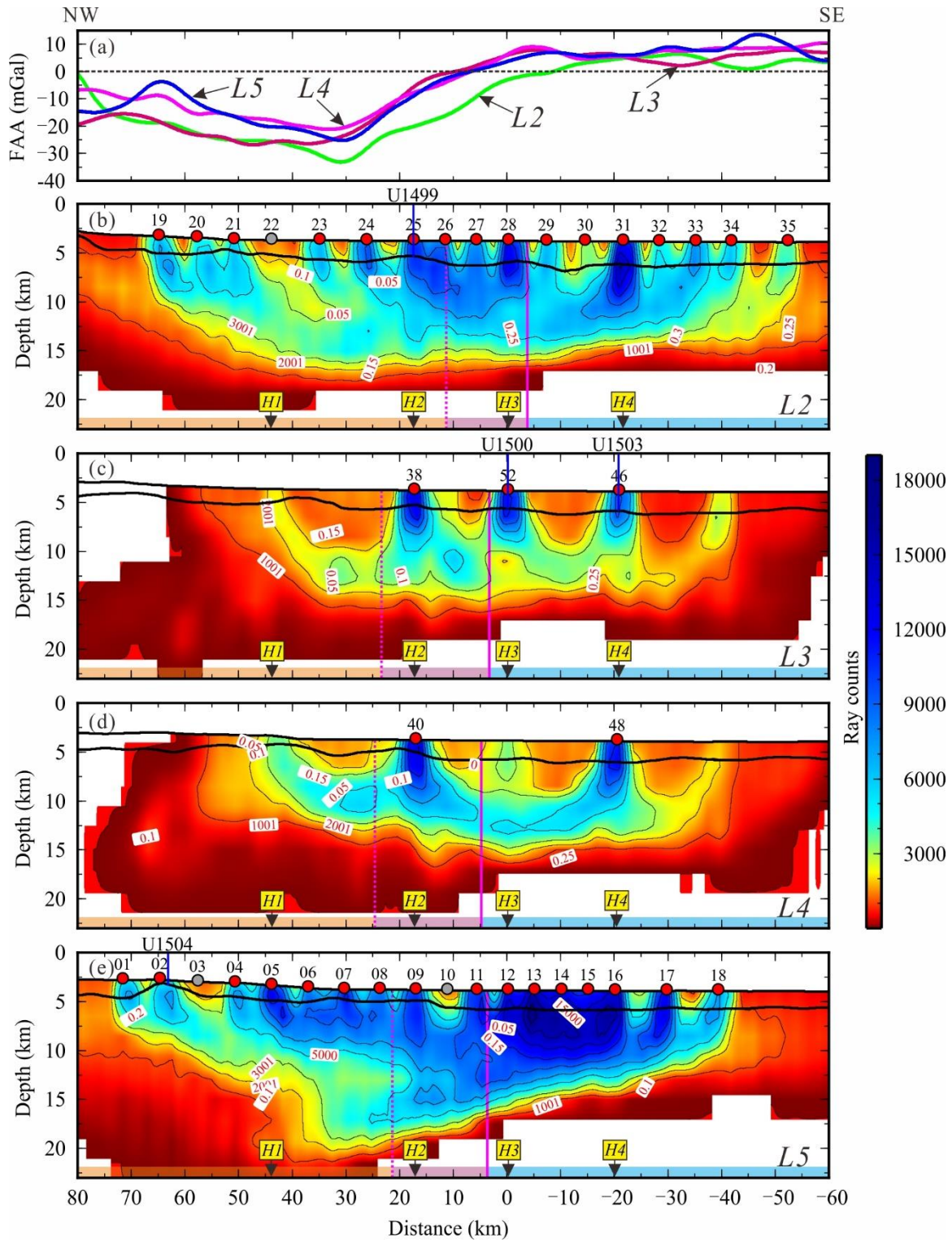
Figure S3. Vertical slices crosscutting the 3D raytracing count model and free-air gravity anomaly. The other symbols are same as Figure 5.
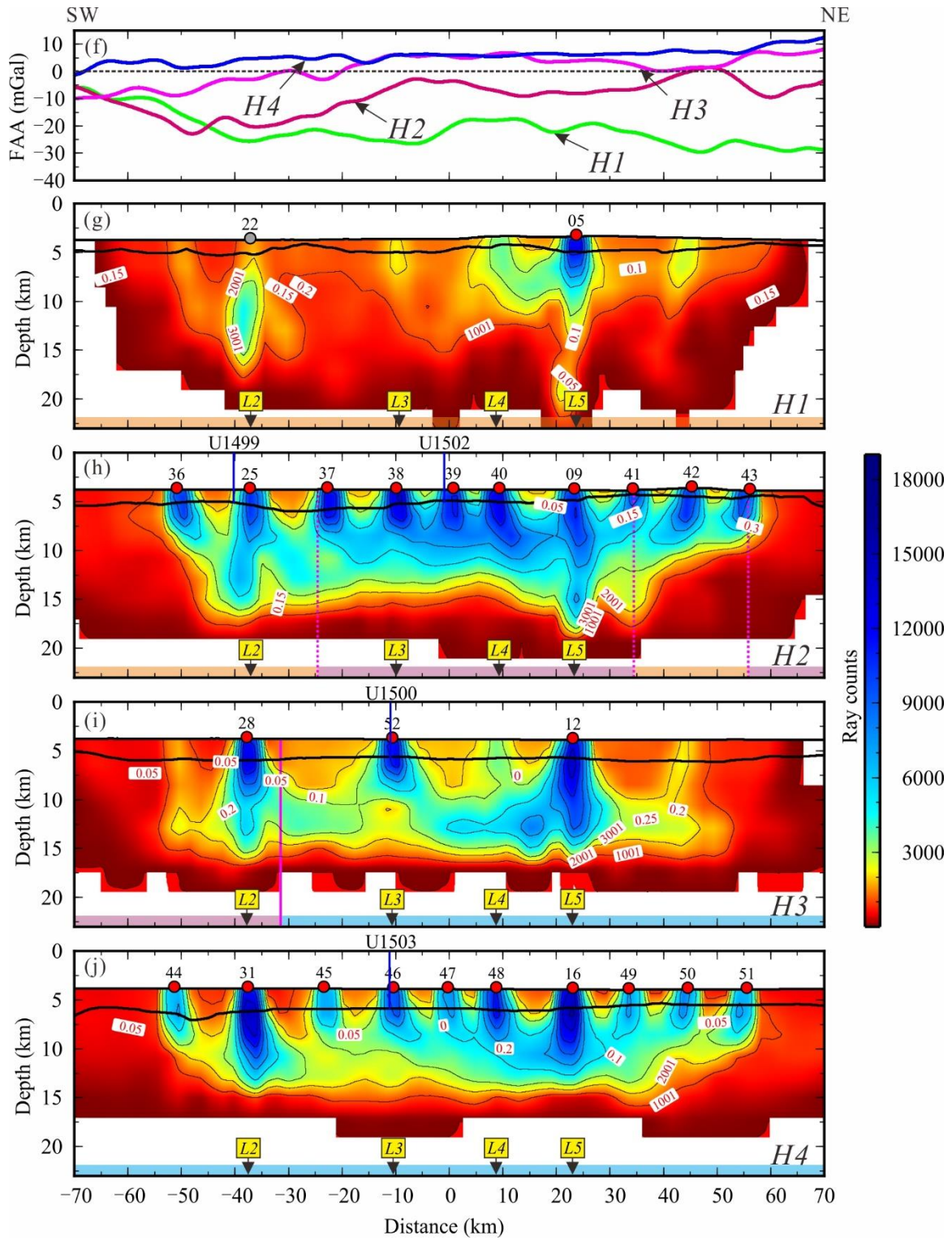
Figure S3 (Continuous).
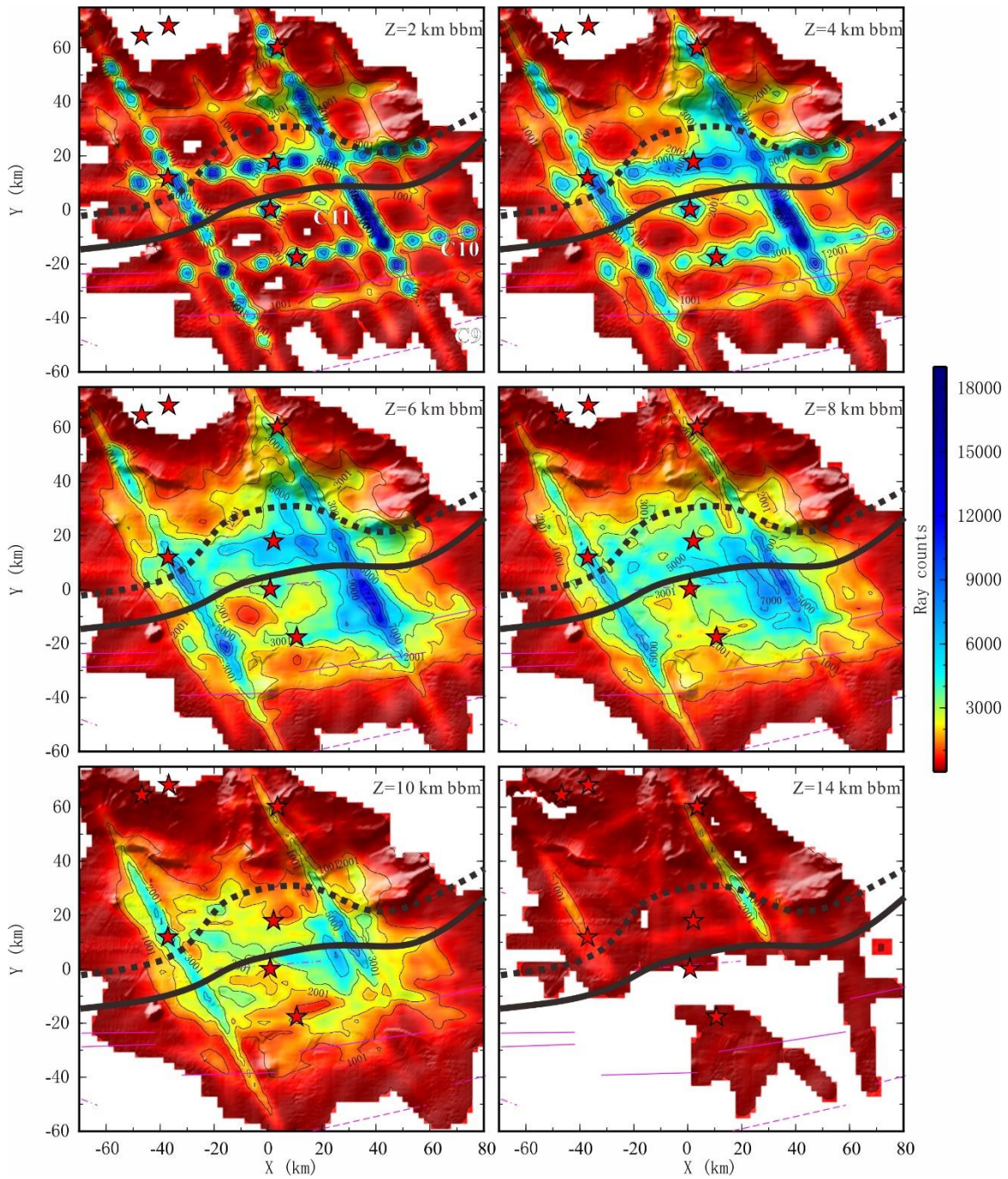
Figure S4. Horizontal slices of the 3D raytracing count model at different depths below TOB (bbm). The other symbols are same as Figure 6.
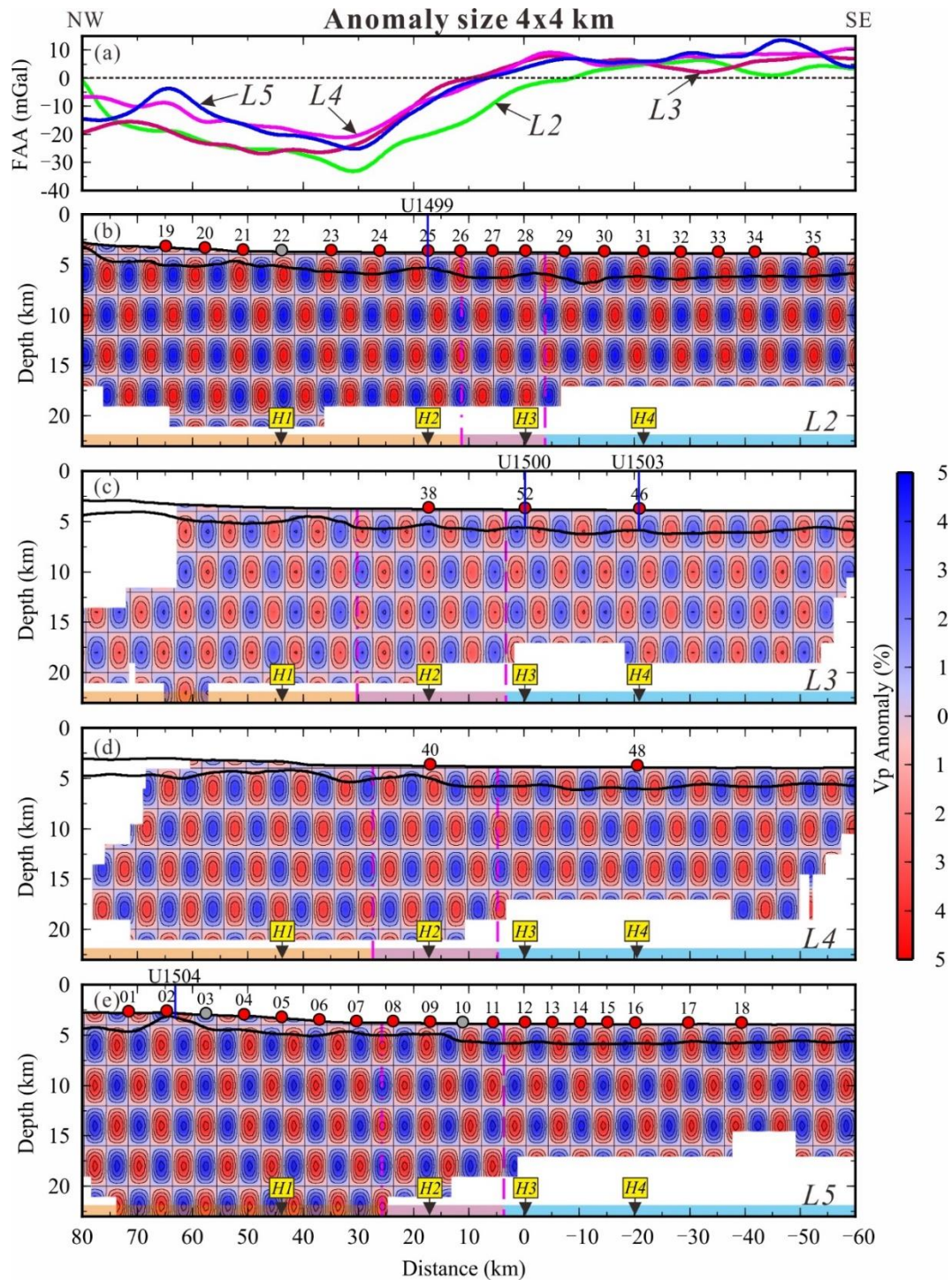
Figure S5. Vertical slices crosscutting the 3D models with true checkerboard pattern of the 4x4 km (a-e), 10x10 km (a'-e') and 20x20 km (a''-e'') anomaly size. The other symbols are same as Figure 5.
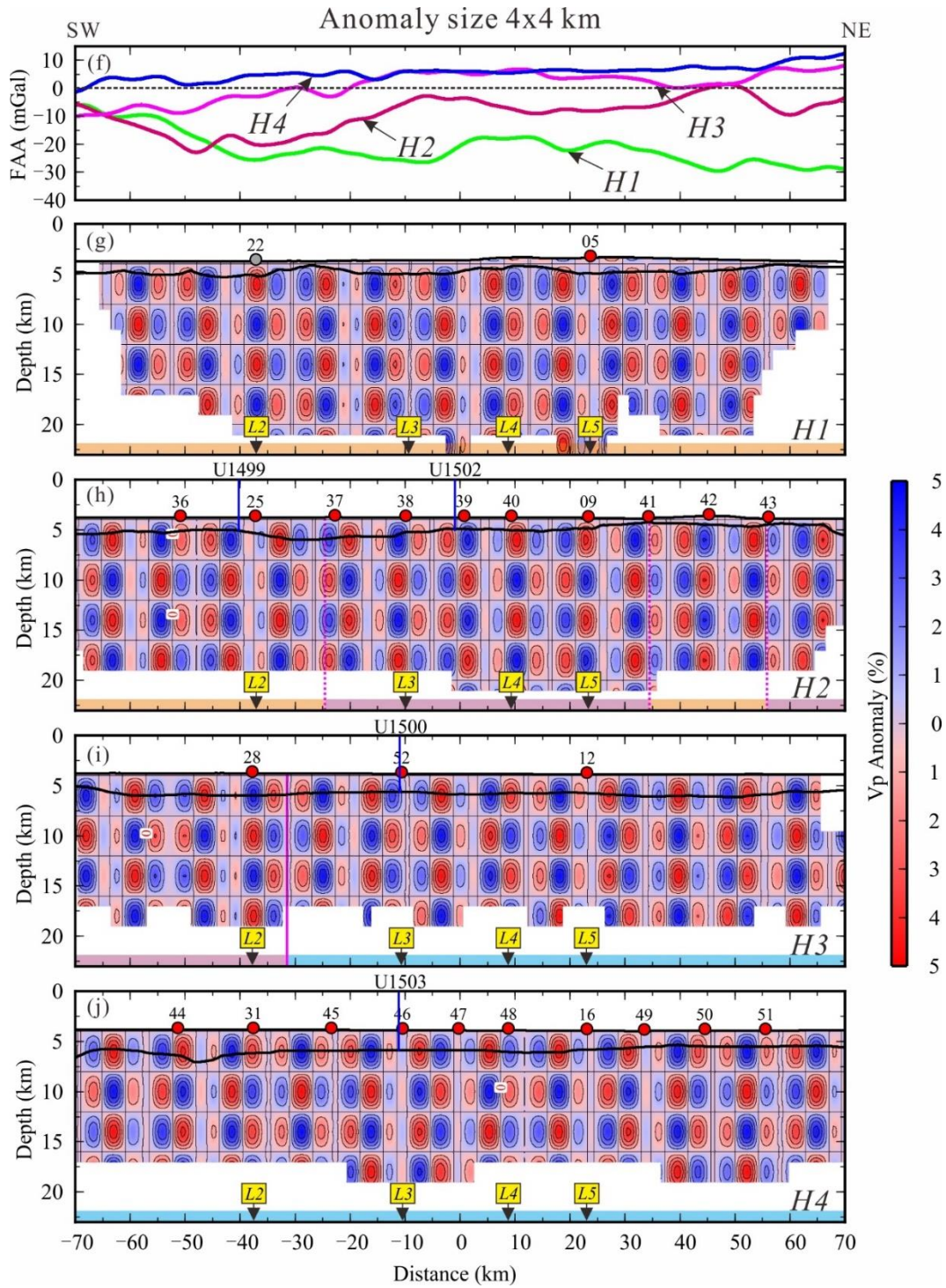
Figure S5 (Continuous).
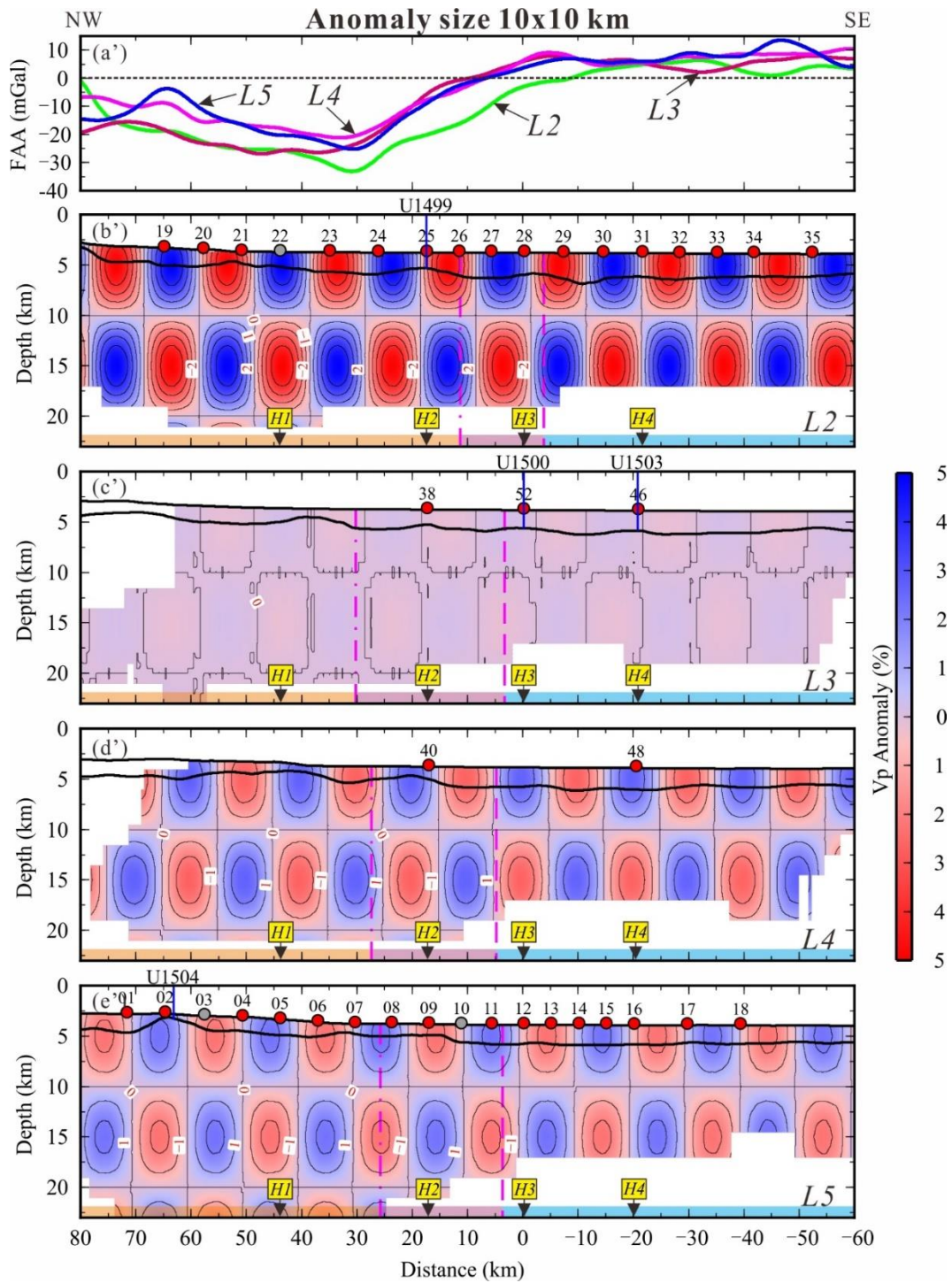
Figure S5 (Continuous).
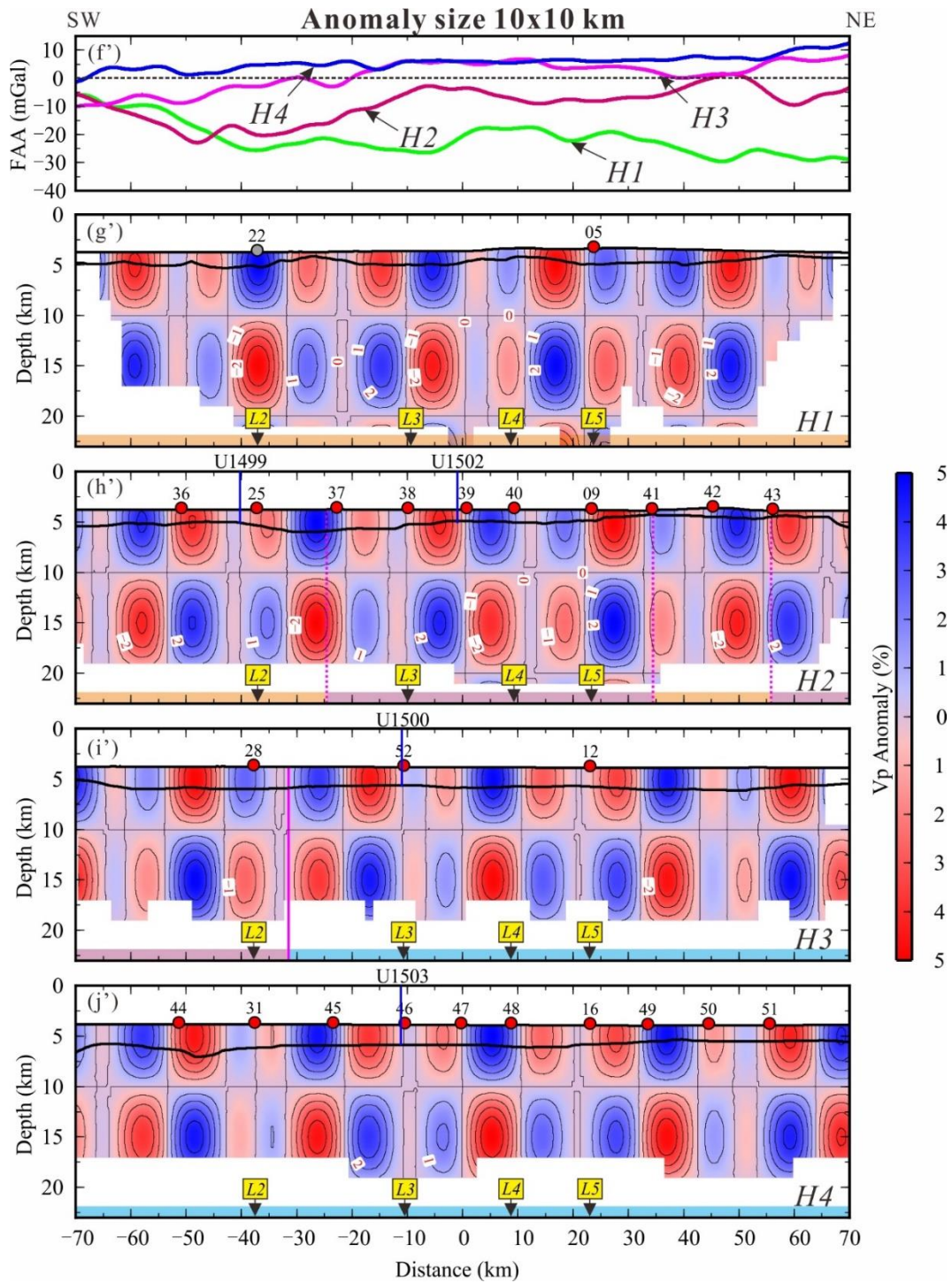
Figure S5 (Continuous).
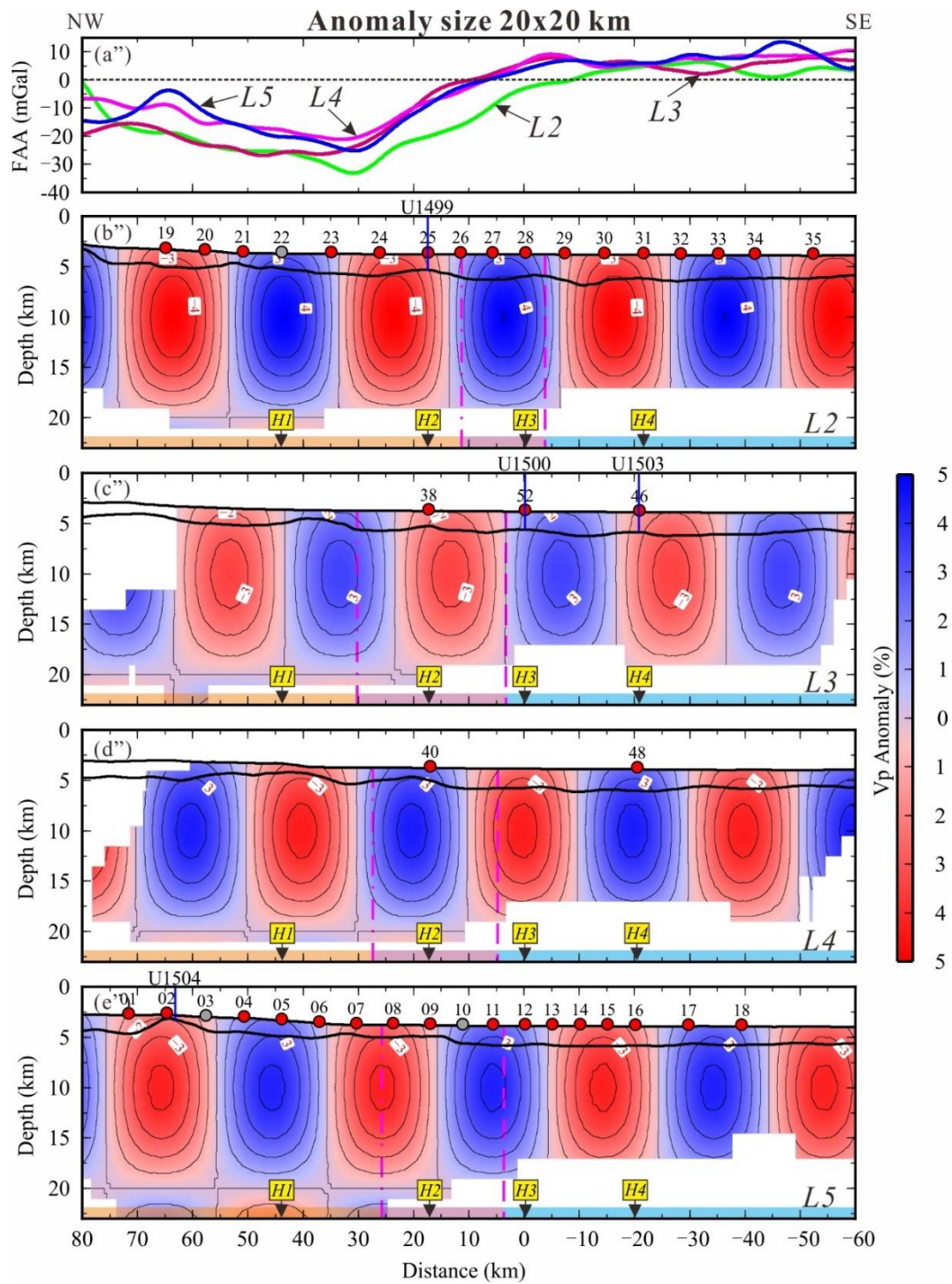
Figure S5 (Continuous).
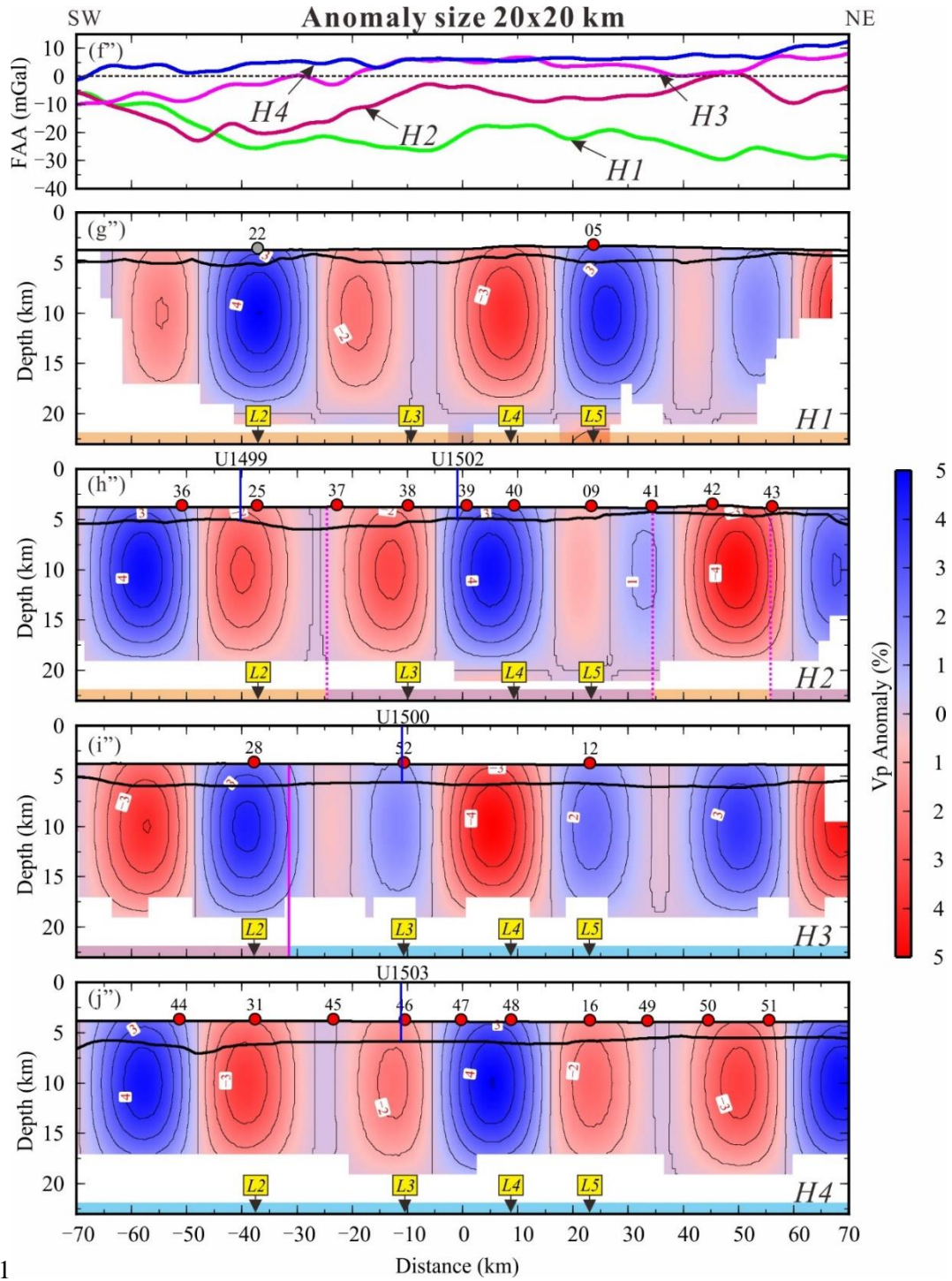
Figure S5 (Continuous).
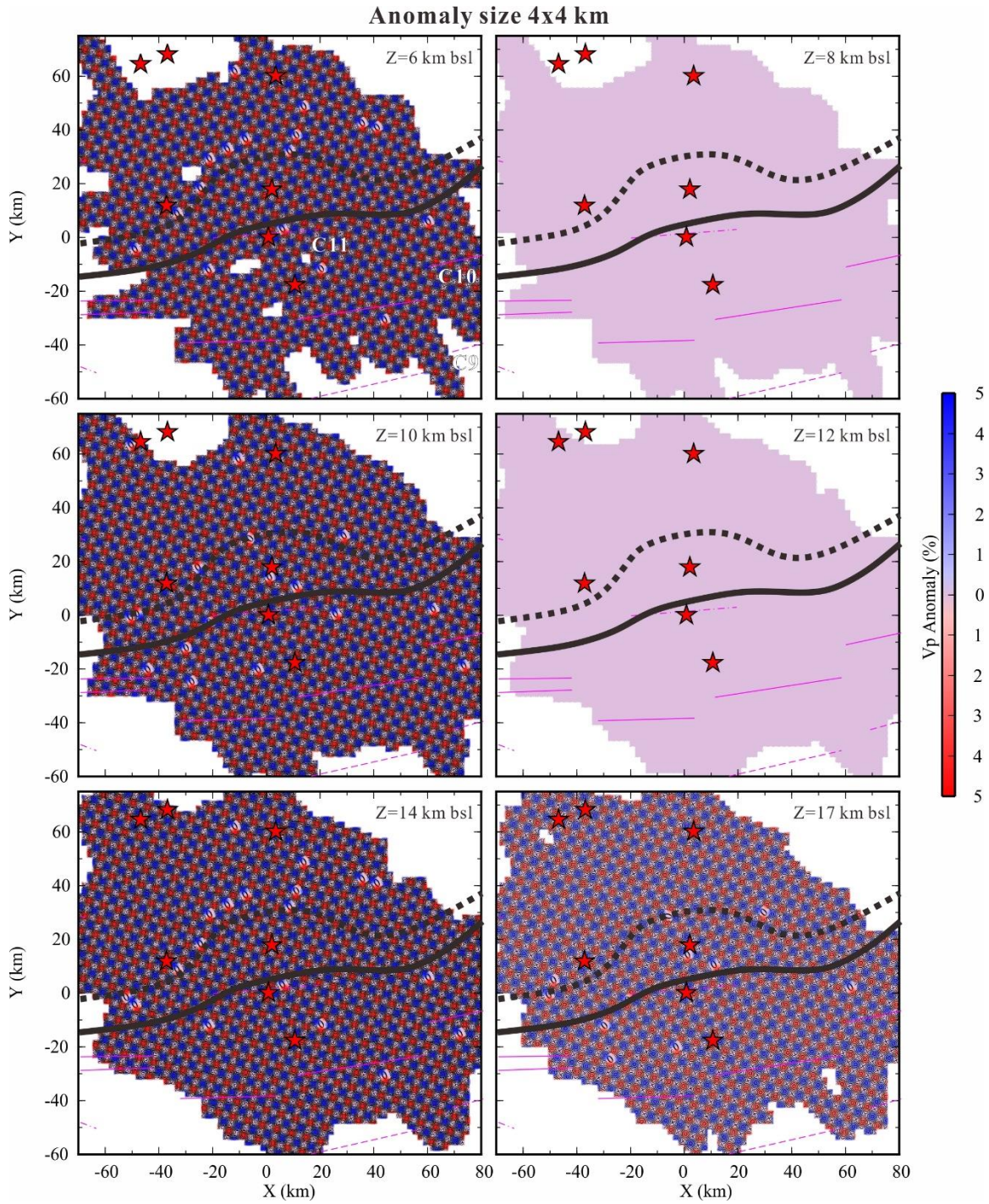
Figure S6. Horizontal slices of the 3D models with true checkerboard pattern of the 4x4 km, 10x10 km and 20x20 km anomaly size at different depths below sea level (bsl). The other symbols are same as Figure 6.

Anomaly size 10x10 km
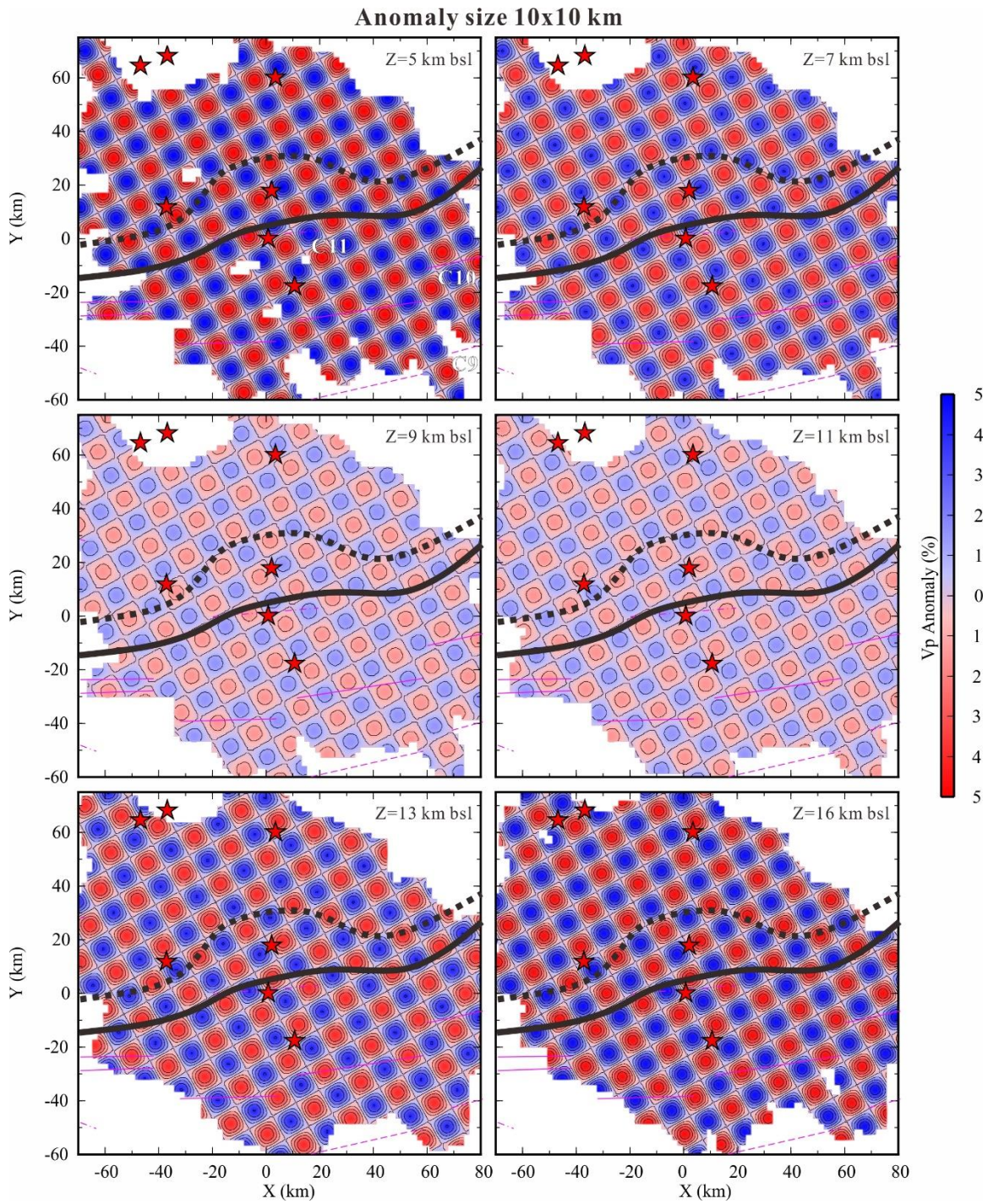
Figure S6 (Continuous).
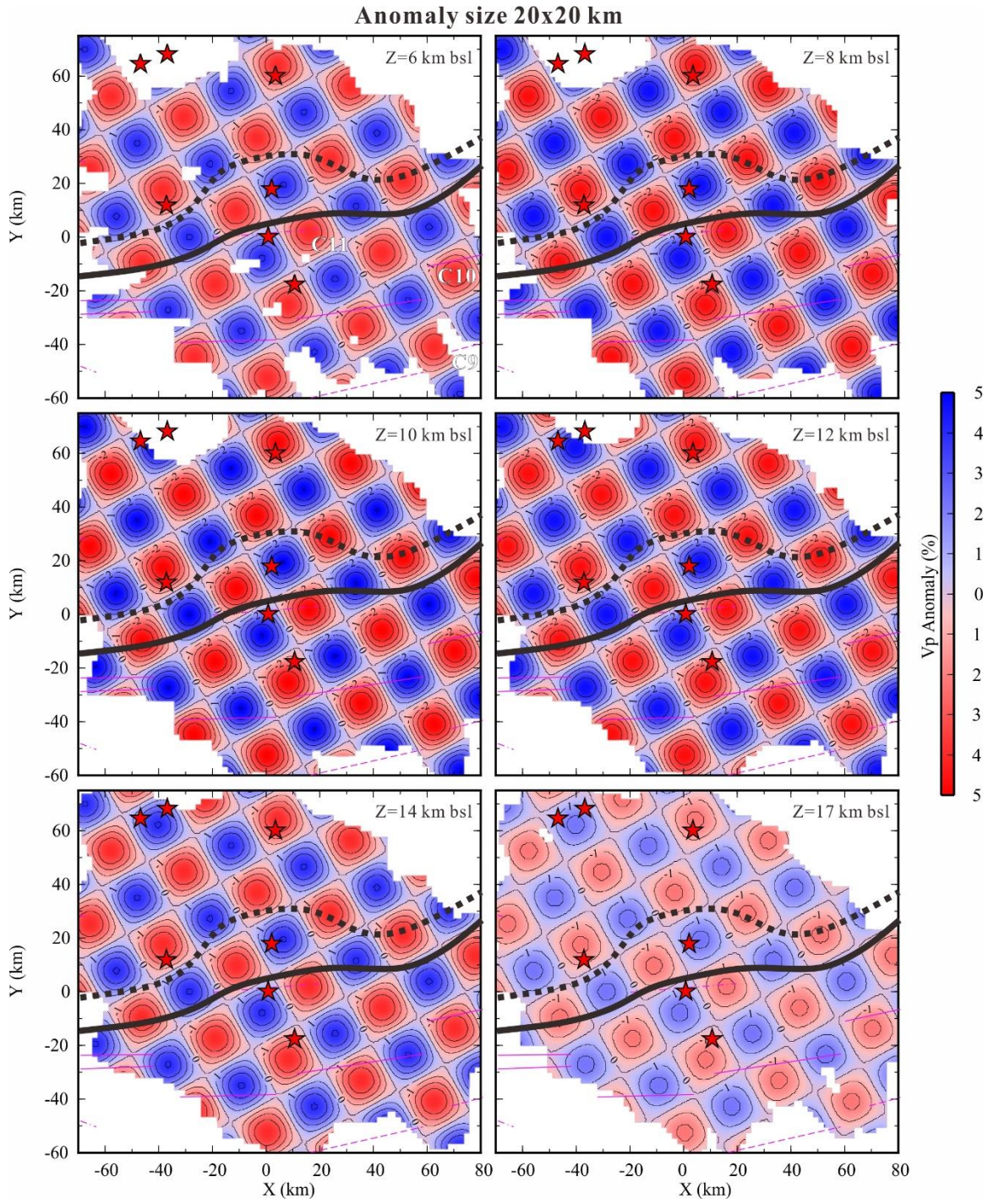
Figure S6 (Continuous).
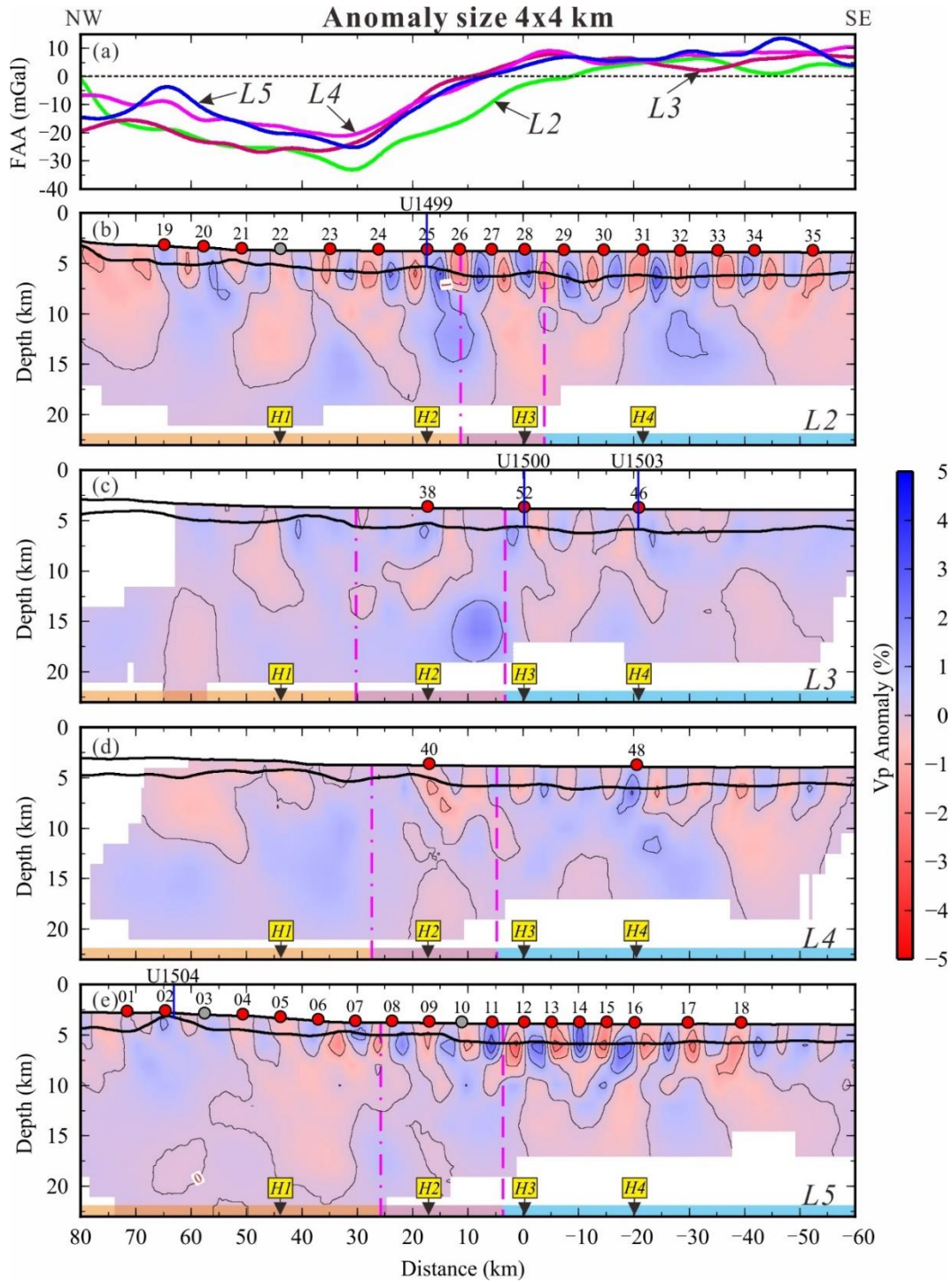
Figure S7. Vertical slices crosscutting the 3D models with retrieved checkerboard pattern of the 4x4 km (a-e), 10x10 km (a'-e') and 20x20 km (a''-e'') anomaly size. The other symbols are same as Figure 5.
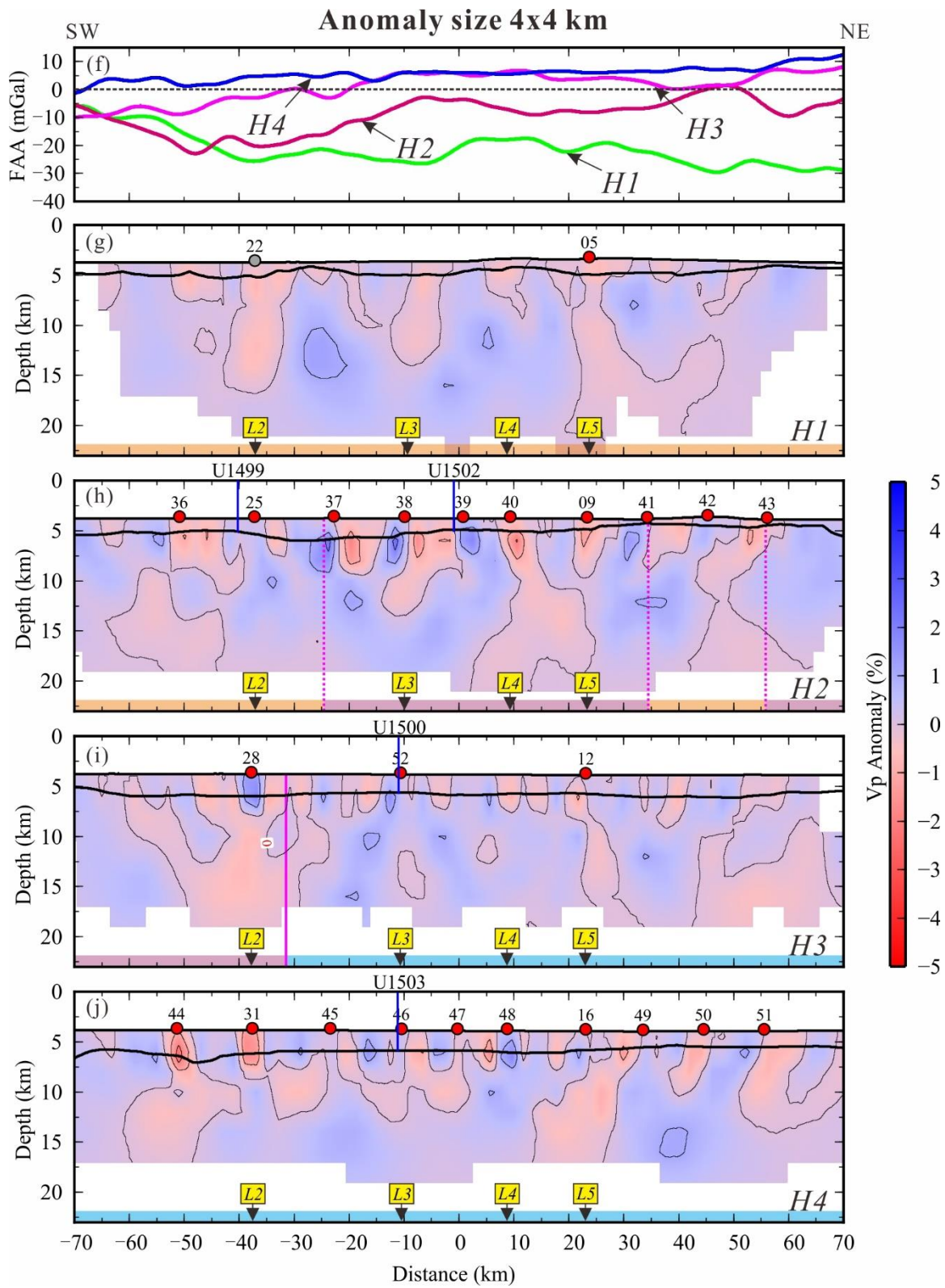
Figure S7 (Continuous).
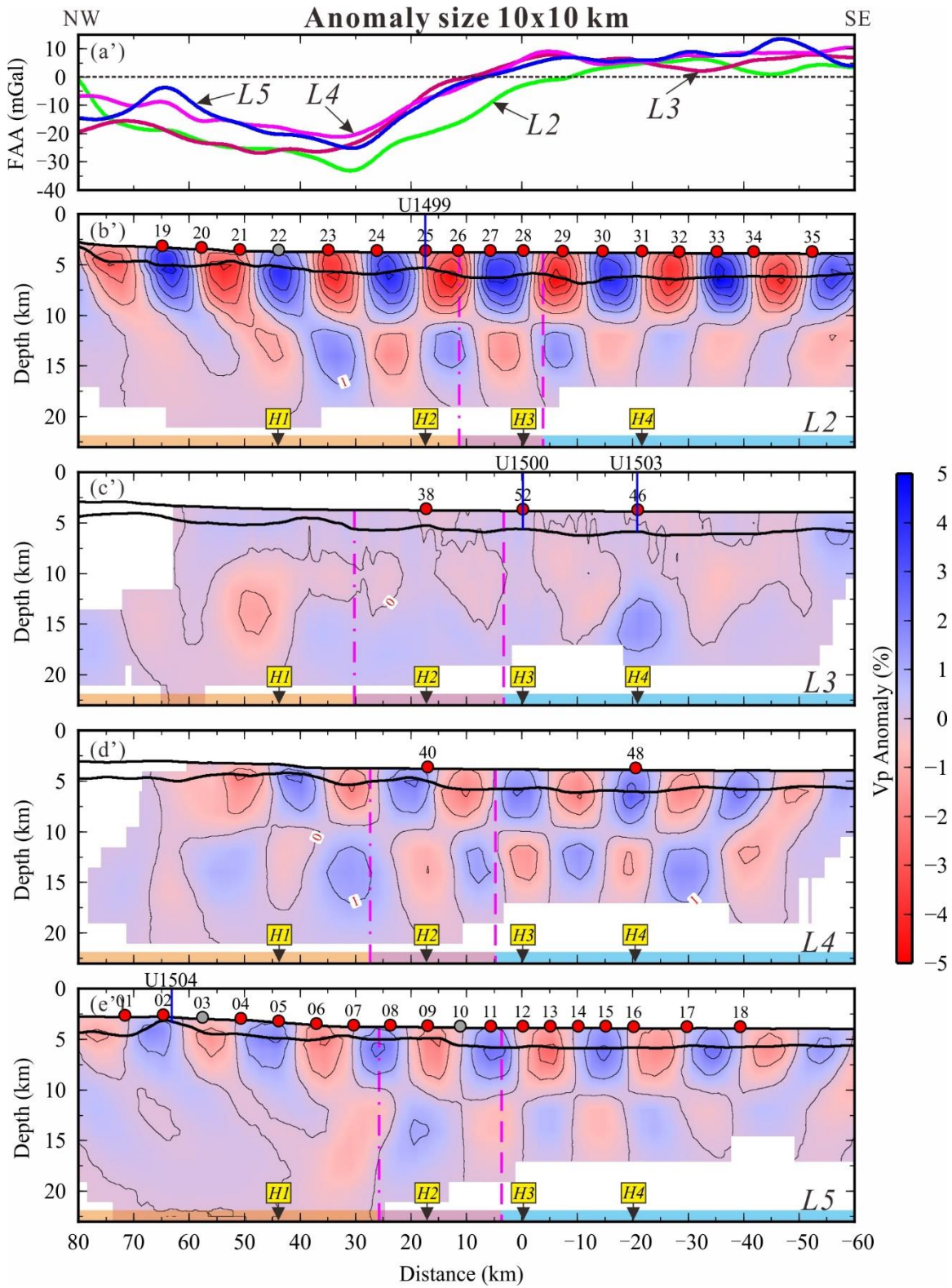
Figure S7 (Continuous).
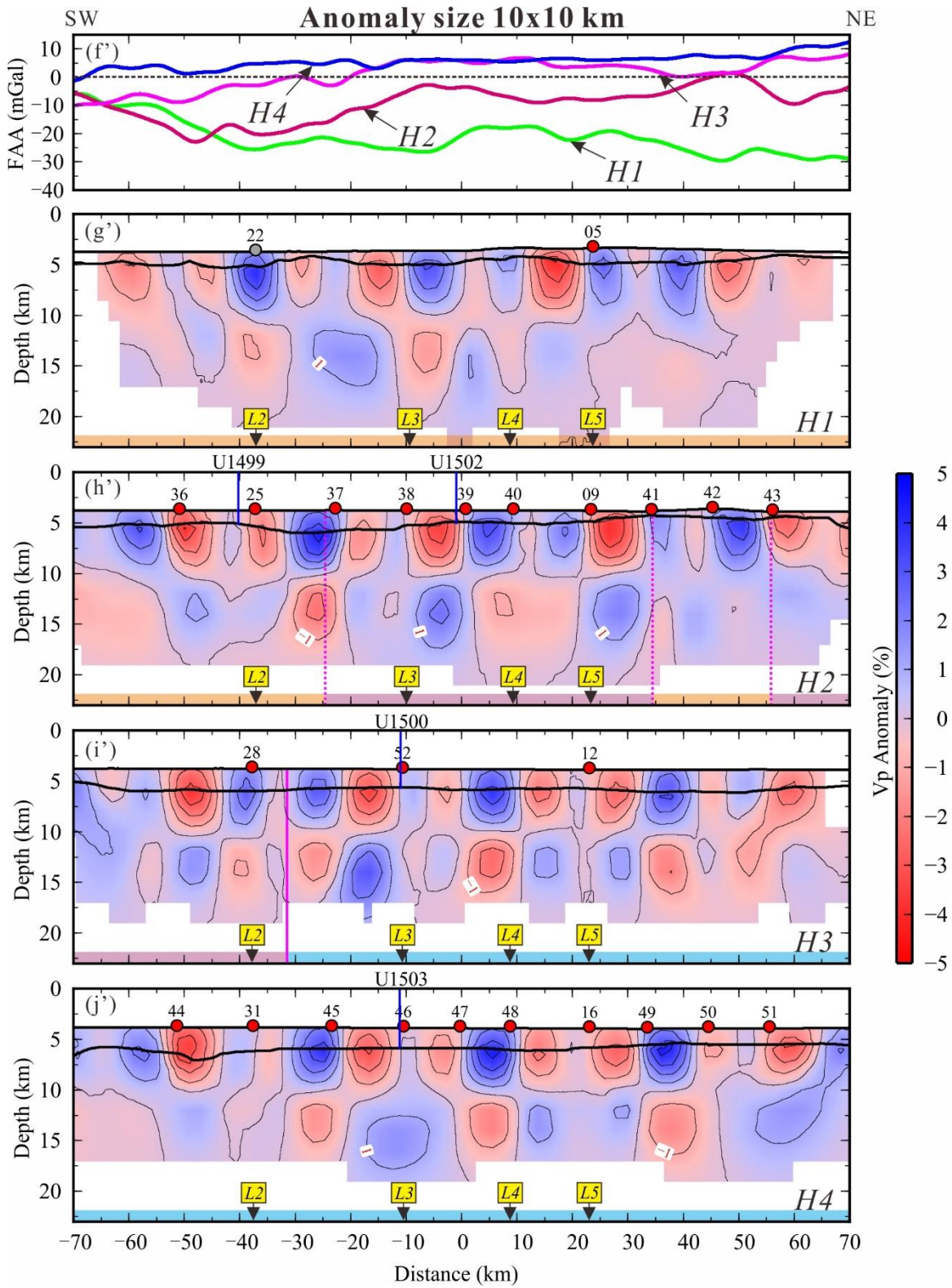
Figure S7 (Continuous).
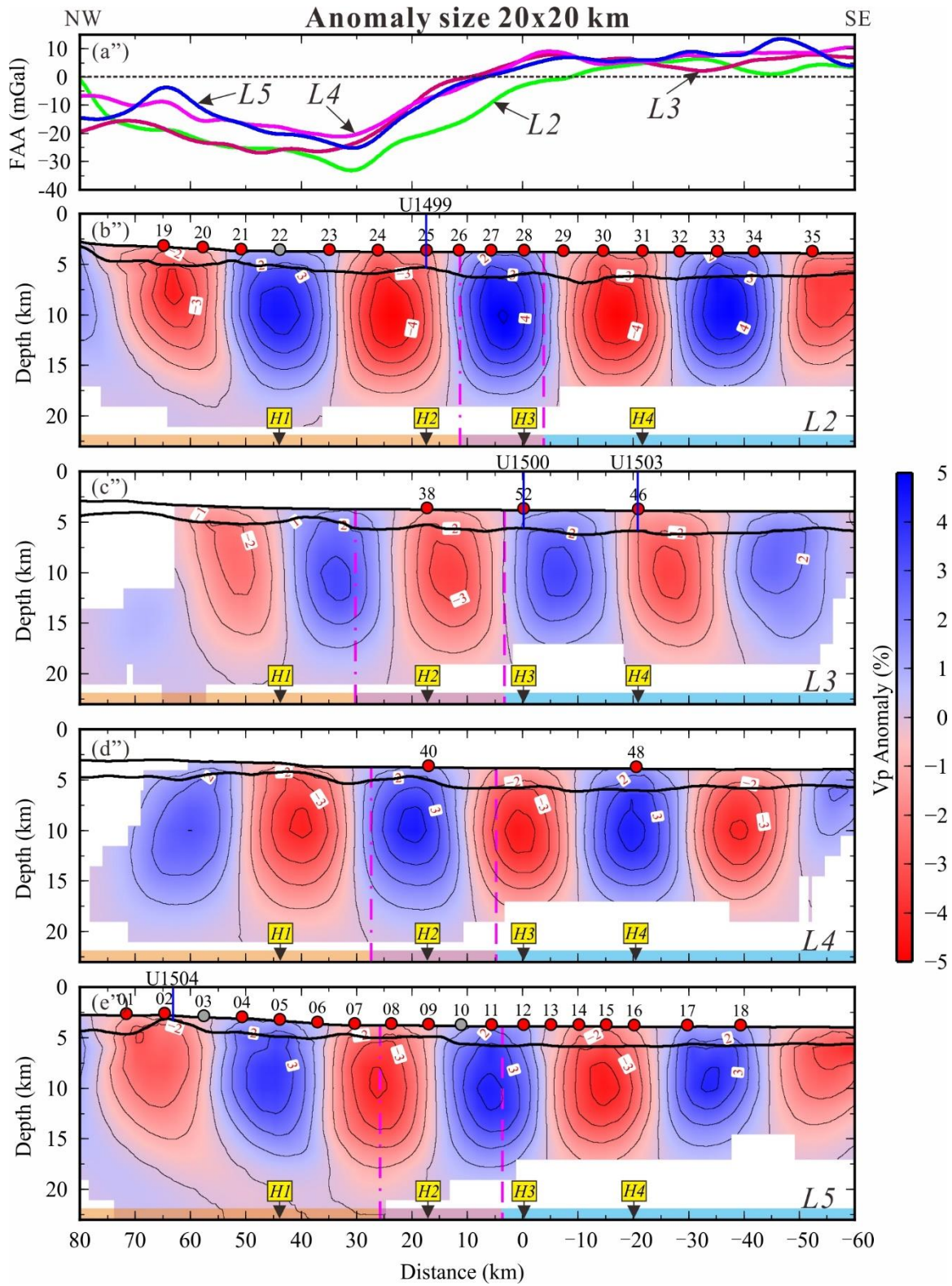
Figure S7 (Continuous).
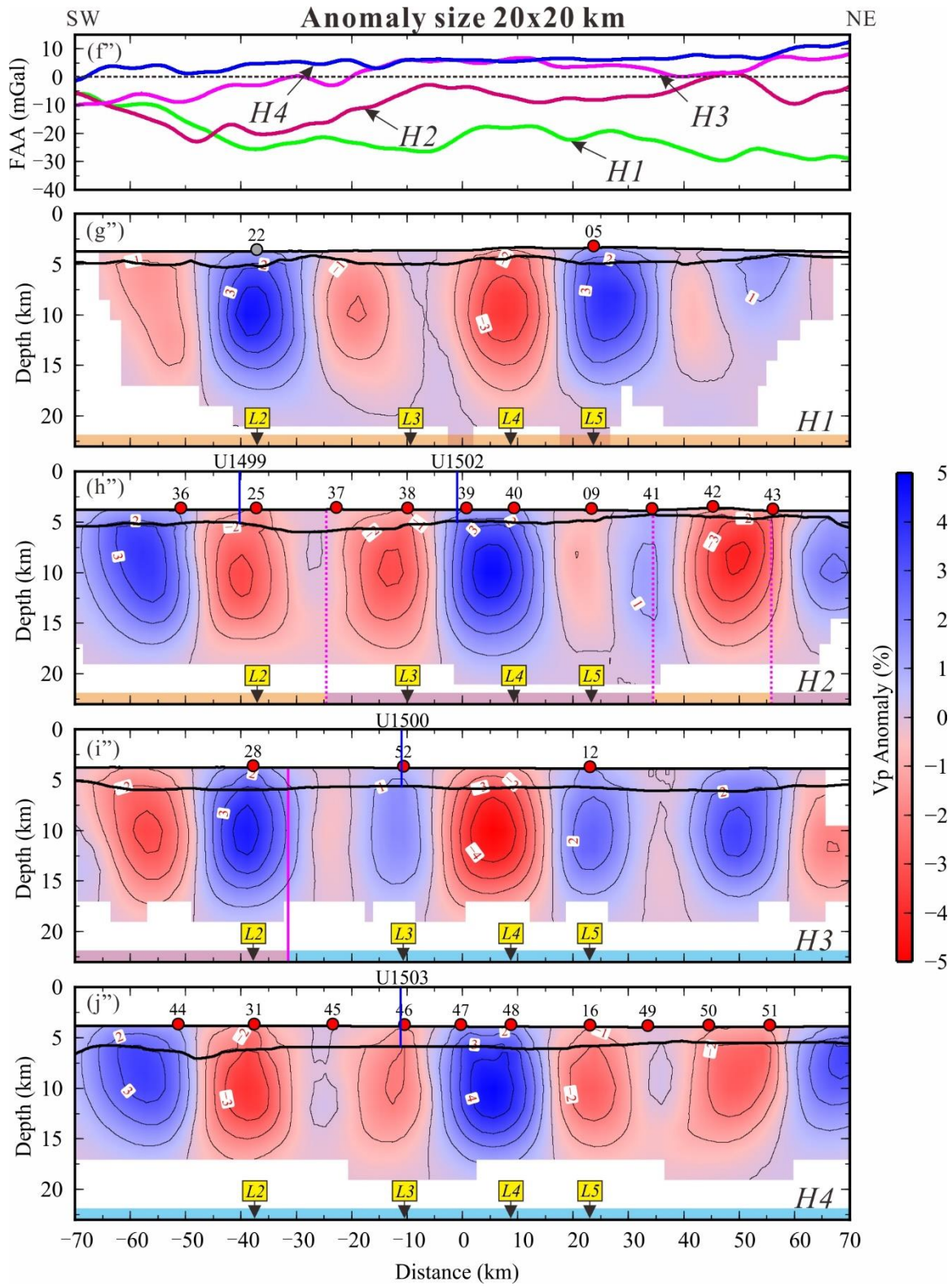
Figure S7 (Continuous).
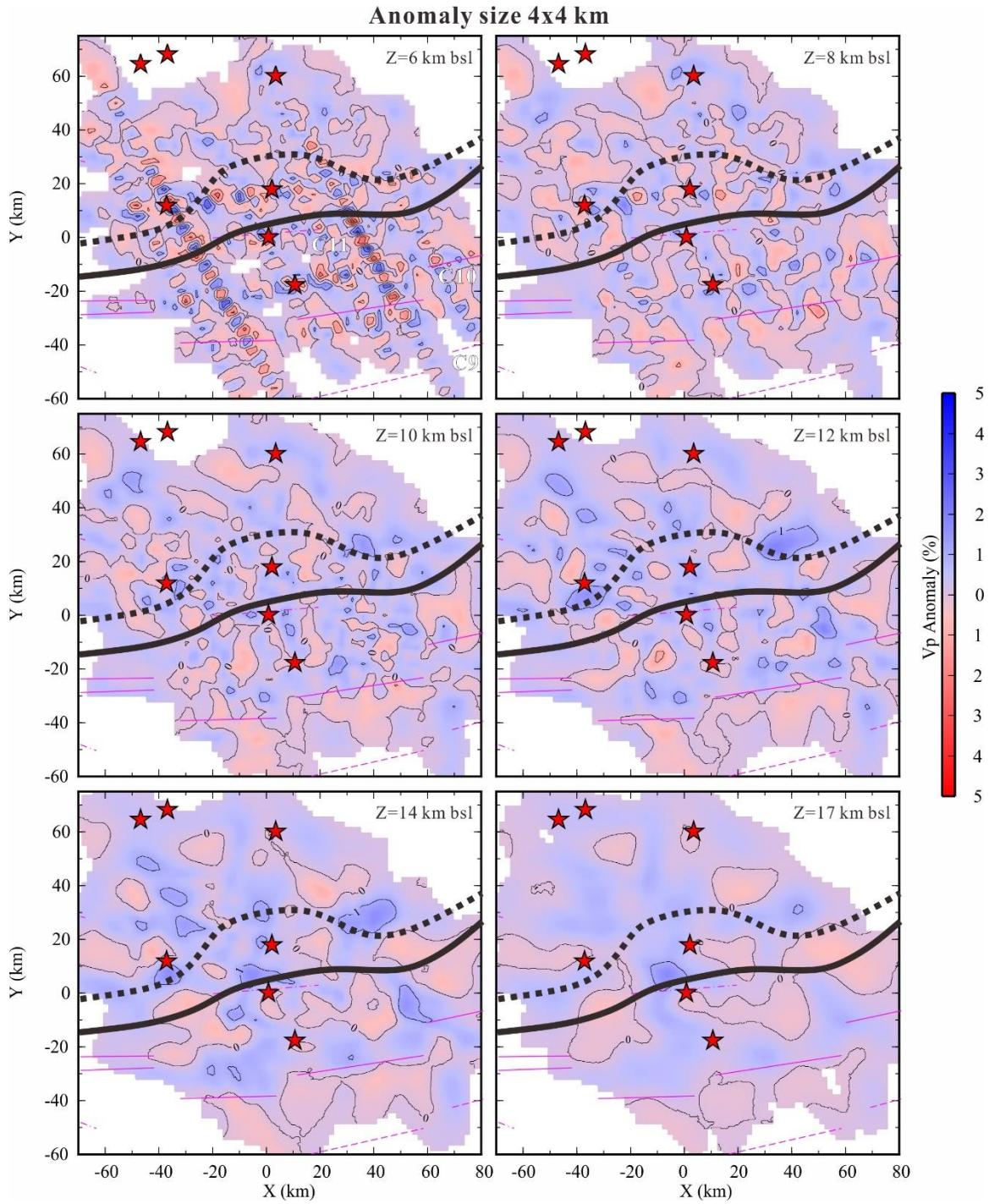
Figure S8. Horizontal slices of the 3D models with retrieved checkerboard pattern of the 4x4 km, 10x10 km and 20x20 km anomaly size at different depths below sea level (bsl). The other symbols are same as Figure 6.
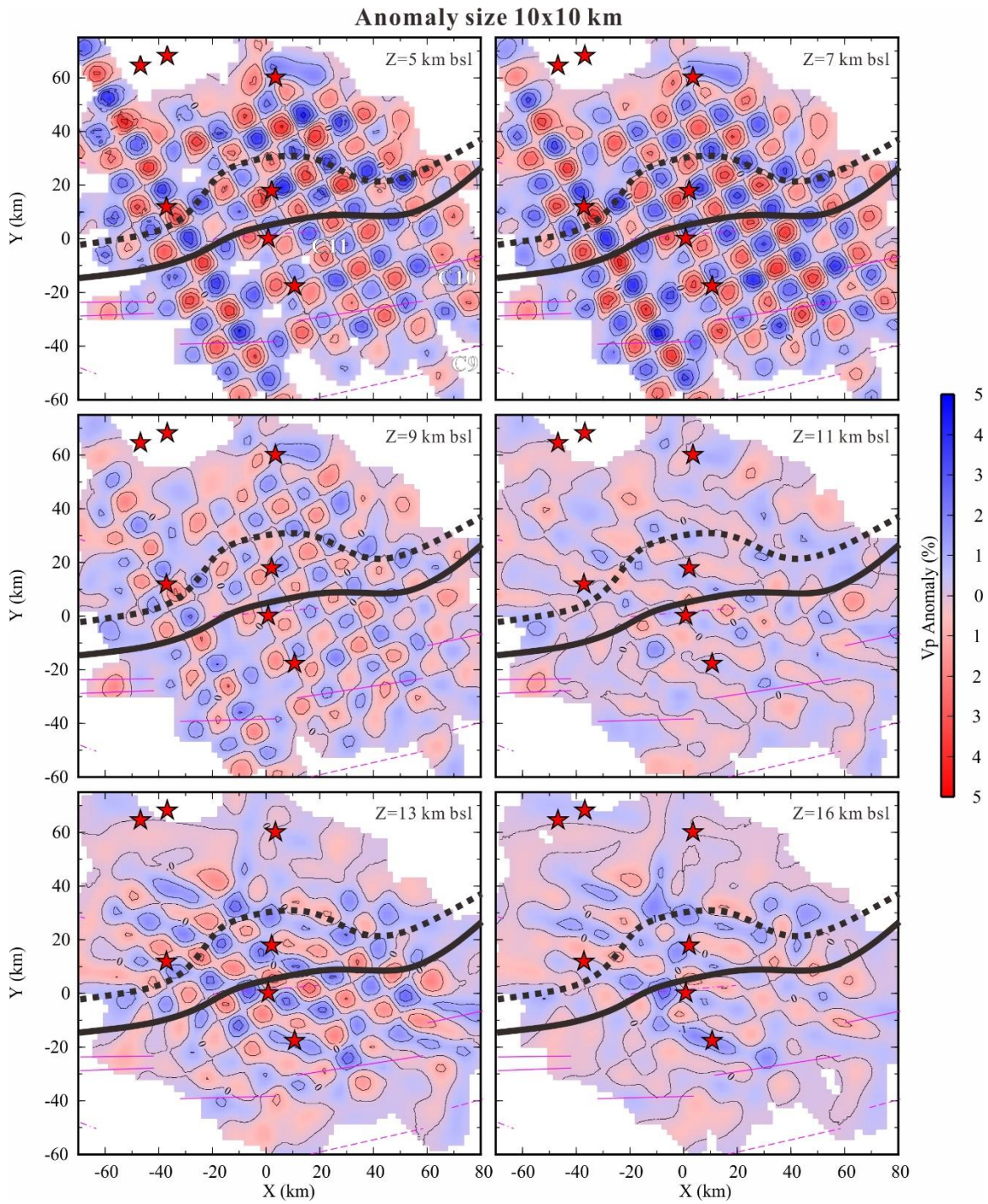
Figure S8 (Continuous).
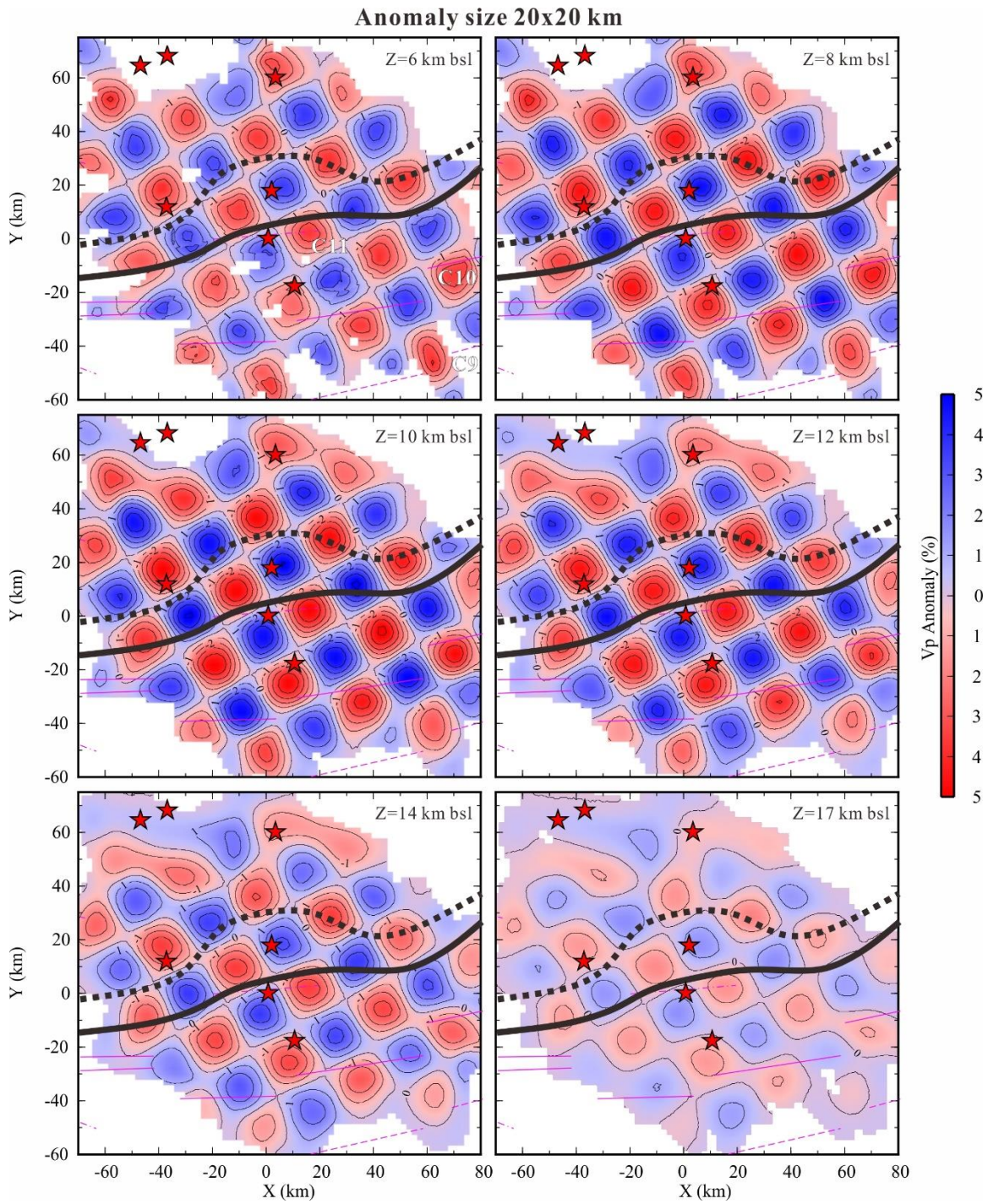
Figure S8 (Continuous).
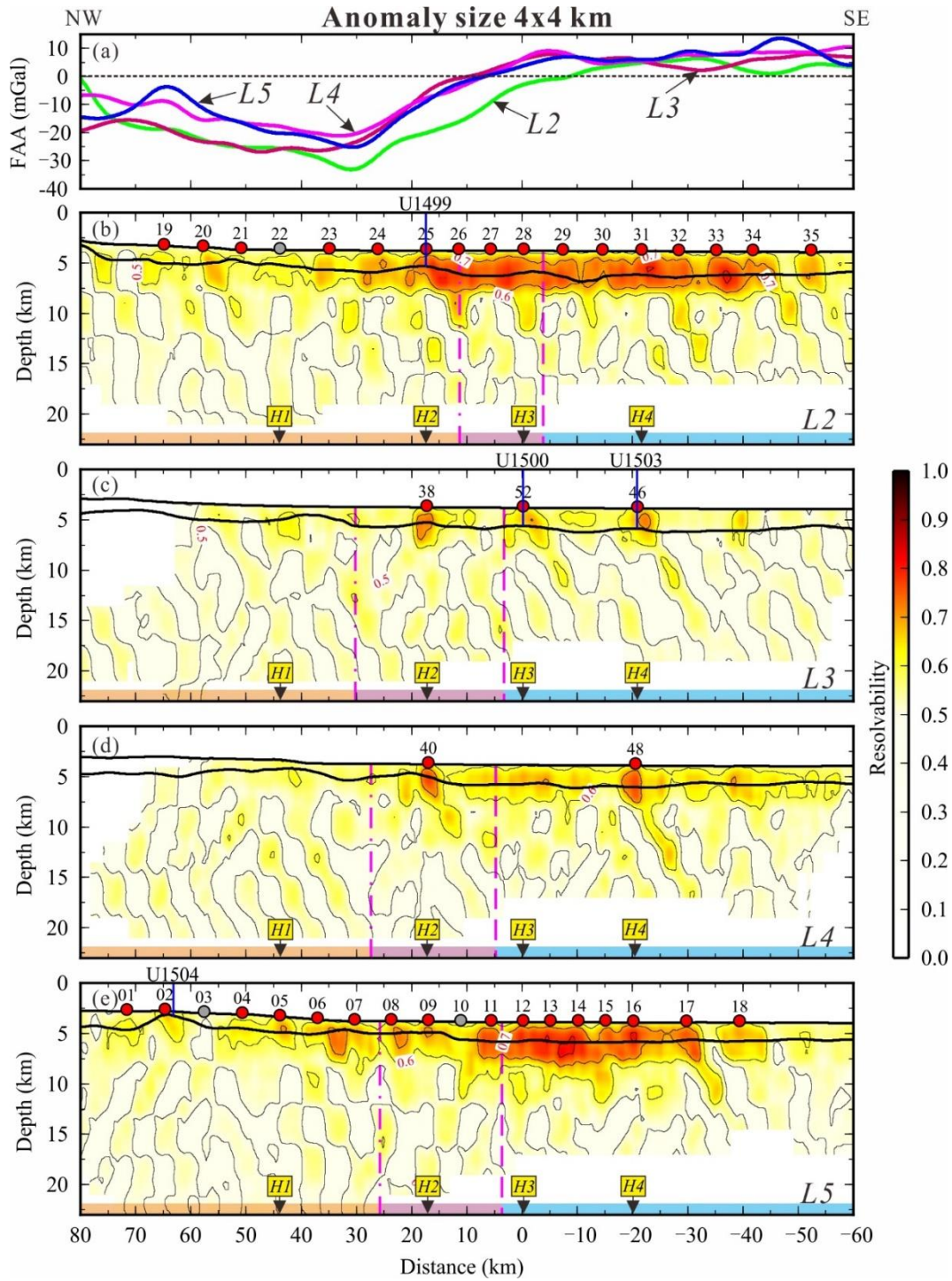
Figure S9. Vertical slices crosscutting the 3D resolvability models with retrieved checkerboard pattern of the 4x4 km (a-e), 10x10 km (a'-e') and 20x20 km (a''-e'') anomaly size. The other symbols are same as Figure 5.

Figure S9 (Continuous).
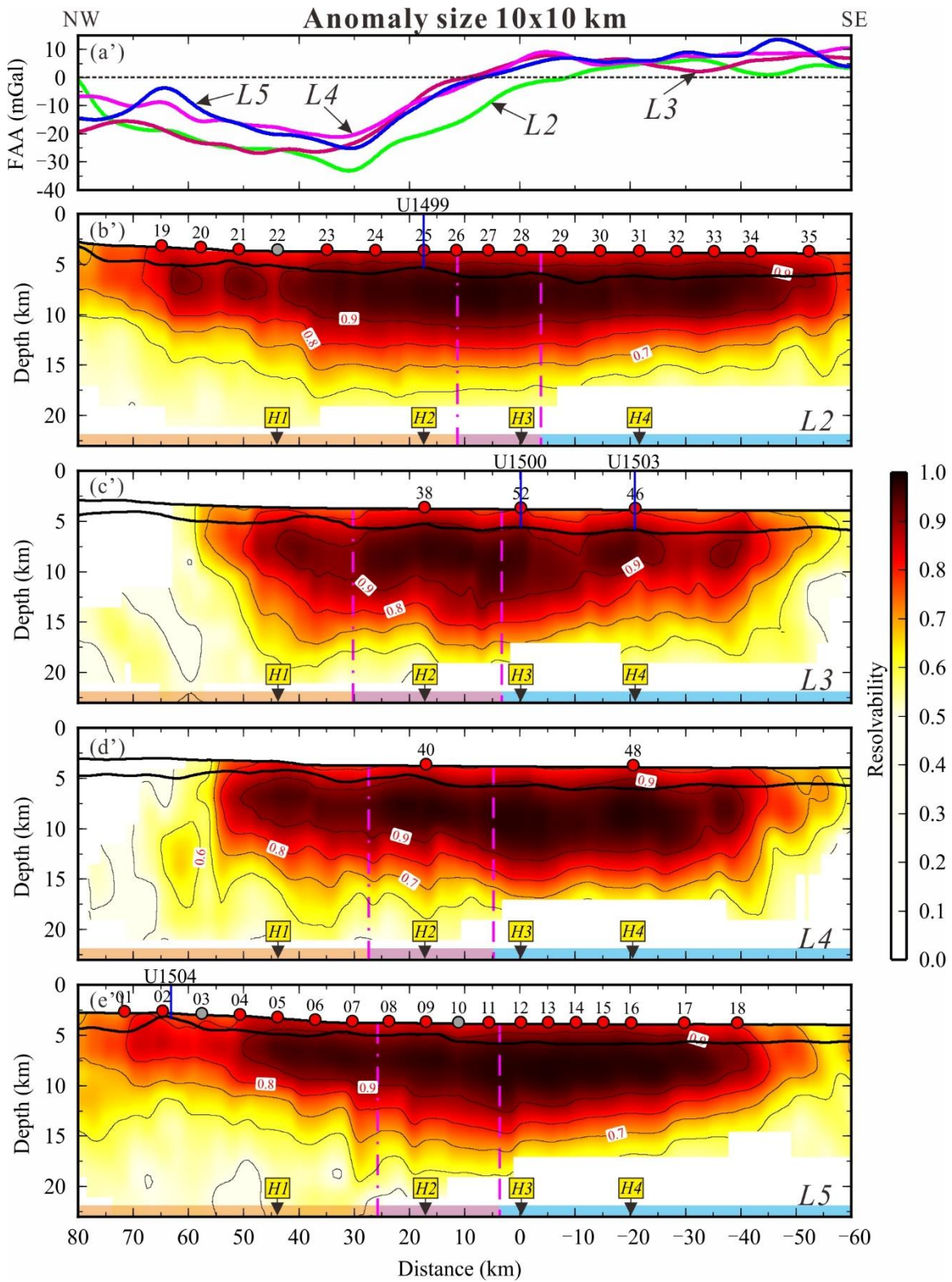
Figure S9 (Continuous).
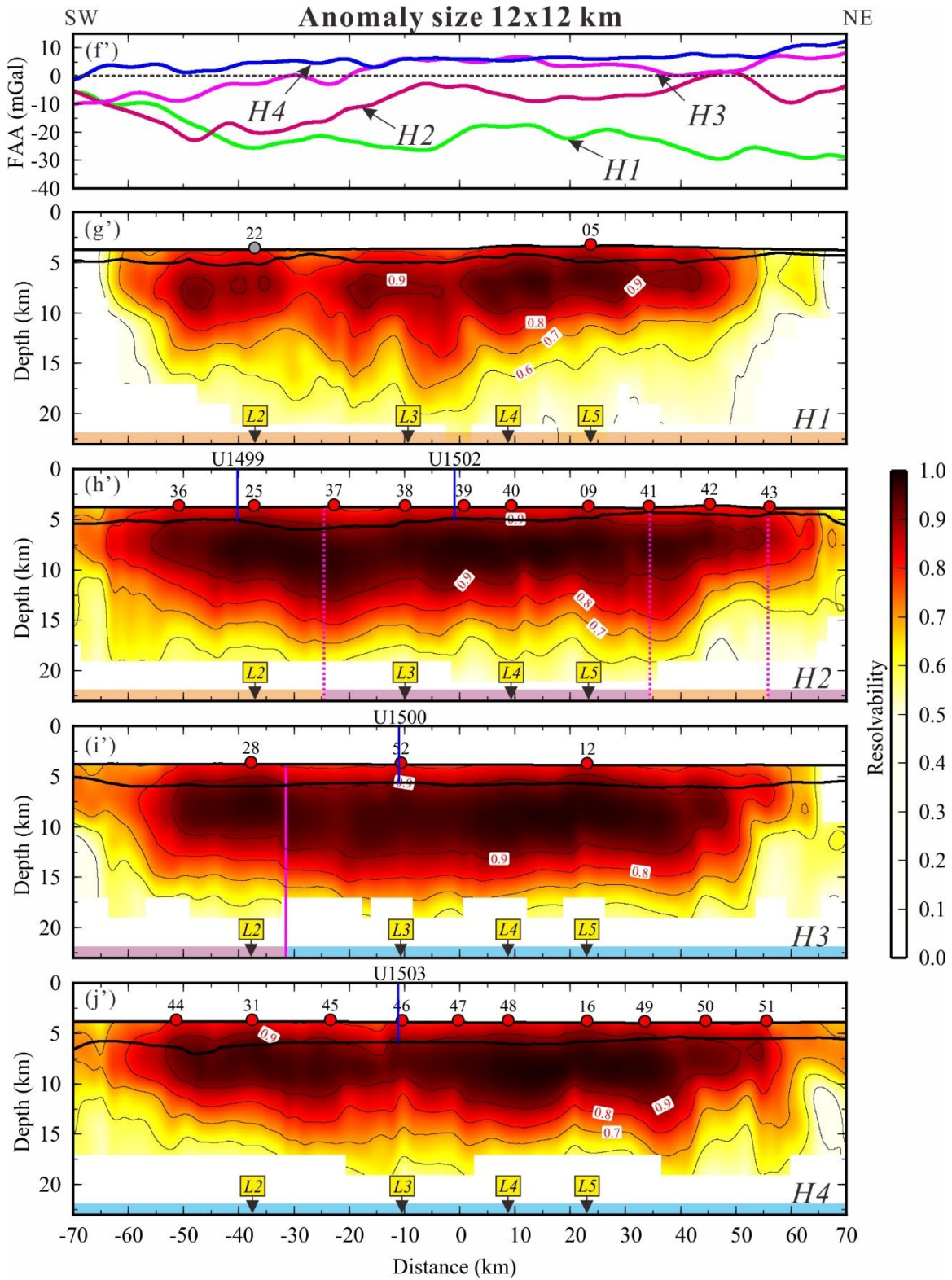
Figure S9 (Continuous).
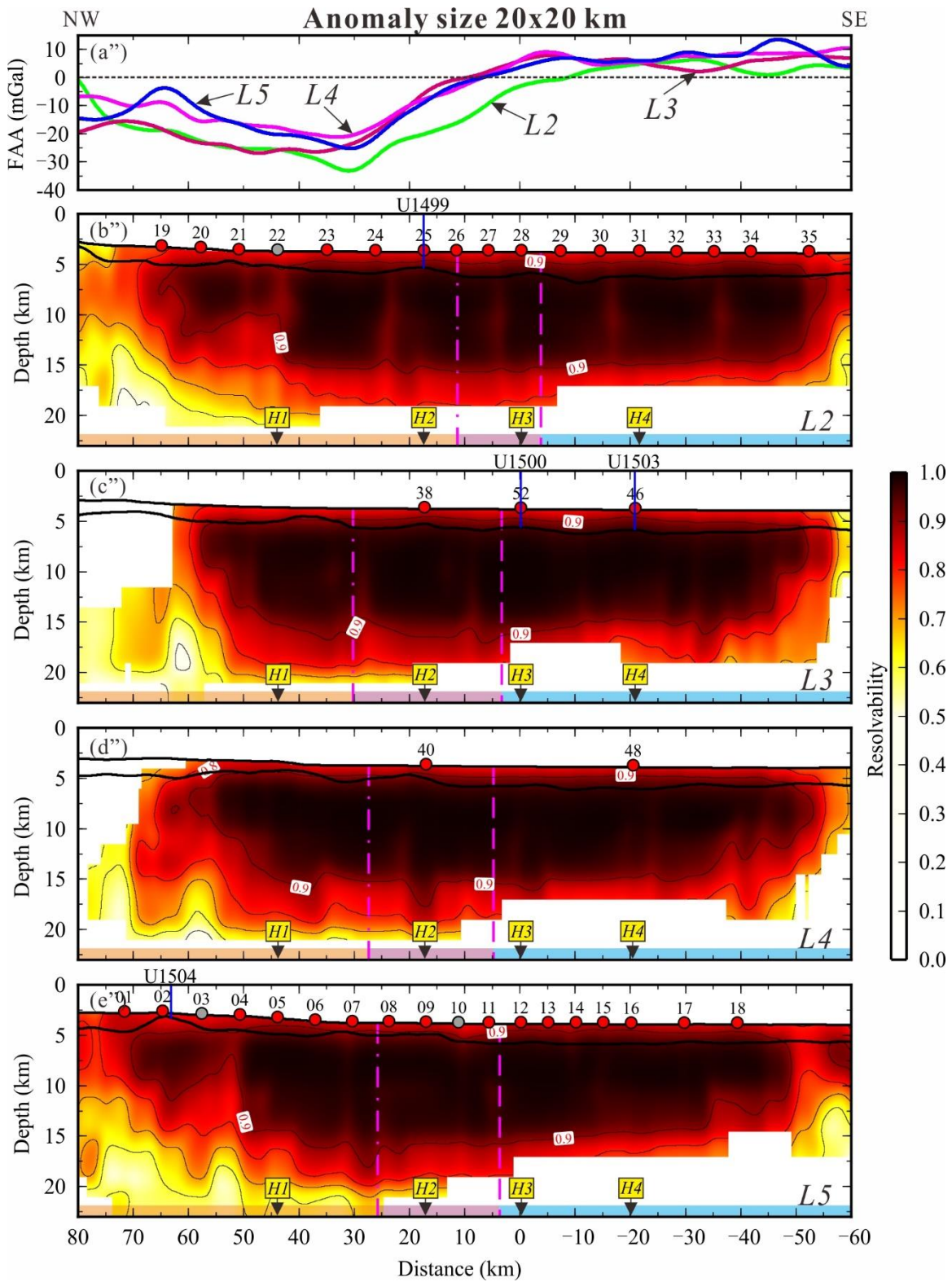
Figure S9 (Continuous).
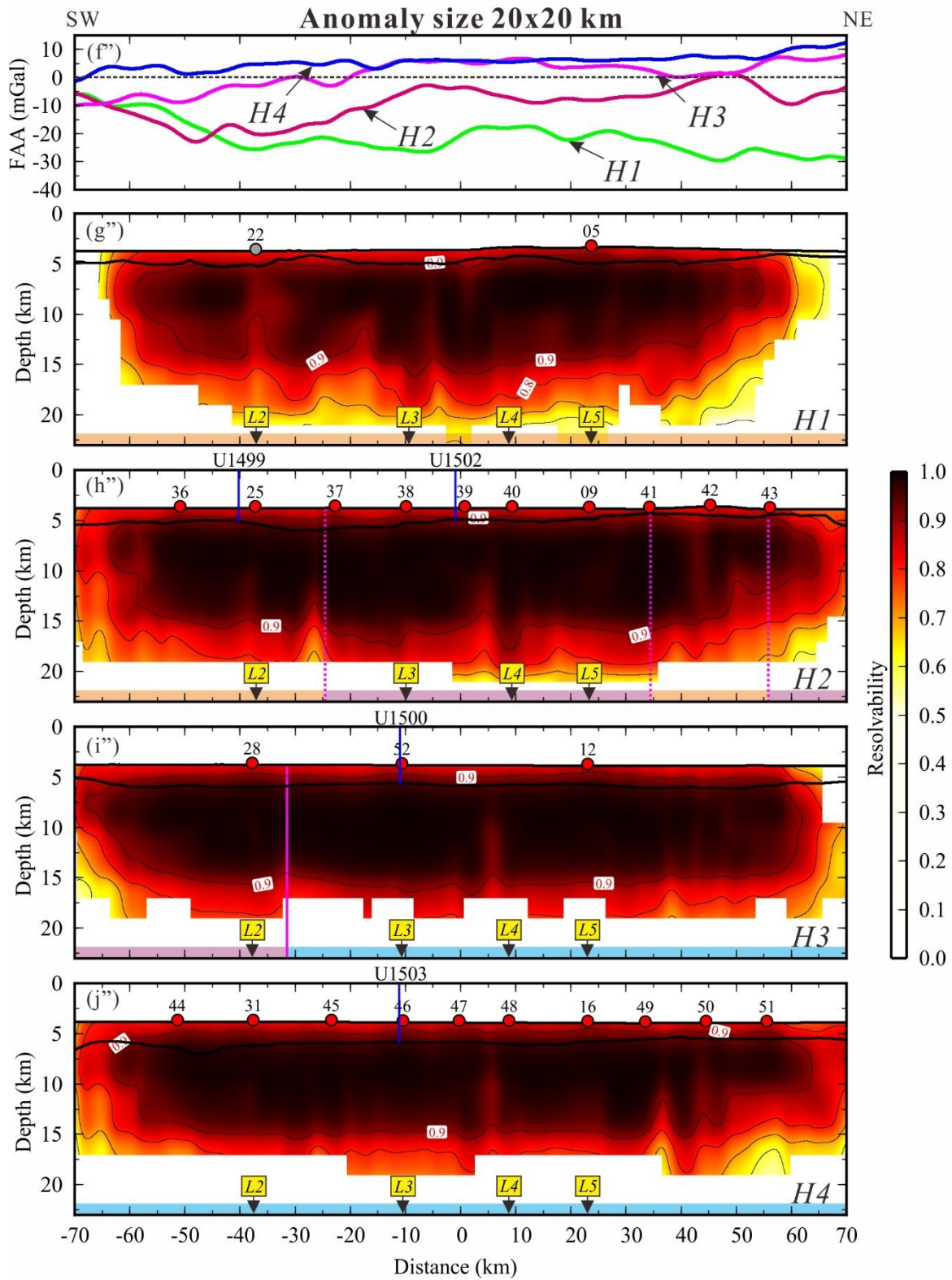
Figure S9 (Continuous).
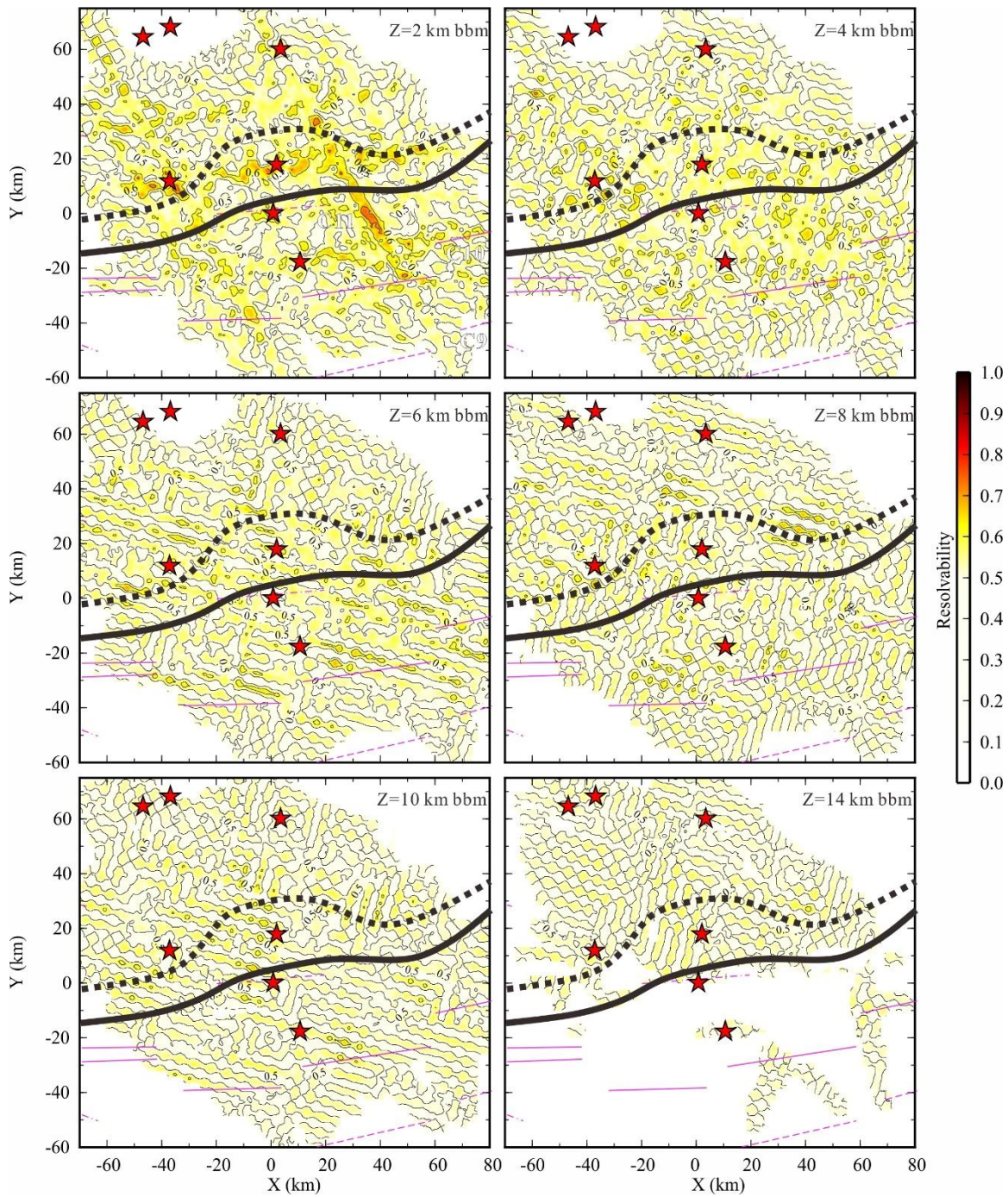
Figure S10. Horizontal slices of the 3D resolvability models with retrieved checkerboard pattern of the 4x4 km, 10x10 km and 20x20 km anomaly size at different depths below sea level (bsl). The other symbols are same as Figure 6.
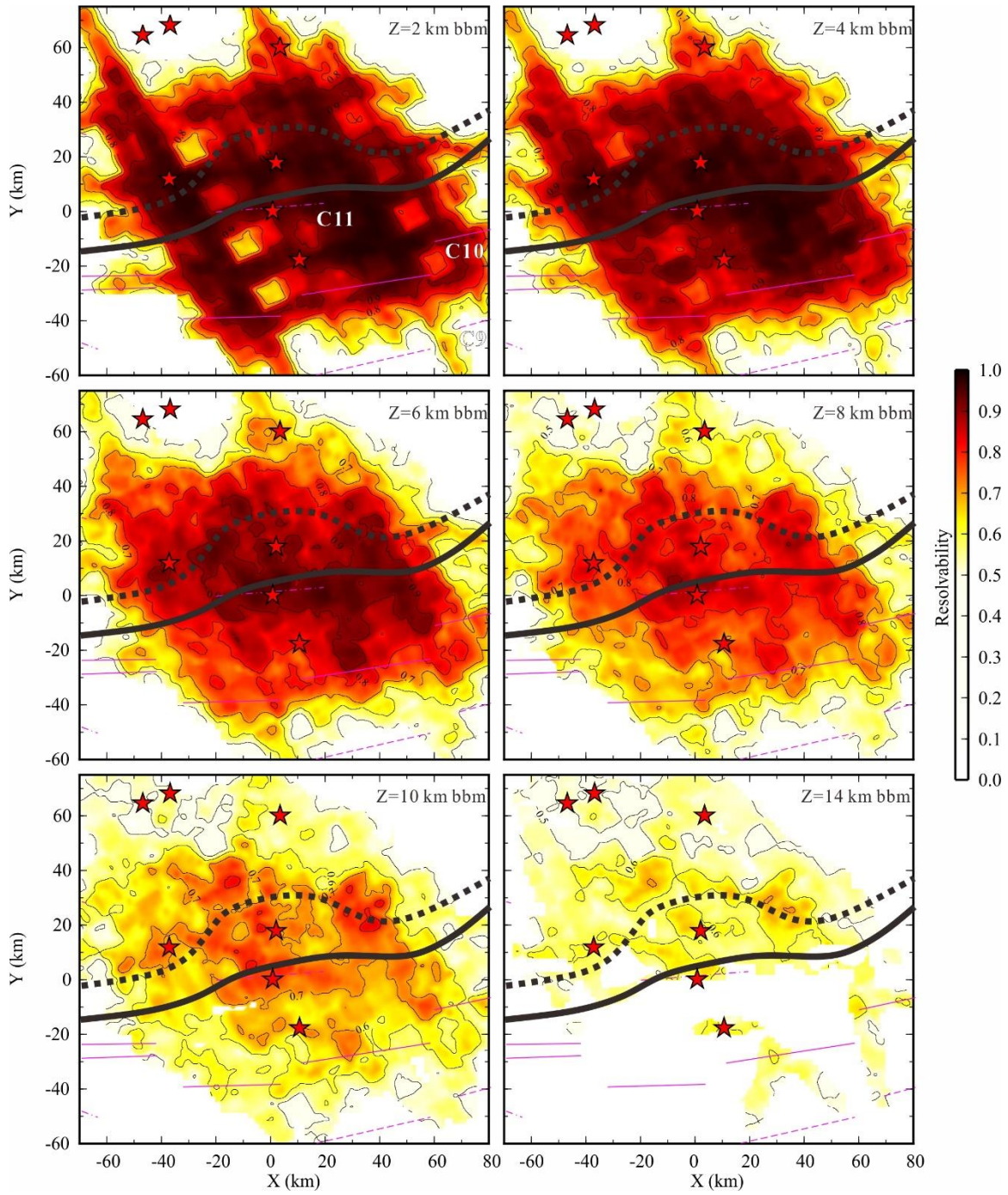
Figure S10 (Continuous).
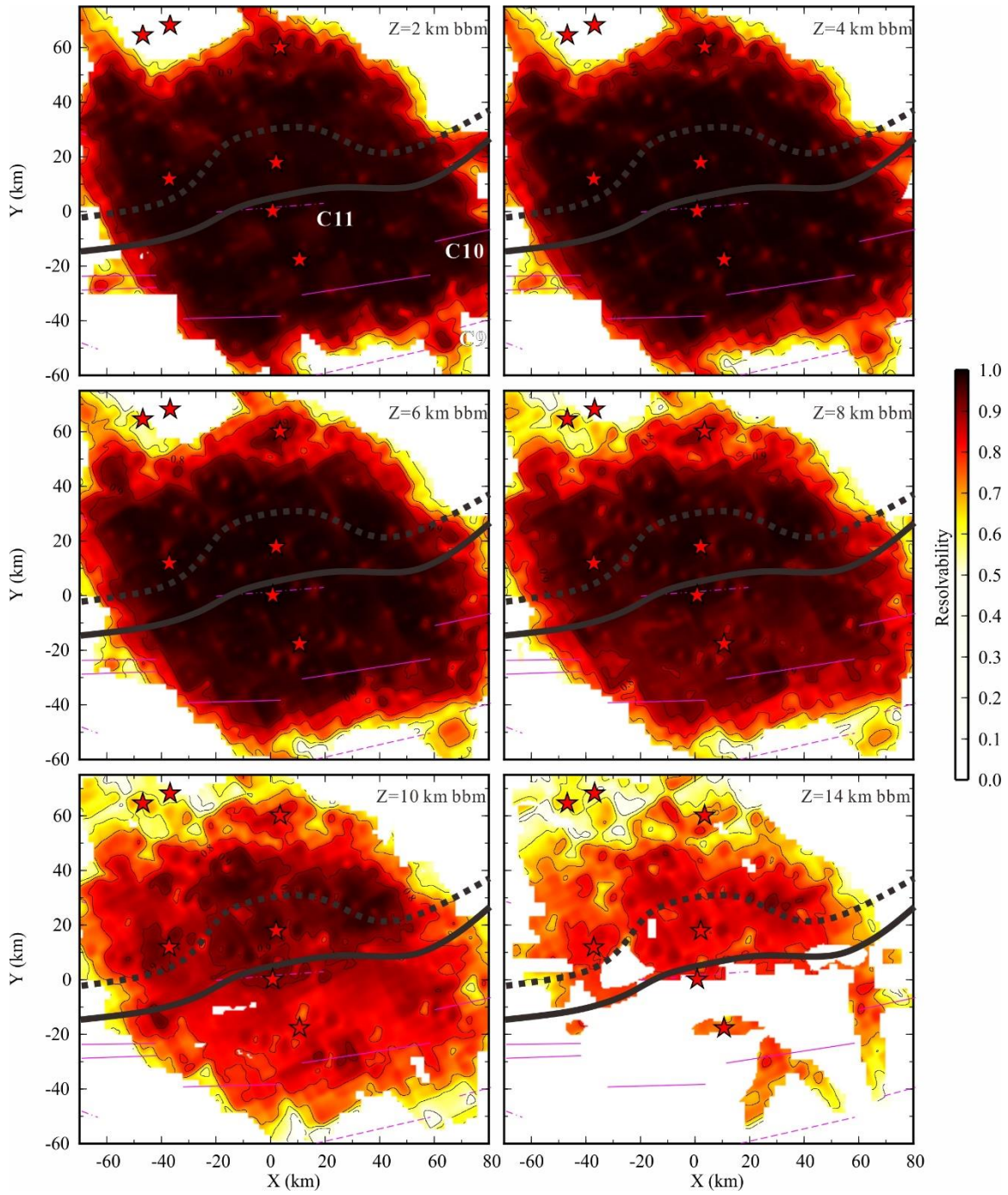
Figure S10 (Continuous).
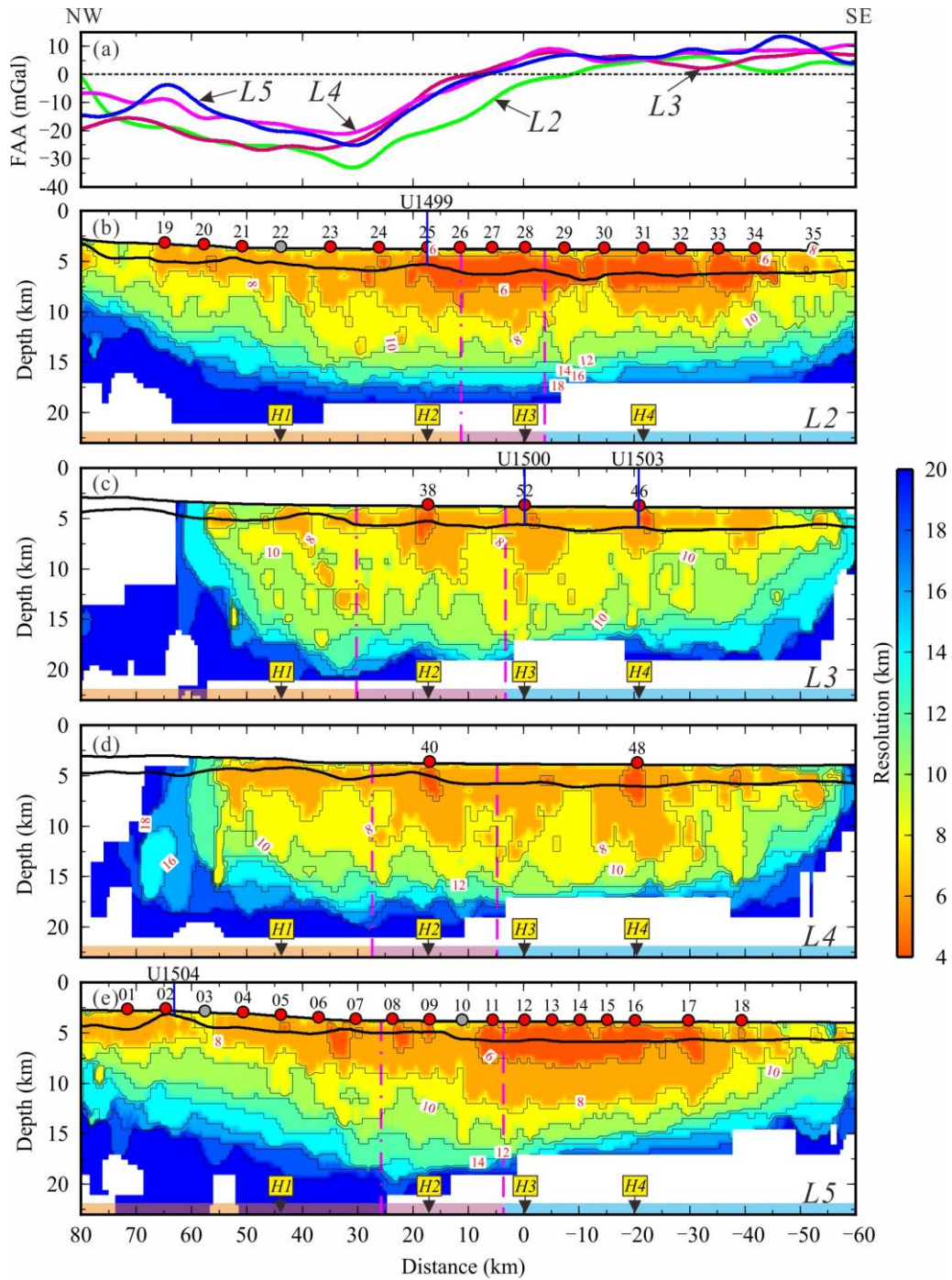
Figure S11. Vertical resolution maps showing the region at which we are able to retrieve each size of the checkerboard pattern. The other markers are same as Figure 5.
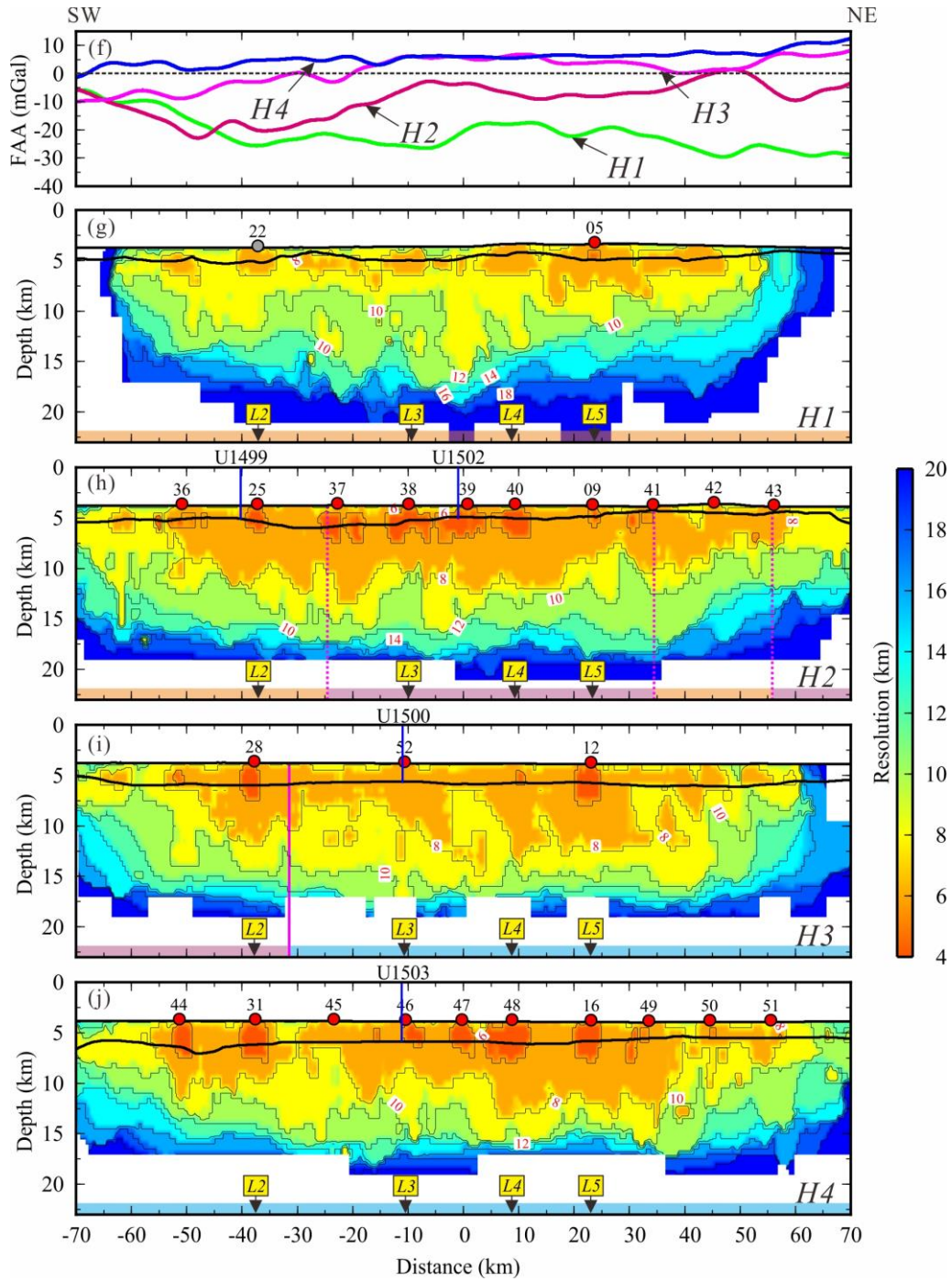
Figure S11 (Continuous).
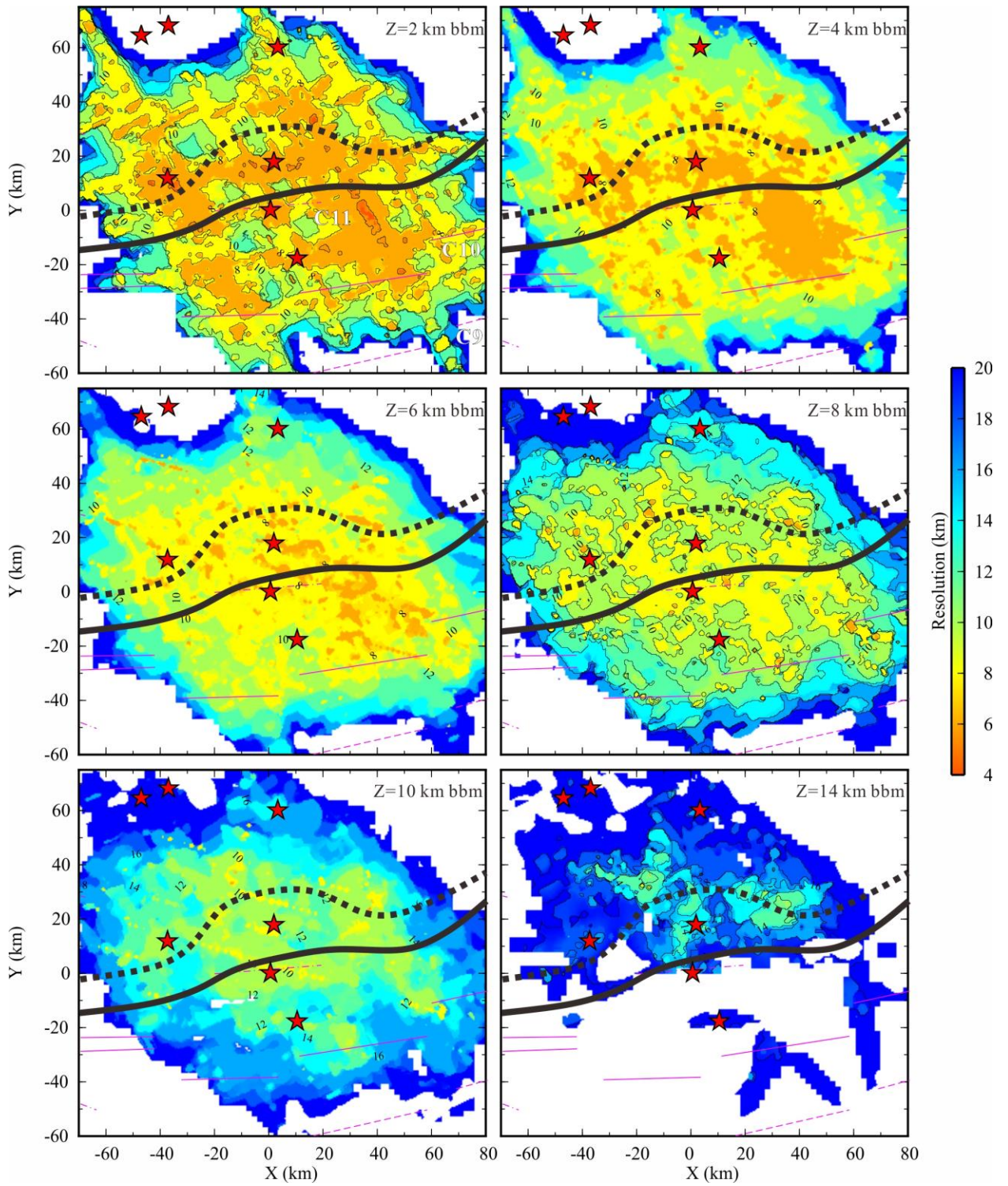
Figure S12. Horizontal resolution maps showing the region at which we are able to retrieve each size of the checkerboard pattern at different depths below TOB (bbm). The other markers are same as Figure 6.
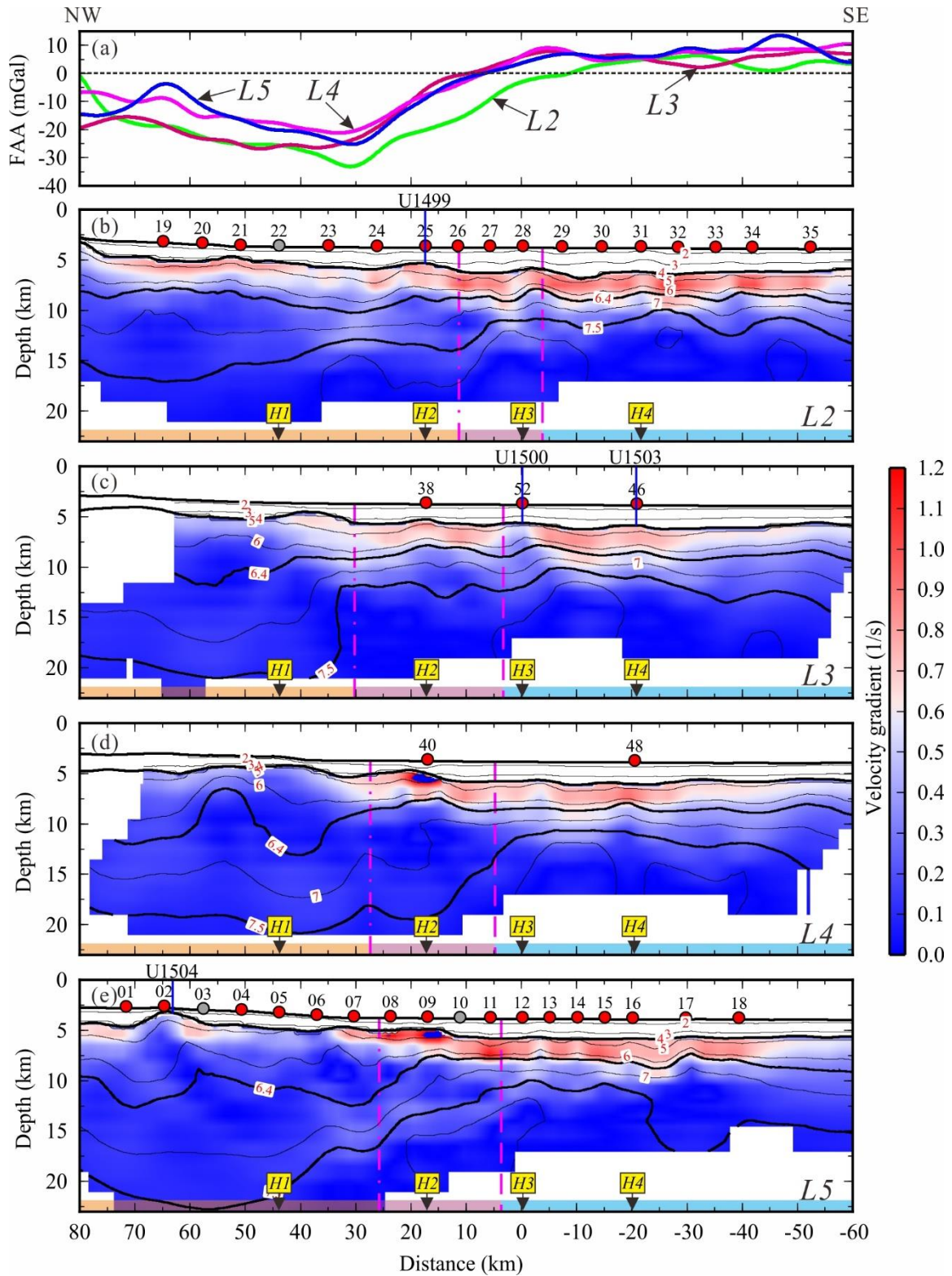
Figure S13. Vertical slices crosscutting the 3D velocity gradient model and free-air gravity anomaly. The other symbols are same as Figure 5.
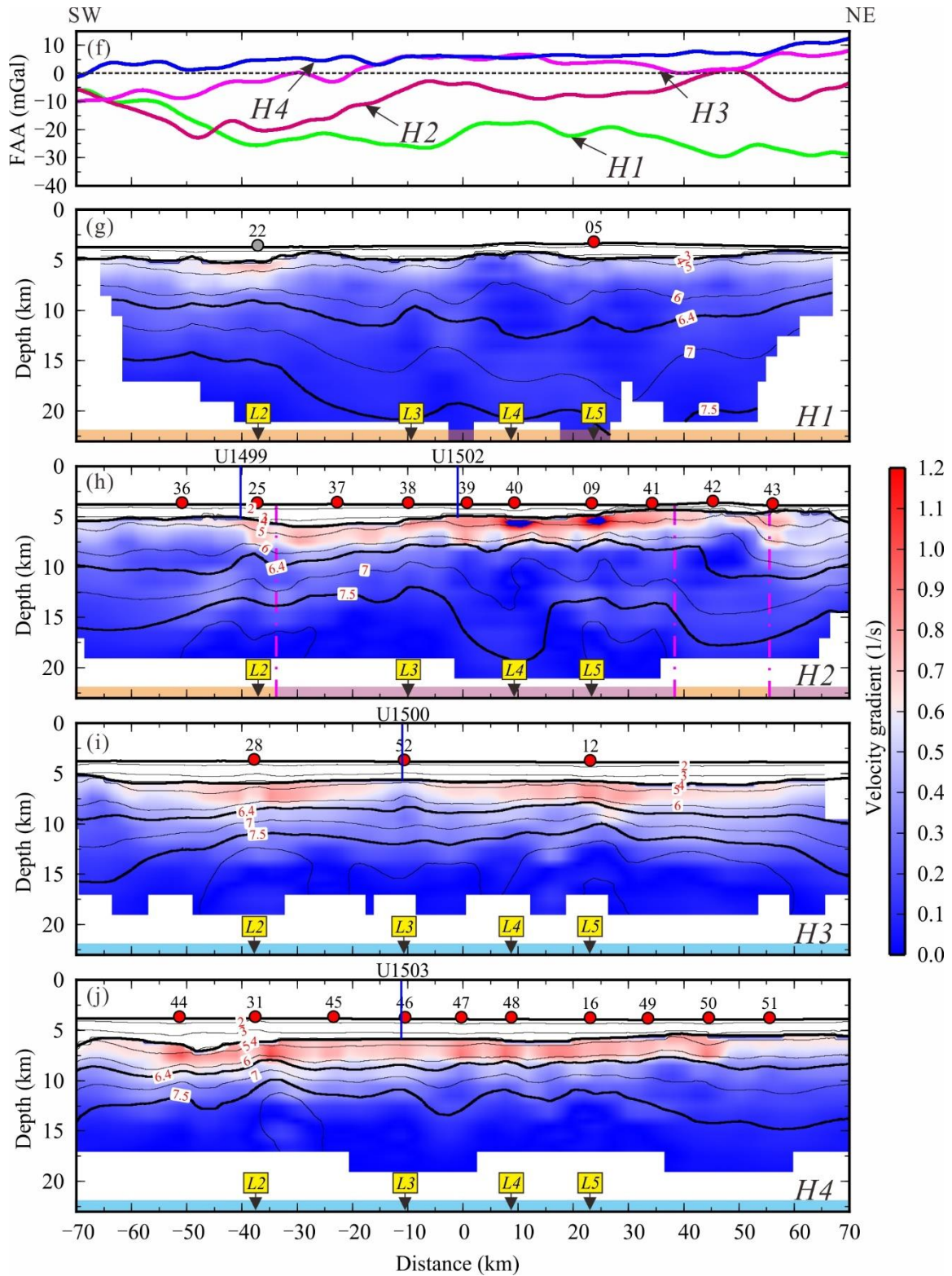
Figure S13 (Continuous).
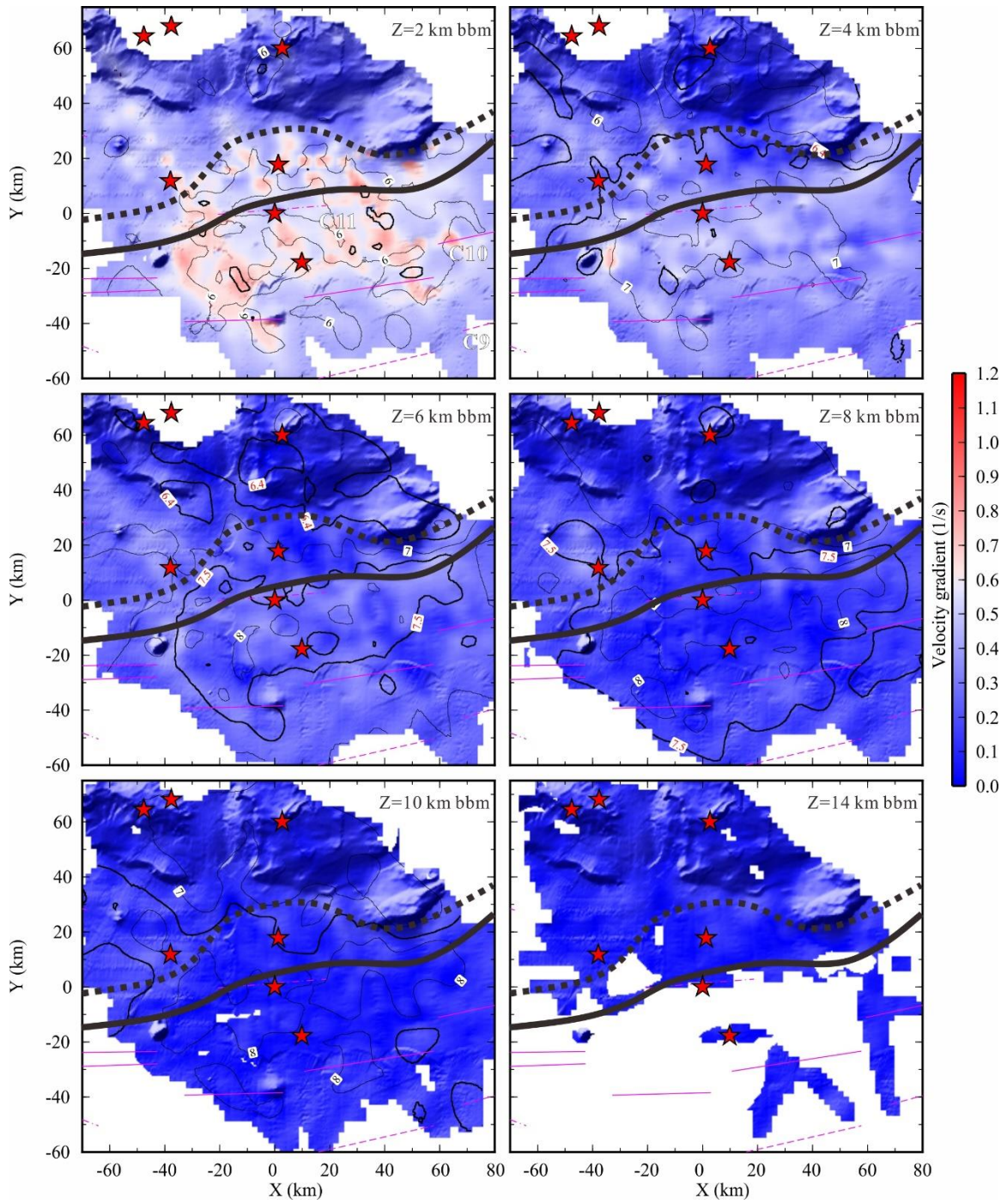
Figure S14. Horizontal slices of the 3D velocity gradient model at different depths below TOB (bbm). The other symbols are same as Figure 6.
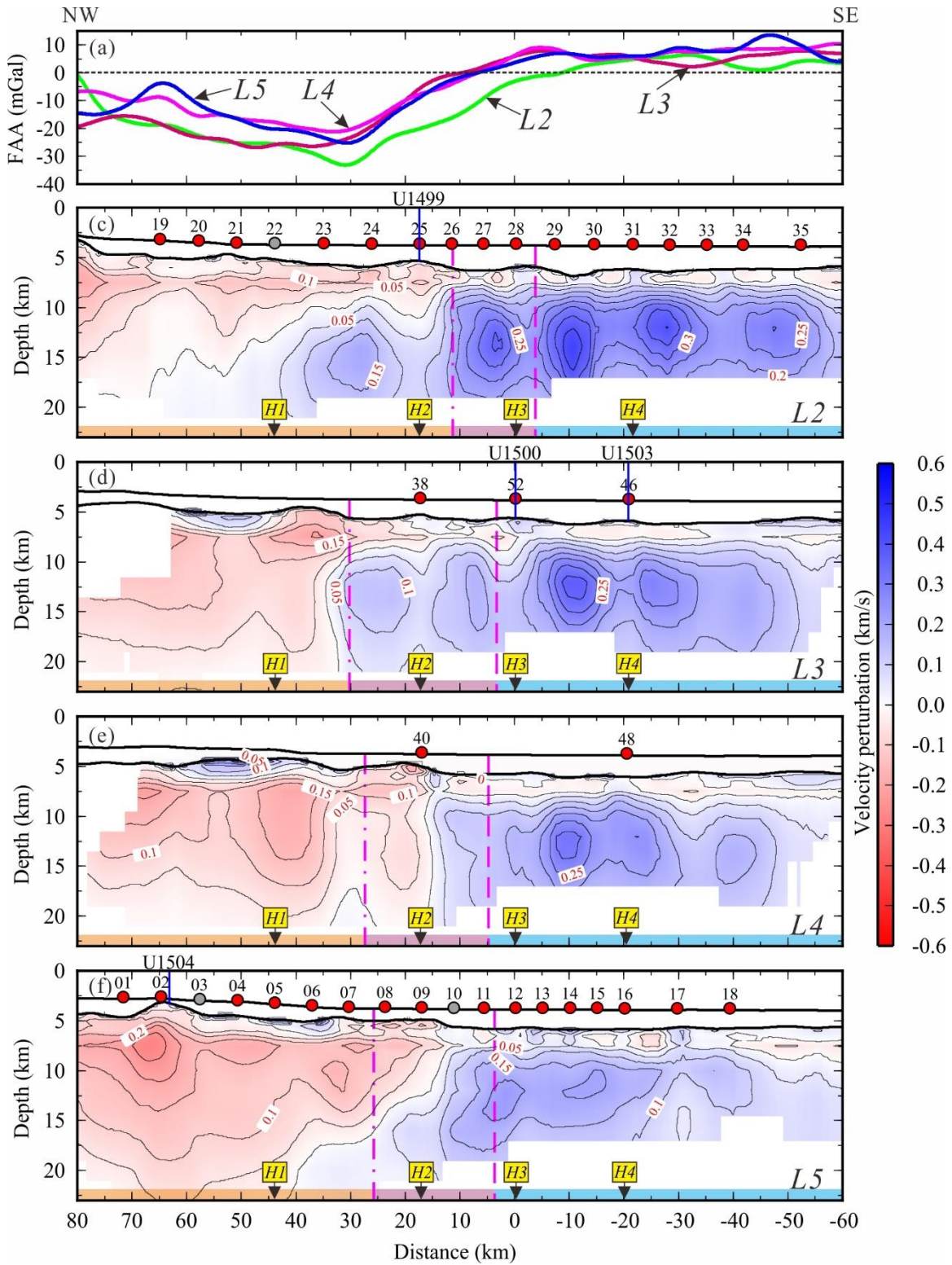
Figure S14. Vertical slices crosscutting the 3D velocity perturbation model and free-air gravity anomaly. The other symbols are same as Figure 5.
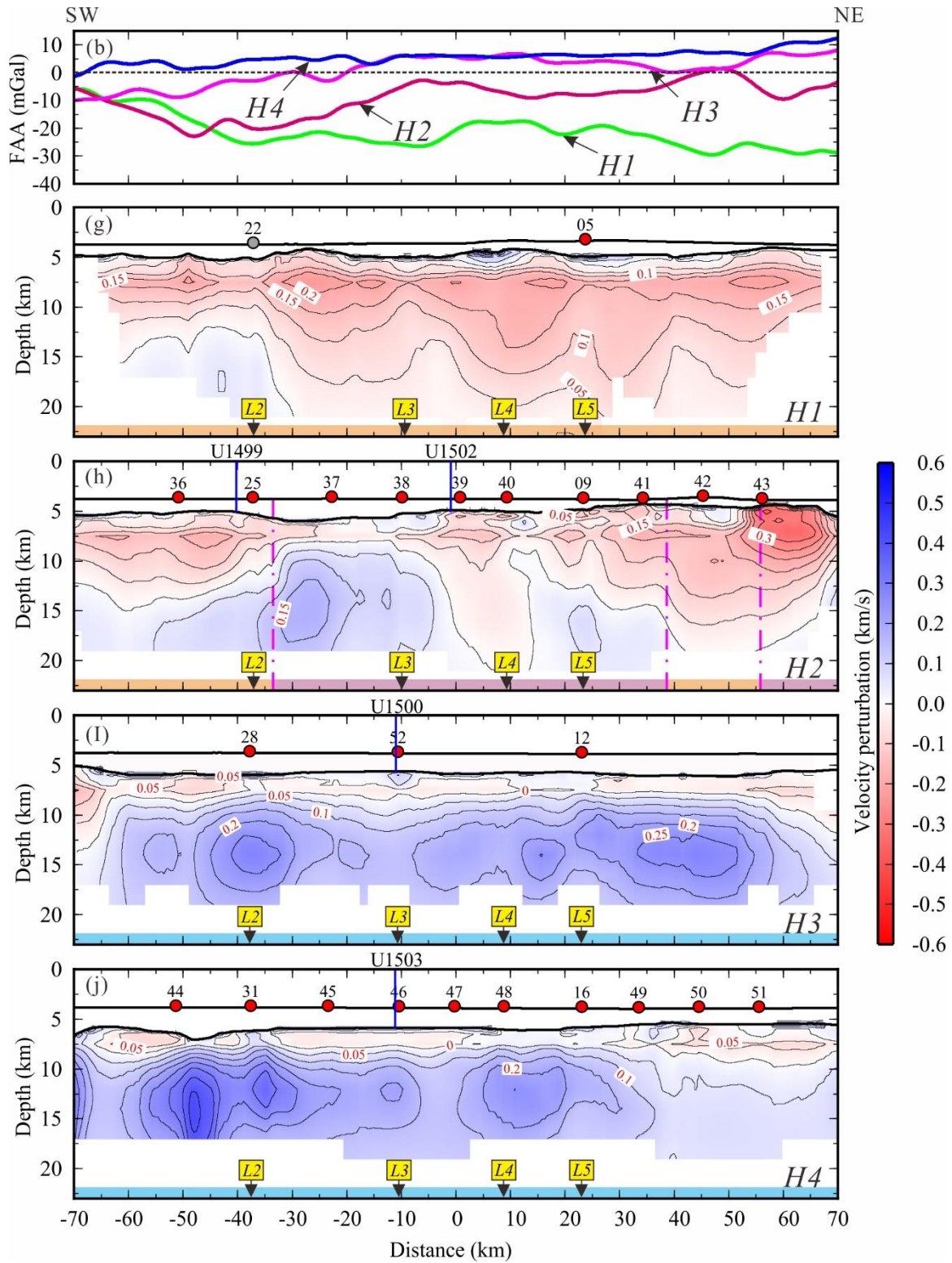
Figure S15 (Continuous).
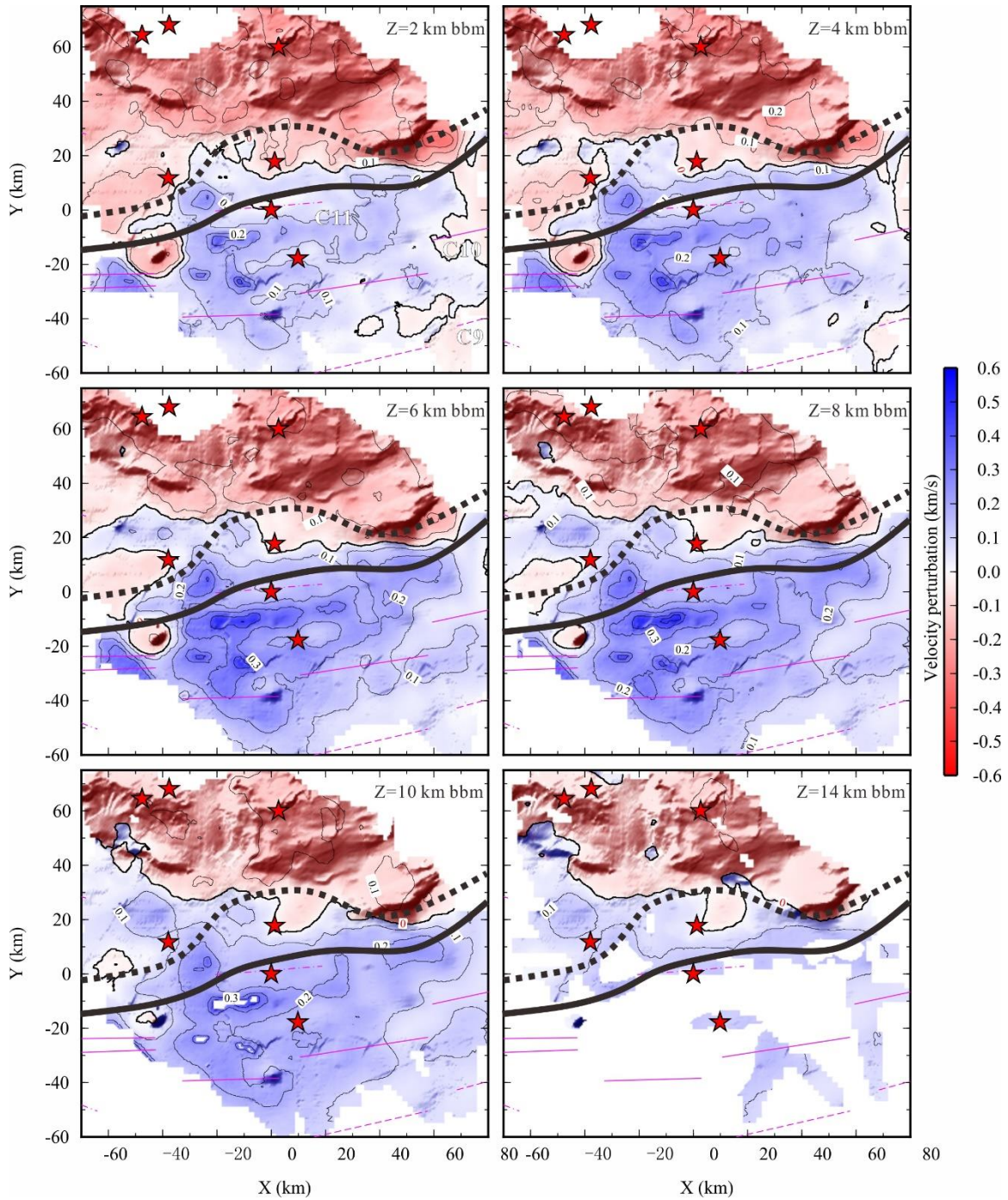
Figure S16. Horizontal slices of the 3D velocity perturbation model at different depths below TOB (bbm). The other symbols are same as Figure 6.
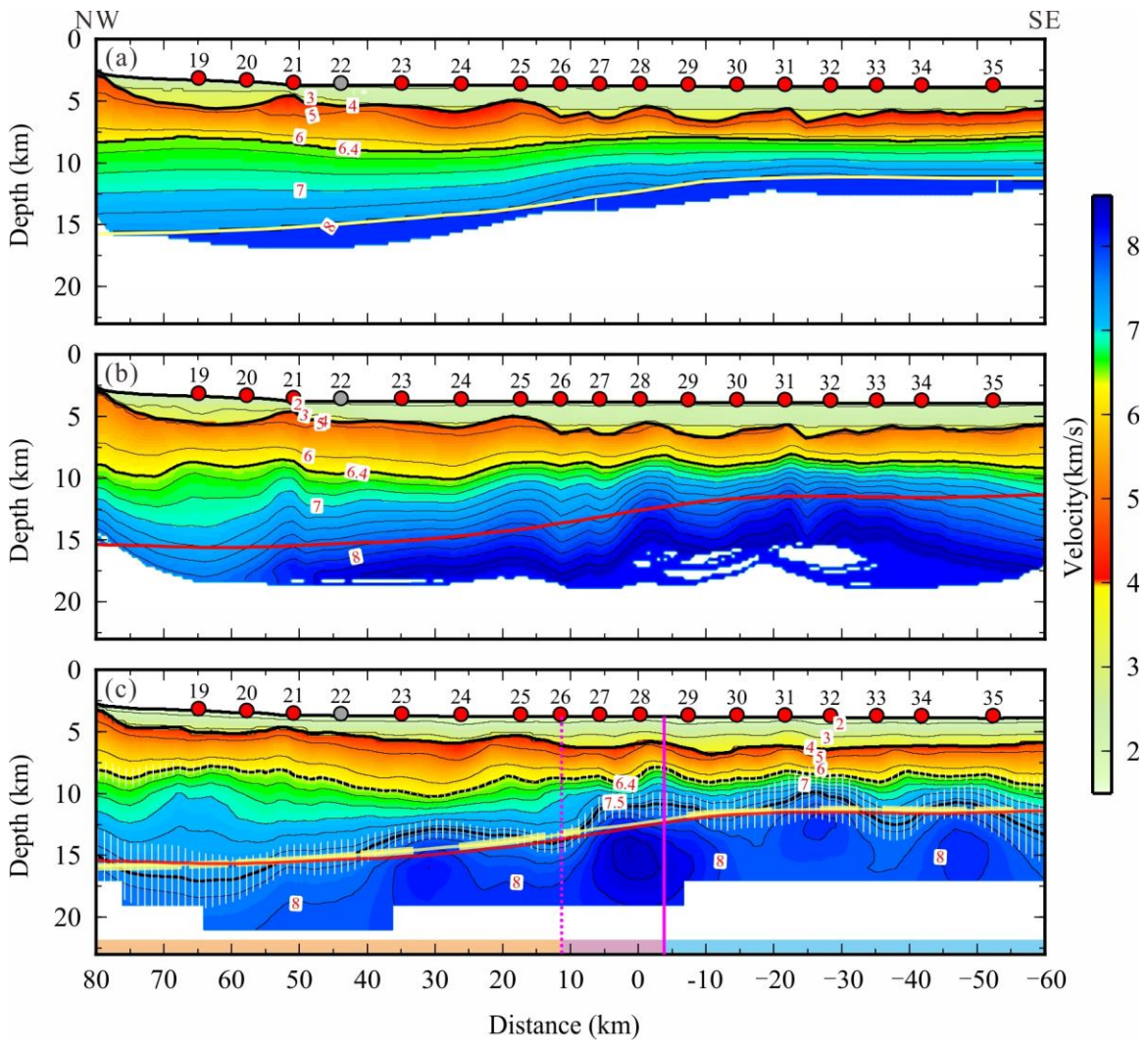
Figure S17. Comparison among (a) Forward Vp model by using RayInvr with the yellow line indicating the inverted Moho; (b) Inversion Vp model by using Tomo2D with the red line showing the inverted Moho; (c) Vertical slice from 3D Vp model along profile L2 with the yellow and red lines from (a) and (b) which correspond well with the 7.5 km/s velocity contour. The white bars show the depth uncertainties for 6.4 km/s and 7.5 km/s contours. The other symbols are same as Figure 5.
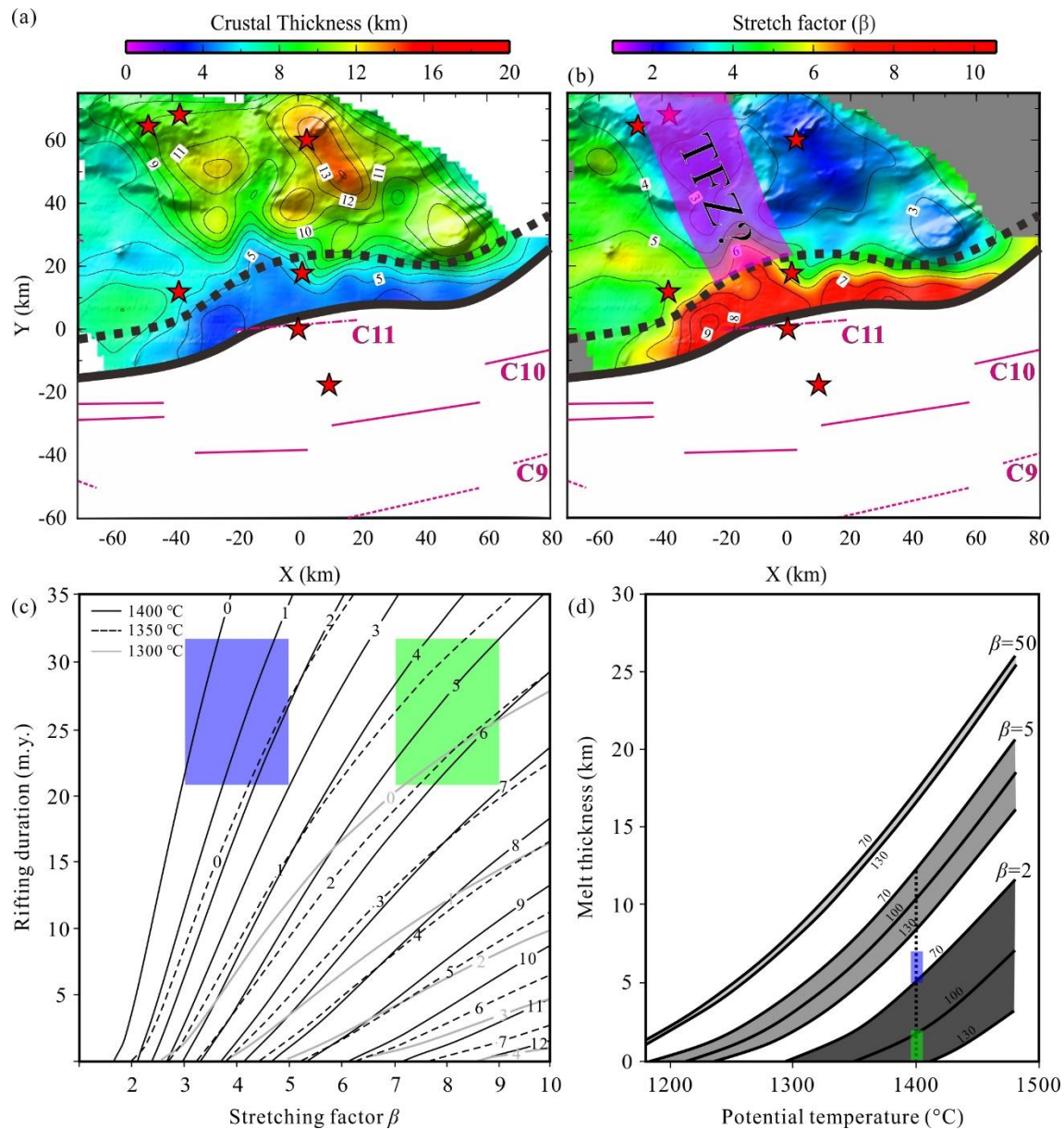
Figure S18. Analysis for the formation genesis of HVLC assuming that it is formed by syn-rift decompression melting of upwelling asthenosphere. (a) The whole crust thickness map removing the HVLC. (b) The whole crustal stretching factor (β) map assuming 32 km as the initial thickness (Li et al., 2006). (c) The relationship among melt thickness, β, rift duration and potential temperature of asthenosphere assuming 125 km as the initial continental lithospheric thickness (modified from Bown et al., 1995). The green and blue rectangles correspond to the SW and NE segments of continental domain, respectively, which are contrary to the observed HVLC thickness in Figure 7d. (d) The relationship among melt thickness, β, potential temperature of asthenosphere and initial continental lithospheric thickness assuming instantaneous breakup (modified from White & McKenzie, 1989). The green and blue thick lines correspond to the melt thickness inferred from HVLC in the SW and NE segments of continental domain, respectively. It can be seen that if the potential temperature of the asthenosphere is uniform of 1400 °C, the initial lithospheric thickness in NE segment should be smaller than 70 km assuming its β as 2, whereas the initial lithospheric thickness in SW segment should be larger than 260 km assuming its β as 5.